NUMERICAL STUDY OF THE OPTICAL PROPERTIES OF SILVER NANOSTRUCTURES WITH DIFFERENT TOPOLOGIC SHAPES

by

ZHONGYUE ZHANG

(Under the Direction of Yiping Zhao)

ABSTRACT

The collaborative oscillation of electrons in noble metal nanostructures results in a surface plasmon resonance that makes them useful for various applications including chemical and biological sensors, plasmonic waveguides, and enhanced spectroscopy. In this dissertation, we study the morphology dependent properties of the surface plasmon resonance, and the discrete dipole approximation method is used to investigate the optical properties of Ag nanostructures with different topologic shapes, such as the cylindrical nanorods, needle-shaped nanorods, period-shaped nanorods, L-shaped nanorods, Y-shaped nanorods, parallel-nanorod structures, U-shaped nanostructures, and the helical nanostructures.

For the cylindrical nanorods, the extinction spectra depend on both the aspect ratio (length/diameter) and the diameter. For short nanorods, the longitudinal mode plasmon peaks red shift linearly with aspect ratio. For larger aspect ratios, multipolar plasmon peaks appear in the extinction spectra which also red shift linearly with aspect ratio.

Comparing to nanorods with a simple shape (cylinder and needle), irregular nanorods shows many distinct plasmon resonances over a large spectra range. More hot spots are observed for the nanorods with more defects. These results show that defects or imperfections in Ag nanorod structures could drastically change the optical properties, generate extra hot spots for surface enhanced spectroscopy, and have different enhanced field distribution for future plasmonics applications. A U-shaped nanostructure has more hot spots than a parallel-nanorod structure; and at the longitudinal mode incidence, the electric field enhancements are much larger than those of the parallel-nanorod structure. These results could be used to engineer U-shaped nanostructures for specific plasmon applications.

Helical nanostructures are another good structure to tune the plasmon peak and arrange the electric field distribution. The plasmon peak and the electric field distribution can be tuned not only by the structural parameters but also by the polarizations of the incident light, especially the circular polarizations. In addition, the origins of the plasmon modes are also investigated. The transverse modes are due to the electron oscillations perpendicular to the cross sections and the longitudinal plasmon peaks are due to the charge oscillations along the arc length of the helix and are mainly determined by the effective dipole length.

INDEX WORDS: optical property, silver, nanorods, shape dependent, helix, discrete dipole approximation

NUMERICAL STUDY OF THE OPTICAL PROPERTIES OF SILVER NANOSTRUCTURES WITH DIFFERENT TOPOLOGIC SHAPES

by

ZHONGYUE ZHANG

B.S., Lanzhou University, China, 1998

M.S., University of Science and Technology of China, China, 2004

A Dissertation Submitted to the Graduate Faculty of the University of Georgia in Partial Fulfillment of the Requirements for the Degree

DOCTOR OF PHILOSOPHY

ATHENS, GEORGIA

2009

NUMERICAL STUDY OF THE OPTICAL PROPERTIES OF SILVER NANOSTRUCTURES WITH DIFFERENT TOPOLOGIC SHAPES

by

ZHONGYUE ZHANG

Major Professor:	Yiping Zhao
Committee:	William M. Dennis Qun Zhao Zhengwei Pan

Electronic Version Approved:

Maureen Grasso
Dean of the Graduate School
The University of Georgia
May 2009

ACKNOWLEDGEMENTS

I wish to express my sincere appreciation to my advisor, Prof. Yiping Zhao, for his support, guidance, and encouragement during the course of this research. His insight and passion have inspired and taught me beyond research. I also thank Prof. William M. Dennis, Prof. Qun Zhao, and Prof. Zhengwei Pan, for serving on my thesis reading committee and providing helpful suggestions and support on this research.

I would like to thank all my former and current lab colleagues. I thank Dr. Yuping He, Mr. Yongjun Liu, and Mr. Wilson Smith for the assistance and the collaboration. Support and friendship of Dr. Jianguo Fan, Mr. John Gibbs, Mr. Justin Abell, Dr. Vivien Chu are much appreciated. I enjoyed the work with Ms. Junxue Fu, Dr. Hang Liu, Dr. Yang Zhang, and Dr. Qiang Liu. I also thank Mr. Peter Dluhy for proof reading my manuscripts.

I gratefully acknowledge help and support from the following people: Mr. Zhuofei Hou, Dr. Yi Zhou, and Mr. Jason Langley in the department of physics and astronomy, Ms. Shan-Ho Tsai in university of Georgia research computer center.

I wish to extend to my deepest thanks to my family, especially my mother and my wife, for constant dedication, love, and support. Finally, I thank my daughter who brings so much happiness to my family

TABLE OF CONTENTS

Page

LIST OF TABLES

Page

LIST OF FIGURES

CHAPTER 1

INTRODUCTION

1.1 Surface plasmon resonance

The colors of colloidal noble metal particles in stained glass windows have inspired not only artists but also many scientists. These colors have been used to decorate windows of many cathedrals, palaces, etc. In 1857, Michael Faraday showed these colors are due to the metal nanoparticles with a size much smaller than the incident wavelength[3]. In 1908, Gustav Mie explained these colors using classical electromagnetic theory [4]. The origin of these colors is due to the strong absorption and scattering of light by the dispersion of metal nanoparticles [5-7]. In a classical description, the electric field of an incoming light wave induces a polarization of the electrons with respect to the much heavier ionic core of a spherical nanoparticle. A net charge difference is only felt at the nanoparticle surface, which in turn acts as a restoring force. This creates, in the simplest case, a dipolar oscillation of all the electrons with the same phase. When the frequency of the electromagnetic field becomes resonant with the coherent electron motion, a strong absorption occurs in the spectrum. This is the origin of the observed color. The resonance between the frequency of electrons oscillation and the frequency of the incident light is known as plasmon resonance. Since the net charge difference appears at the surface of a nanoparticle, this resonance is also known as the localized surface plasmon resonance (LSPR)[5].

Ag and Au are well known for their ability to generate LSPR. With resonant excitations, the strong interactions of the collective oscillations of the conduction electrons within the particles can excite a strong local electromagnetic field compared to the incident field, which is one of the major mechanisms of surface enhanced Raman scattering (SERS)[8-10]. The plasmon resonances of a nanoparticle depend strongly on its composition[11-14], morphology[15-27], surrounding media[28-30], as well as the assembly of the nanostructures[31-34]. For single metallic particles, the plasmon resonance frequency is determined by the particle size and particle shape. When spherical metal particles are transformed to rods[15, 16], disks[17, 18, 22], triangular prisms[19, 21], and nanorings[20], the plasmon resonances and the *E* field enhancement distributions are strongly affected. Composite particles, such as multilayer disks[11], core-shell spheres[12], and barcodes[13], also show unique LSPR properties.

Because of the enhancement of the electric field around and between the metallic nanoparticles, sub-wavelength holes, corrugations, and textures in metallic films, the plasmon resonance is being exploited for the construction of nanoscale optical and photonic devices [35-45], such as superlenses, optical data storage, plasmon waveguide, nano-optics, and apertureless near field scanning optical microscopy. Other important applications are sensors and biosensors based on the sensitivity of the surface plasmon band to detect attached molecules and environmental changes [46-48] or the surface electric field enhancement which amplifies the signal of several optical techniques: surface enhanced Raman scattering (SERS) [9, 10], surface enhanced resonance Raman scattering (SERRS) [9, 10], surface enhanced infrared absorption spectroscopy (SEIRAS) [49], and enhanced fluorescence spectroscopy [50-53]. Recently, based on the surface plasmon resonance, negative refractive index (NRI) materials have attracted a lot of researchers[54-59], which show several interesting effects such as bending light oppositely, negative radiation pressure, and Dopper shift reversal [60, 61].

1.2 Mie theory

In 1908, Mie theoretically explained the extinction and scattering of small spherical metal particles by solving Maxwell's equation for an electromagnetic wave interacting with a small sphere having the same macroscopic, frequency-dependent material dielectric constant as the bulk metal[4]. According to Mie theory, the scattering efficiency Q_{sca} and the extinction efficiency Q_{ext} can be written as,

$$Q_{sca} = \frac{2}{x^2}\sum_{n=1}^{\infty}(2n+1)(|a_n|^2 + |b_n|^2)\,, \tag{1.1}$$

$$Q_{ext} = \frac{2}{x^2}\sum_{n=1}^{\infty}(2n+1)\,\mathrm{Re}(a_n + b_n)\,, \tag{1.2}$$

where $x = kr$ is the size parameter, r is the radius of the sphere, $k = 2\pi/\lambda$ is the wave number, λ is the wavelength in the ambient medium, and

$$a_n = \frac{m^2 j_n(mx)[xj_n(x)]' - \mu_1 j_n(x)[mxj_n(mx)]'}{m^2 j_n(mx)[xh_n^{(1)}(x)]' - \mu_1 h_n^{(1)}(x)[mxj_n(mx)]'}\,, \tag{1.3}$$

$$b_n = \frac{\mu_1 j_n(mx)[xj_n(x)]' - j_n(x)[mxj_n(mx)]'}{\mu_1 j_n(mx)[xh_n^{(1)}(x)]' - h_n^{(1)}(x)[mxj_n(mx)]'}\,, \tag{1.4}$$

where m is the refractive index of the sphere relative to the ambient medium, μ_1 is the ratio of the magnetic permeability of the sphere to the magnetic permeability of the ambient medium, the functions $j_n(z)$ and $h_n^{(1)}(z) = j_n(z) + iy_n(z)$ are spherical Bessel functions of order n (n = 1, 2, …), and the primes mean derivatives with respect to z. The derivatives follow the properties of the spherical Bessel functions,

$$[zj_n(z)]' = zj_{n-1}(z) - nj_n(z), \tag{1.5}$$

$$[zh_n^{(1)}(z)]' = zh_{n-1}^{(1)}(z) - nh_n^{(1)}(z). \tag{1.6}$$

For $n = 0$ and 1, the spherical Bessel functions are given by:

$$j_0(z) = \sin(z)/z, \tag{1.7}$$

$$j_1(z) = \sin(z)/z^2 - \cos(z)/z, \tag{1.8}$$

$$y_0(z) = -\cos(z)/z, \tag{1.9}$$

$$y_1(z) = -\cos(z)/z^2 - \sin(z)/z. \tag{1.10}$$

The recurrence formula is given by:

$$f_{n-1}(z) + f_{n+1}(z) = \frac{2n+1}{z} f_n(z). \tag{1.11}$$

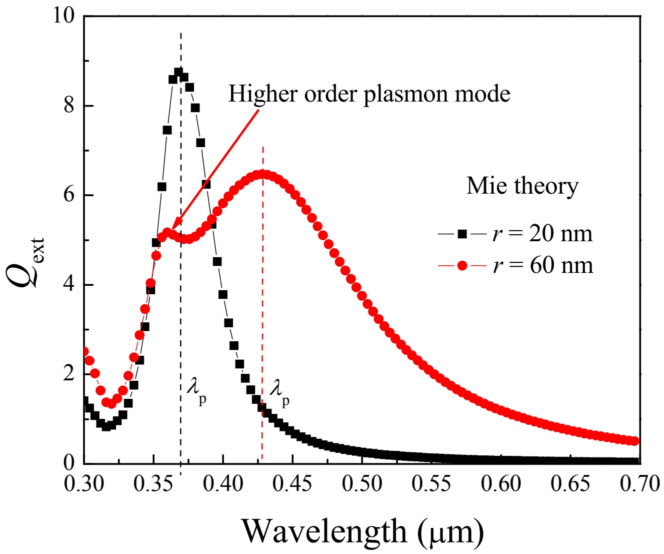

Figure 1.1 The extinction spectrum of Ag spheres calculated by Mie theory.

Figure 1.1 shows the extinction efficiency Q_{ext} of Ag spheres with radius r = 20 and 60 nm calculated from Eq. 1.2. The bulk refractive indicies are taken from Ref.[1]. When the radius increases from r = 20 nm to r = 60 nm, the dipolar mode plasmon peak red shifts from λ = 0.368 μm to λ = 0.429 μm. At the same time, because the incident light can not polarize the larger sphere homogeneously, higher-order mode (Quadrupole mode here) appears at the left side of the dipolar plasmon peak.

1.3 Gans theory

Mie's theory was developed for particles of spherical shape only. Gans extended Mie's theory within the dipole approximation. For randomly oriented elongated spheroids, Gans theory predicts that the extinction cross section C_{ext} ($C_{ext} = Q_{ext}\ \pi a_{eff}^2$, where a_{eff} is the effective radius of the nanoparticles) can take the following form[62],[63],

$$C_{ext} = \frac{2\pi N V \varepsilon_m^{3/2}}{3\lambda} \sum_j \frac{(1/P_j^2)\varepsilon_2}{(\varepsilon_1 + \frac{1-P_j}{P_j}\varepsilon_m)^2 + \varepsilon_2^2} \qquad (1.12)$$

where N is the concentration of the spheroids in small density solutions, V is the volume of a single spheroid, ε_1 and ε_2 are the real and imaginary part of the dielectric function of the material, ε_m is the dielectric constant of the surrounding medium, and the P_j (j = A, B, and C) is the depolarization factor for the three axes: A (long axis), B (short axis), and C (short axis) of a spheroid,

$$P_A = \frac{1-e^2}{e^2}\left[\frac{1}{2e}\ln\left(\frac{1+e}{1-e}\right) - 1\right] \qquad (1.13)$$

$$P_B = P_c = \frac{1-P_A}{2} \qquad (1.14)$$

$$e = (1-\xi^{-2})^{1/2} \qquad (1.15)$$

where the aspect ratio ξ is defined as $\xi = L/D$. The diameter of the long axis of the spheroid is L, and short axis is D. It is found that extinction cross section C_{ext} of the spheroid is only a function of the aspect ratio ξ.

Figure 1.2 shows some representative extinction cross section spectra of the Ag spheroids with different aspect ratios ξ, in which we take $NV = 1$. The dielectric constants used in the calculation are the bulk Ag dielectric constant obtained from Ref.[1], and the surrounding medium is assumed to be vacuum, i.e., $\varepsilon_m = 1$. As expected, there are two extinction peaks in each spectrum, one located at wavelength $\lambda < 350$ nm, which corresponds to the transverse mode (TM) plasmon resonance λ_{TM}, i.e. the collective electron oscillation perpendicular to the long axis of the rod. The other peak is located at $\lambda > 350$ nm, which corresponds to the longitudinal mode (LM) plasmon resonance λ_{LM}, i.e. the collective electron oscillation along the axis. If the aspect ratio ξ is increased, λ_{LM} red shifts drastically while λ_{TM} blue shifts slightly. Similar to Ref.[64], λ_{LM} red shifts linearly with the aspect ratio ξ.

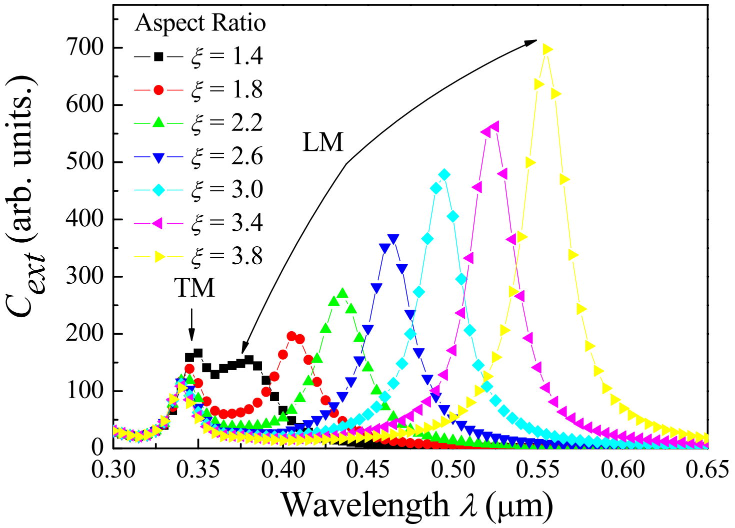

Figure 1.2 Extinction cross sections C_{ext} of randomly orientated spheroids with different aspect ratio calculated by Gans theory.

1.4 Discrete dipole approximation method

Both Mie theory and Gans theory give analytic extinction coefficient for regular shaped nanoparticle. For arbitrary shaped particles, i.e. besides spheres and spheroids, there are no analytical solutions for the extinction coefficient. Numerical methods have been introduced to study the light scattering from particles with arbitrary shapes, including the discrete dipole approximation (DDA) [65-71], multiple multipole method (MMP) [72-75], the finite difference time domain method (FDTD) [76-81], and T-matrix method [82-90]. Each method has its own advantages and disadvantages. But for single nanoparticals of arbitrary shape and complex surrounding medium, DDA method has been proved to be accurate and more efficient.

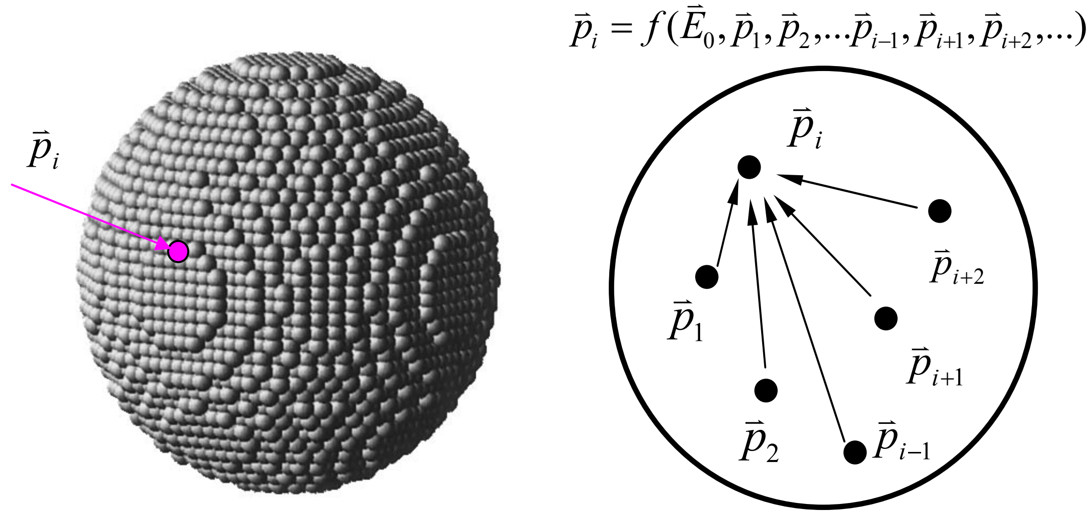

Figure.1.3 Schematics to illustrate discrete dipole approximation method

Discrete dipole approximation (DDA) is first introduced by Purcell and Pennypacker [67]. In this method, as illustrated in Fig. 1.3, a targeted particle is represented by an array of N dipoles with polarizability α_i located at position $\vec{r}_i$. The polarization of each dipole, $\vec{P}_i$, can be written as,

$$\vec{P}_i = \alpha_i \vec{E}_{loc}(\vec{r}_i), \tag{1.16}$$

where $\vec{E}_{loc}(\vec{r}_i)$ is the sum of the incident field $\vec{E}_{inc}(\vec{r}_i) = \vec{E}_0 e^{i\vec{k}\cdot\vec{r}_i - i\omega t}$ and the local electric fields generated by all the other N - 1 dipoles at location $\vec{r}_i$, as illustrated in Fig. 1.3.

$$\vec{E}_{loc}(\vec{r}_i) = \vec{E}_{inc}(\vec{r}_i) + \vec{E}_{dip,i} = \vec{E}_0 e^{ik\vec{r}_i} - \sum A_{i,j} \cdot \vec{P}_j\,, \tag{1.17}$$

where $\vec{P}_j$ is the dipole moment of the jth dipole, and $A_{i,j}$, with $i \neq j$, is a matrix element in a $3N\times3N$ interaction matrix, defined as,

$$A_{i,j} \cdot \vec{P}_j = \frac{e^{ikr_{ij}}}{r_{ij}^3}\left\{k^2 \vec{r}_{ij} \times (\vec{r}_{ij} \times \vec{P}_j) + \frac{(1 - ikr_{ij})}{r_{ij}^2}[r_{ij}^2 \vec{P}_j - 3\vec{r}_{ij}(\vec{r}_{ij} \cdot \vec{P}_j)]\right\}. \tag{1.18}$$

Substituting Eq. (1.17) and (1.18) into Eq. (1.16) and rearranging terms in the equation, one can have,

$$\vec{A}^{'} \cdot \vec{P} = \vec{E}\,, \tag{1.19}$$

where $\vec{A}^{'}$ is a matrix derived from matrix $\vec{A}$. By solving the $3N$ complex linear equations, the polarization of each dipole can be obtained, and the optical scattering and absorbance properties can be calculated. The extinction cross section C_{ext}, the absorption cross section C_{abs}, and the scattering cross section C_{sca} can be expressed as,

$$C_{ext} = \frac{4\pi k}{|\vec{E}_0|^2}\sum_{i=1}^{N} \operatorname{Im}(\vec{E}_{inc,i}^{*} \cdot \vec{P}_i)\,, \tag{1.20}$$

$$C_{abs} = \frac{4\pi k}{|\vec{E}_0|^2}\sum_{i=1}^{N}\{\operatorname{Im}(\vec{P}_i(\alpha_i^{-1}) \cdot \vec{P}_i^{*}) - \frac{2}{3}k^3 \vec{P}_i \cdot \vec{P}_i^{*}\}, \tag{1.21}$$

$$C_{sca} = C_{ext} - C_{abs}\,. \tag{1.22}$$

The scattering E field is the sum of the incident field and the dipole field of all dipoles which is given by

$$\vec{E}_{dipole} = \frac{e^{ikr}}{r^3}\left\{k^2\vec{r}\times(\vec{r}\times\vec{P}) + \frac{(1-ikr)}{r^2}[\vec{r}^2\vec{P} - 3\vec{r}(\vec{r}\cdot\vec{P})]\right\}. \quad (1.23)$$

The E field enhancement ($\gamma = |\vec{E}|^2 / |\vec{E}_0|^2$) calculated by DDA may have an uncertainty factor of 2 to 3 compared to Mie theory for a sphere [91]. However, when the same lattice parameter is used, it is reasonable to investigate the relative effect of particle shape or particle size on the absorbance spectrum and the E field distribution.

One of the effective and efficient methods to solve the Eq. (1.19) is to use the complex-conjugate gradient method (CCG method) [92, 93]. In brief, beginning from an initial guess $\vec{P}_i^{(0)}$, the CCG method generates a sequence $\vec{P}_i^{(n)}$, where n = 1, 2, …, that converges monotonically for estimate $\vec{P}$ until Eq. (1.19) is solved to some error criterion. The error tolerance may be specified as:

$$\frac{|A^+AP - A^+E|}{|A^+E|} < h, \quad (1.24)$$

where A^+ is the Hermitian conjugate of A, and h is the error tolerance. We typically use $h = 10^{-5}$ in order to satify Eq. (1.24) to high accuracy.

The DDA calculation results are strongly dependent on the dipole polarizabilities. Draine and Goodman established the lattice dispersion relation (LDR) method to prescribe the dipole polarizabilities [69]. Not only the dielectric constants but also the direction of the propagation and the polarization state of the incident polarization are also considered in LDR. By choosing these dipole polarizabilities, the infinite lattice of point dipoles will propagate electromagnetic plane waves with the same dispersion relation as in a medium of specified dielectric constants.

$$\alpha^{LDR} = \frac{\alpha^{CM}}{1 + (\alpha^{CM}/d^3)[(b_1 + m^2 b_2 + m^2 b_3 S)(kd)^2 - (2/3)i(kd)^3]}, \quad (1.25)$$

where m is the refractive index and α^{CM} is the Clausius-Mossotti polarizabilities in the infinite wavelength limit of the DDA, i.e., $kd \to 0$ [67],

$$\alpha^{CM} = \frac{3d^3}{4\pi}\frac{\varepsilon - 1}{\varepsilon + 2}, \tag{1.26}$$

and b_1 = -1.891531, b_2 = 0.1648469, b_3 = -1.7700004, and S is a function of the propagation direction and the polarization of the incident wave.

$$S = \sum_{j=1}^{3} (\hat{a}_j \hat{e}_j)^2 , \tag{1.27}$$

where $\hat{a}$ and $\hat{e}$ are unit vectors defining the incident direction and the polarization state. Extensive DDA calculation for spheres, comparing with different dipole polarizability, proved that LDR appears to be best for $|m|kd < 1$ [94].

There are two obvious criteria for the validity of the DDA method. First, $|m|kd < 1$. However, if accurate calculations of the scattering phase function are desired, a more conservative criterion $|m|kd < 0.5$ is needed. Second, the lattice spacing must be small enough to describe the target particle satisfactorily.

In summary, the DDA method divides the targets into an array of polarized cubes (dipoles). The induced polarizations of each dipole by the incoming E field can be solved from a self-consistent equation. The optical properties of the targets can be obtained from the polarization induced by all dipoles. This method is conceptually simple and can yield accurate results when the number of dipoles used to approximate the target is increased. DDA method has already been applied in many difference systems, such as the scattering of interstellar [95], interplanetary dust grains [96], ice crystals [97], human blood cells [98], and metal particles [64, 99]. The accuracy of the DDA method has been tested by a lot of researchers. DDA results were compared with those from other methods [100-102], Nordin *et al.* compared DDA result with result from exact Mie solution for spheres [100]. They also compared DDA's results with those from electrostatics method for spheroids. Jensen *et al.* compared DDA's result with result from Modified long wavelength approximation (MLWA) method for spheres and spheroids [101]. Yang *et al*. compared DDA's results with T-matrix's results for spheroids [102]. These comparisons all show that the results from DDA method are in good agreement with the results calculated from other methods.

In this study we follow Flatau [103] and use the public open source program, DDSCAT code [104], to solve the complex linear Eq. (1.19) for different shapes of Ag nanostructures.

1.5 Organization of this dissertation

This dissertation is organized as the following:

Chapter 2 systematically investigates the optical properties of the cylindrical Ag nanorods with different diameters and aspect ratios using DDA method. The plasmon peak, the multipole mode, the anisotropic extinction properties are calculated. Those results are compared to the results obtained from Gans theory.

Chapter 3 investigates the extinction spectra and the *E* field enhancement distributions of Ag nanorods with different topologic shapes, such as the needle-shape, period-shape, L-shape, Y-shape, and U-shape. To understand the anisotropic SERS signal and polarization dependent extinction spectra, the angular dependent optical properties are also studied.

Chapter 4 systematically investigates the optical properties of the Ag helical nanostructures. We studied the incident polarization dependent extinction spectra and the *E* field enhancement distributions. The structural parameter dependent optical properties are also investigated, such as the pitch height and the total helix height.

Chapter 5 summaries this dissertation and gives a vision for future work in the optical property of metal nanostructures.

CHAPTER 2

OPTICAL PROPERTIES OF AG NANORODS

2.1 Introduction

Recently, large SERS signals have been discovered from Ag nanorod/nanowire arrays by several research groups [105-108]. Tao *et al.* found that aligned Ag nanowires with a 45 ± 5 nm diameter and a 1.57 ± 0.07 μm length gave an enhancement factor of $\sim 10^9$ when probing Rhodamine 6G [105], and both the Raman signal and the UV-Vis had a strong polarization dependence, which may be due to the shape anisotropy and large electromagnetic fields localized in the interstitials between adjacent nanowires. Stephen *et al*. also achieved a SERS enhancement factor of approximately 10^8 when probing trans-1, 2-bis (4-pyridyl) ethylene and using a silver rod array substrate with a length of 508 nm and the diameter of 80-90 nm fabricated by a so-called oblique angle deposition [106]. They also showed that the anisotropic polarized SERS signals were consistent with the topological anisotropy of the nanorod arrays [107]. The stronger SERS signal appears perpendicular to the long axis of the nanorod arrays, while the maximum absorbance at the excited wavelength was observed along the direction of the long axis [107]. Although the nanorods have been investigated for their better ability to couple light to resonant collective electron plasmon oscillations than film and bulk material [5, 7], theoretically, for most investigations, the nanorod is approximated as an elongated spheroid, and its extinction propertyis usually described by Gans theory [62]. The basic assumption for Gans theory is that the size of the rod is much smaller than the incident wavelength and can be considered as a single dipole.

Experimentally, in the contrary, most research groups found that Ag nanorods with larger diameter and longer length in fact gave the best SERS enhancement [106, 109]. For example, the Ag nanowires made by Tao *et al.* are ~ 1.6 μm long and 45 nm in diameter [109] and the silver nanorods used by Chaney *et al*. have a length of 508 nm and diameter of 80-90 nm [106, 110-112]. Those sizes are not small comparing to incident wavelength for Raman experiments and in general, thus the nanorods should not be considered as a single dipole, as assumed by the Gans theory. Therefore, the results obtained from Gans theory may not be accurate to describe the optical properties of those larger nanorods. A better way to investigate the extinction properties of those nanorods is to use a numerical method. We would like use DDA method. Although, others calculated Ag optical properties using DDA method, most DDA calculation on Ag nanoparticles impose volume constraints [113, 114]. The total volume of the nanoparticle or nanorod is fixed while the aspect ratio or the shape is varying. For theoretical investigations, this constraint can clearly demonstrate how the parameters such as aspect ratio or shape, affect the extinction spectra. However, experimentally, both the aspect ratio and the volume of a nanoparticle will change during the growth process. For example, the diameter and the length of the Ag nanorod array prepared by the oblique angle deposition method can be tuned by controlling the deposition conditions, such as deposition rate and time [106]. Thus, the change of the optical absorbance spectra is not only a reflection of the change of the aspect ratio, but also the change of the volume as well as the diameter of the nanorods. One cannot separate those parameters individually like the theoretical investigation. The combination effect of both the aspect ratio and the diameter in the experiments will lead to some complications in interpretation of the extinction spectra. Yet, so far, a systematic and theoretical investigation of the extinction spectra of Ag nanorods with the change of both the aspect ratio and the diameter is not available.

In this chapter, we present a systematic study on the optical properties of Ag nanorods with different diameter and aspect ratio using DDA method. The plasmon peaks, the multipole mode, the anisotropic extinction properties are calculated.

2.2 Extinction spectra calculated by DDA

In the literature, we find that most calculations for Ag nanostructures use the bulk dielectric constants data from two different sources [1, 2]. In order to investigate how the two sets of dielectric constants affect DDA results, we have calculated the extinction cross section C_{ext} of a cylindrical Ag nanorod with a diameter D = 20 nm and an aspect ratio ξ = 2 at *p*-polarization incidence and *s*-polarization incidence using these two different sets of dielectric constants. As shown in Fig. 2.1, the incident direction is perpendicular to the long axis of the Ag nanorod. The *p*-polarization is defined when the *E* field of the incident light is parallel to the nanorod, and the *s*-polarization is defined when the *E* field is perpendicular to the nanorod axis.

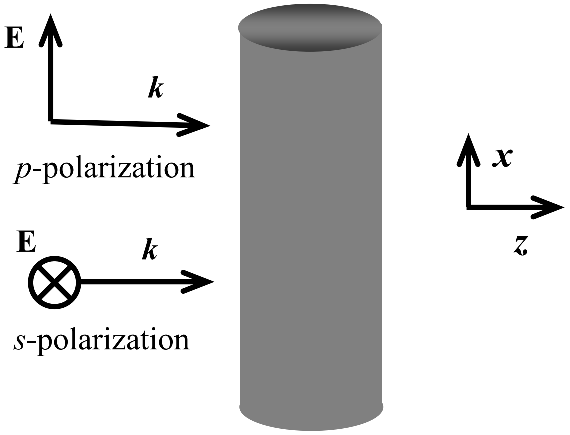

Figure 2.1 Schematic for *p*-and *s*-polarization incidence on an Ag nanorod

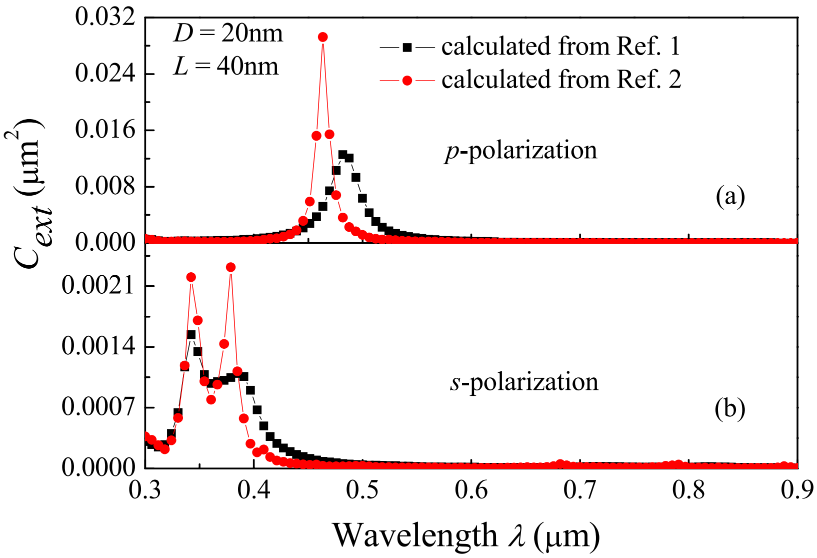

Figure 2.2 Extinction cross section C_{ext} of D = 20nm and L = 40nm Ag nanorod calculated by DDA method using two sets of dielectric constants from Refs [1] and [2]. (a) at p-polarization incidence (b) at s-polarization incidence

The nanorod was divided into 5310 dipoles and the lattice spacing d = 1.33 nm. The extinction cross sections C_{ext} as a function of the wavelength are plotted in Fig. 2.2. For p-polarization incidence, results from both sets of dielectric constants give a single plasmon peak (longitudinal mode, LM). However, the location, amplitude, and the width of the resonant peaks are different. The plasmon peak using data from Ref.[1] is located at λ_p = 0.483 μm, while the peak calculated using data from Ref.[2] is located at λ_p = 0.463 μm. These two peaks have a wavelength difference of ~ 20 nm. For s-polarization incidence, both spectra exhibit double peaks at a UV wavelength region. Similar to the p-polarization incidence, the location, amplitude, and the width of these two peaks are different. The two peaks calculated from Ref.[1] are located at 0.343μm and 0.380μm, respectively, and the separation between these two peaks is 37nm, while the two peaks calculated from Ref.[2] are at 0.345μm and 0.378μm, respectively, and the separation is 33nm. For *p*-polarization and *s*-polarization incidences, the plasmon peaks calculated from Ref.[2] are always sharper and stronger than those from Ref.[1]. From these two figures, we find that plasmon peaks calculated from Ref.[2] are always sharper than those from Ref.[1]. Although the results calculated from two dielectric constants are quantitatively different, they are qualitatively the same. In our calculation, we adapt the dielectric constant from Ref.[1] since the dielectric data extend to longer wavelength range.

In order to explore the effect of both the diameter and the aspect ratio on the extinction spectra, we have calculated the C_{ext} of Ag nanorods with four different diameters, D = 20, 40, 60, and 80 nm, respectively, and various aspect ratios. The configuration of the incident light and the definition of polarizations are shown in Fig.2.1. We divide the calculations into two groups: short nanorods (ξ = 1 – 4, i.e., L = 20 – 320 nm) and long nanorod (ξ > 6, L = 500 nm, 600 nm, 700 nm, 800 nm, and 1000 nm, respectively). The results for the short nanorods will be used to compare with the results obtained from Gans theory since the size is smaller than the wavelength. During the DDA calculation of short nanorods, for nanorods with the same diameter but different aspect ratio, we use the same lattice space, i.e. the total number of dipoles for a nanorod being proportional to its length L. Table 2.1 summarizes the total number of dipoles used for the DDA calculation for short nanorods with different ξ.

Table 2.1 Total dipole number of short nanorods ($\xi \leq 4$)

R	1.0	1.5	2.0	2.5	3.0	3.5	4.0
# of dipoles	2655	4071	5310	6726	7965	9381	10620

Table 2.2 Dipole number and lattice space for long nanorods ($\xi > 4$)

L *D*	500nm	600nm	700nm	800nm	1000nm	*d*
20nm	10400	12480	14560	16640	20800	2.47nm
40nm	10000	12000	14000	16000	20000	3.98nm
60nm	6640	8000	9360	10640	13360	5.97nm
80nm	8400	10080	11760	13440	16800	6.69nm

The lattice space d of dipoles for different diameters $D = 20$, 40, 60, and 80 nm are $d =$ 1.333, 2.675, 3.998, and 5.331 nm, respectively. Table 2.2 summarizes the total number of dipoles used and corresponding unit dipole diameters for long nanorods. For different diameter nanorods, the size of the unit dipole is different, but the requirement for the DDA method, $|m|kd < 1$ (m is complex refractive index of Ag, and $k = 2\pi/\lambda$ is the wavenumber) is fulfilled. Under this condition, different size dipoles will only shift the plasmon resonant wavelength slightly (a few nanometers) [100]. Thus, with the exception that the exact plasmon resonant wavelength may not be accurate (± few nanometers), the changes of the plasmon wavelength and the absorbance as functions of the nanorod diameter D and aspect ratio ξ will be well described.

2.3 Results of DDA calculations

2.3.1 The extinction coefficient C_{ext} of small aspect ratio Ag nanorods ($\xi \leq 4$)

The extinction cross sections C_{ext} of nanorods with D = 20, 40, 60, 80 nm and aspect ratios $\xi \leq 4$ were calculated for both *p*-polarization and *s*-polarization incidence.

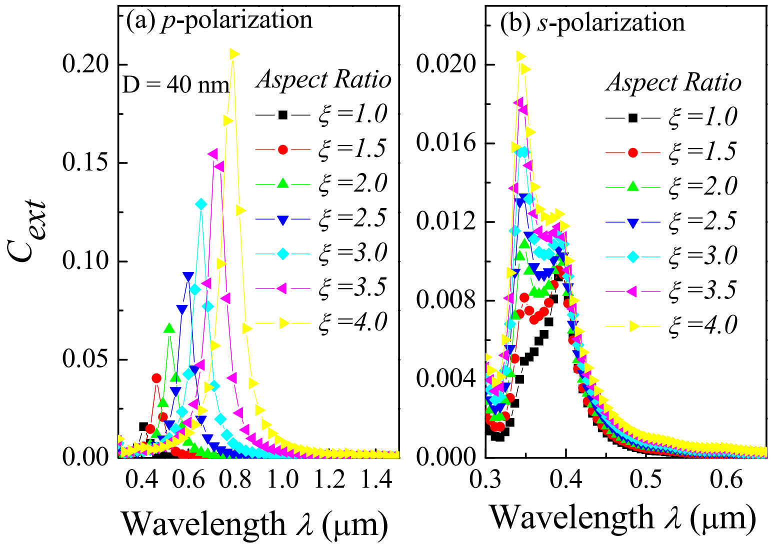

Figure 2.3 Extinction cross section C_{ext} of D = 40nm nanorods calculated by DDA method (a) at *p*-polarization incidence (b) at *s*-polarization incidence

Figure 2.3 plots C_{ext} spectra of Ag nanorods with D = 40 nm for aspect ratios ξ from 1 to 4. For *p*-polarization incidence, as shown in Fig. 2.3 (a), there is only one extinction peak in each of the spectra, which corresponds to the LM plasmon resonance. With the increase of the aspect ratio ξ, the resonant wavelength λ_{LM} red shifts, the amplitude of the resonant peak increases, and the width of the resonant peak increases as well. This result agrees qualitatively with that obtained from Gans theory (Fig. 1.2). For *s*-polarization incidence, as shown in Fig. 2.3 (b), the C_{ext} spectrum exhibits two extinction peaks, one at a longer wavelength (called transverse dipole mode, TDM) and the other at a shorter wavelength (called transverse quadrupole mode, TQM)[99]. This double-peak feature is not observed in Fig. 1.2. The amplitudes of both TDM and TQM peaks increase with ξ and the relative extinction amplitude changes as well. When the

ξ varies from 1 to 1.5, the intensity of the TDM peak is stronger than that of the TQM peak. When $\xi \geq 2.0$, the peak intensity of TQM is stronger than that of TDM. We also find that the TQM mode blue shifts and TMD mode red shifts slightly with ξ. However, since the peak intensity of TMQ is stronger, the overall shift of peak position is blue, but will not be as significant as the red shift of λ_{LM}, which is consistent with Gans theory.

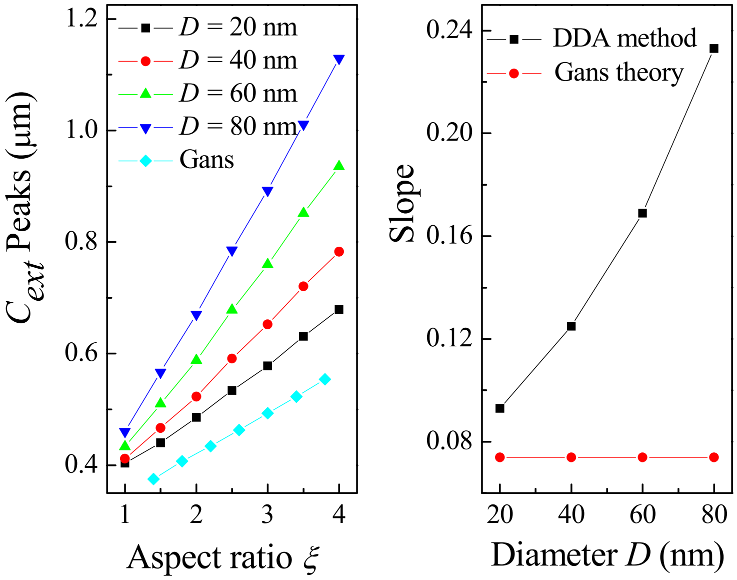

Figure 2.4 LM plasmon resonant wavelengths as a function of the aspect ratio ξ of nanorod for different diameters D (b) the slope of linear curve in (a) changes with diameter D

To illustrate the effect of the nanorod diameter on the plasmon resonant peak, Figure 2.4(a) plots λ_{LM} obtained from the DDA calculations as a function of ξ. The λ_{LM} calculated from Gans theory (Fig. 1.2) is also plotted in Fig. 2.4 (a). All the curves in Fig. 2.4 (a) share one comment feature, that is, λ_{LM} increases linearly with the aspect ratio ξ, which qualitatively agrees with the Gans theory. However, for the same aspect ratio, larger diameter nanorods have a larger λ_{LM}, and the λ_{LM} red shifts faster. The slope k (D) of the λ_{LM} shift for different nanorod diameters is obtained from Fig. 2.4(a) using the fitting equation $\lambda_{LM} = k(D)\cdot\xi + \lambda_0$ and is plotted in Fig. 2.4(b).

For the short nanorods, we find that the absorption process dominates the extinction spectra and the contribution of scattering is very small. For example, Figure 2.5 plots in semi-log scale the ratio of the absorption cross section C_{abs} to the scattering cross section C_{sca} for Ag nanorods with the same diameter D = 20 nm and at ξ = 1 and ξ = 4. For both ξs, the ratio C_{abs}/C_{sca} is larger than 1, and with the increase of R, the ratio C_{abs}/C_{sca} decreases, which demonstrates that the scattering becomes more and more important.

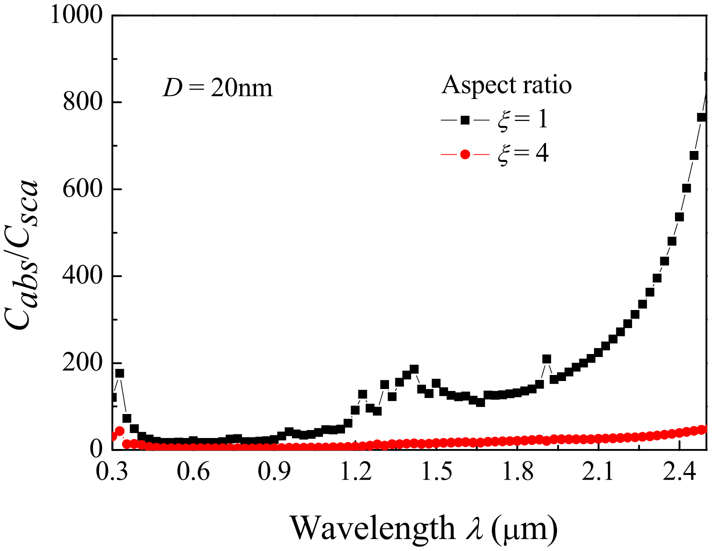

Figure 2.5 The ratio of absorption cross section C_{abs} to scattering cross section C_{sca} for two different Ag nanorods, D = 20nm, ξ = 1 and D = 20nm, ξ = 4

The above results can be understood qualitatively through the classic electromagnetic theory. When the volume of the nanorod becomes smaller, only the dipole oscillation /absorption contributes significantly to the extinction. Therefore, the C_{ext} calculated from the DDA is close to that of Gans theory. However, when the size of the Ag nanorods increases, the scattering effect becomes more important. The red shift of the plasmon resonance is due to a so-called "dynamic depolarization effect", which relates to the interaction from radiation emitted at different points in the particle. Dynamic depolarization results in a strong red shift of dipolar plasmon resonance [115, 116]. The dynamic depolarization depends strongly on the total volume of the particle. For the same aspect ratio nanorods, when ξ increases, the total volume ($V = \pi\xi D^3 / 4$) of nanorods with larger diameters increases faster than that of smaller diameter nanorods. This is the reason why the plasmon peak of longer diameter nanorods red shifts faster than shorter diameter nanorods. The broadening of the plasmon peak is caused by a so-called radiation damping effect, which is due to the damping of the dipole through radiation loss. For small particles, the effect of radiation resistance can be neglected. When the size becomes bigger, the radiation fields must be taken into account. The radiation damping effects reduces the intensity, makes the peak asymmetric, and broadens the peak [115, 117].

The nature of the extinction of a nanorod is due to the forced oscillation of electrons inside the Ag nanorod. This oscillation is determined by the induced charge distribution in the nanorod. If the nanorod is small, and the induced charge distribution is uniform, the entire nanorod can be treated as a dipole. This is particularly true when the size of the nanorod is smaller than the incident wavelength. The angular distribution of the far field scattering intensity is a good way to judge the nature of the plasmon resonance. In order to further understand the physical nature of the extinction of the Ag nanorods, we have investigated the angular distribution of the scattered far field intensity of nanorods. When the size of a nanorod is much less than the incident wavelength, the nanorod can be considered as one dipole. This is the basic assumption for Gans theory. For a dipole with polarization proportional to the incident field, according to the Rayleigh scattering approximation, the angular distribution of the scattering intensity in horizontal plane can be written as the following [118],

$$I_{sca}(\theta) = \frac{k^4 \alpha^2}{r^2} I_0 \cos^2 \theta \,, \tag{2.1}$$

where α is the polarizability of the dipole/nanorod, and θ is the angle between the scattering beam and the incident beam. The scattering intensity I_{sca} is collected within the plane of the incident E field and the incident direction, and I_0 is the incident intensity. Thus, the horizontal scattering intensity $I_{sca}(\theta)$ has a $\cos^2(\theta)$ distribution. This is a characteristic for dipole excitation. However, if the induced charge has a quadrupole distribution and the charge has an oscillating spheroidal distribution, then $I_{sca}(\theta)$ will have the form of [119].

$$I_{sca}(\theta) = \frac{ck^8 Q^2}{r^2} \cos^2(2\theta) \,, \tag{2.2}$$

where Q is the nonzero term in the electric quadrupole moment, and c is a constant which does not relate to the wavelength or the scattering direction. The angular distribution is different from that of the dipole. Thus, the angular distribution of the far field scattering intensity $I_{sca}(\theta)$ is a reflection of the nature of the extinction of a nanorod.

Since the extinction spectra calculated by the DDA for Ag nanorods with different diameters and aspect ratios are different from those obtained from Gans theory, one may expect that the angular distribution of the scattering intensity may be different as well. Therefore, we calculated the $I_{sca}(\theta)$ of an Ag nanorod with D = 40 nm and ξ = 4 at p-polarization incident for λ = 0.5 µm, 2.0 µm and 0.783 µm, respectively (Figs. 2.6(a), (b), and (c)). The reason we chose those particular wavelengths is that from Fig. 2.3, λ = 0.783 µm is the LM resonant peak for this particular nanorod. One notices that all three of the angular distributions have similar shapes: the intensity reaches a maximum when $\theta = 0^\circ$ and 180°, and it hits a minimum when $\theta = 90^\circ$. This is quite similar to the situation depicted by Eq. (2.1). Therefore, we used equation

$$I_{sca}(\theta) = A \cos^2 \theta \tag{2.3}$$

to fit the scattering intensity (the solid curves in Figs. 2.6(a), (b), and (c)). The goodness of the fitting shows that the nanorod at these three different wavelengths behaves like a dipole. In addition, it is noticed that the scattering intensity at λ_{LM} = 0.783 µm is much stronger than those at the other two wavelengths, which is due to the plasmon resonance. We also calculated the $I_{sca}(\theta)$ of the same Ag nanorod at *s*-polarization incident for λ_{TDM} = 0.383 µm, λ_{TDM} = 0.344 µm, and λ = 0.45 µm, respectively (Figs. 2.6(d), (e), and (f)). The $I_{sca}(\theta)$ at all three different wavelengths has similar shapes as those for the *p*-polarization incident. For *s*-polarization incident, the incident electric field oscillates perpendicular to the long axis of the nanorod. Because the diameter of the nanorod is much smaller than the incident wavelength, the nanorod can be polarized homogenously along the short axis. However, due to the anisotropic nature of the nanorod, one cannot treat the rod as a single dipole. One can use the Rayleigh-Gans-Debye approximation to treat the rod [118]. This approximation assumes that the internal field in the rod is not altered by the presence of the particle and is identical to the incident wave and each infinitesimal part of the particle acts independently as a Reyleigh scatter. Thus, a series of parallel dipoles perpendicular to the long axis can be used to approximate the scattering intensity for TM incidence, and the scattering intensity in *y*-*z* plane can be written as,

$$I_{sca}(\theta) = F' \frac{I_0 k^4}{r^2} \cos^2\theta [\int_{-L/2}^{L/2} e^{-ikx\cos\varphi} dx]^2 \tag{2.4}$$

where φ is the angle between the infinitesimal Reyleigh scatter and scattering direction. F' is the fitting parameter. The solid curves in Fig.2.6 (d), (e), and (f) are the results of the fitting, which demonstrates that the Rayleigh-Gans-Debye approximation works well. We also notice that the scattering intensity $I_{sca}(\theta)$ at both λ_{TDM} and λ_{TQM} are much stronger than that at off-resonant wavelength.

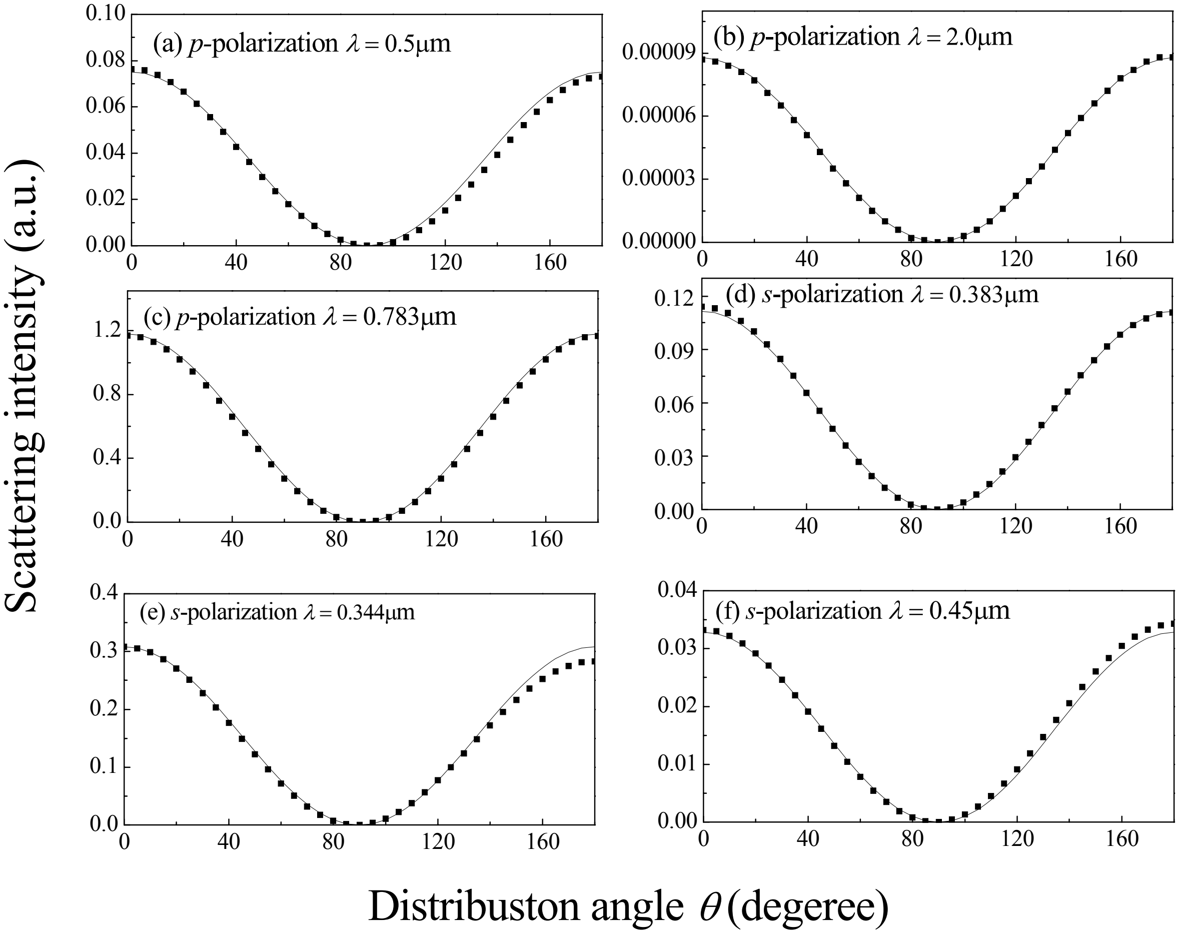

Figure 2.6 The angular distribution of scattering intensity in *x*-*z* plane at *p*-polarization incidence with different incident wavelength (a) λ = 0.5 μm, (b) λ = 2.0 μm, and (c) λ = 0.783 μm, and the angular distribution of scattering intensity in *y*-*z* plane in Fig. 2.1 at *s*-polarization incidence with different incident wavelength (d) λ = 0.383 μm, (e) λ = 0.344 μm, and (f) λ = 0.45 μm (Solid curves are calculated by fitting).

Thus, the angular distribution of scattering intensity for both incident fields calculated from the DDA reveals that the Ag nanorods with small aspect ratio can be treated as dipoles, although the Gans theory does not predict quantitatively the same extinction behavior for those nanorods.

2.3.2 The extinction coefficient C_{ext} of larger aspect ratio Ag nanorods ($\xi > 6$)

The above results show that even at a small aspect ratio, the extinction cross section C_{ext} calculated by the DDA method exhibits a strong dependence on the diameter of the nanorods. Therefore, it would be interesting to see how the larger aspect ratio affects the C_{ext} for Ag nanorods with different diameters. The *p*-polarization extinction spectra of Ag nanorods with fixed L = 500 nm length and different diameter D = 20, 40 and 60 nm (ξ = 25, 12.5, and 8.33, respectively), are shown in Fig. 2.7. Comparing those spectra to the spectra for smaller aspect ratio nanorods (Fig. 2.3), the main LM plasmon resonant wavelengths λ_{LM} red shift further. For the same nanorod length, the larger aspect ratio nanorods shift λ_{LM} further. For example, the λ_{LM} for nanorods with ξ = 25 shifts beyond 2.5 μm. Despite the large extinction peak for the LM plasmon mode, at short wavelength, there are other additional extinction peaks that appear, as shown in the insert of Fig. 2.7. Those are the peaks that are not observed for small ξ. For nanorod with ξ = 8.33, two dominant peaks have been observed at λ = 0.588 μm, and λ = 0.436 μm, respectively. For nanorod with ξ = 12.5, two peaks have also been observed, at λ = 0.678 μm, and λ = 0.491 μm, respectively. However, for nanorods with ξ = 25, three dominant peaks have been observed at λ = 1.019 μm, λ = 0.675 μm, and λ = 0.539 μm, respectively. Another characteristic of those peaks is that, when the peak position separates further from the main resonant wavelength λ_{LM}, the extinction becomes smaller. We use the notation l to label all the extinction peaks: l = 1 denotes the main plasmon peak, l = 2 denotes the nearest extinction peak near main peak, and so on. In the literature, those extinction peaks with $l \geq 2$ are assigned as multipole plasmon resonant peaks [120], where l = 1 represents the dipolar plasmon peak and l = 2 represents the quadrupole plasmon peak and so on.

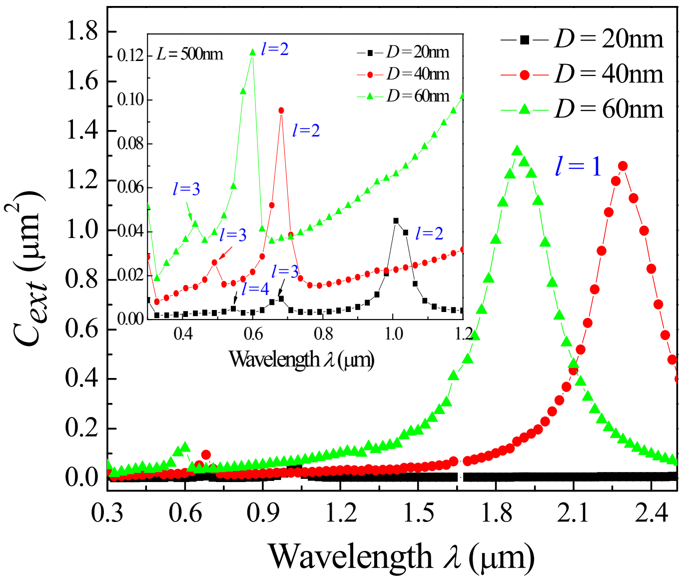

Figure 2.7 Extinction cross section C_{ext} of L = 500 nm, D = 20, 40, 60 nm Ag nanorods calculated by DDA method, the insert figure plots the extinction spectra at short wavelength region.

In order to understand the nature of those resonant peaks, we have also investigated the angular distribution of scattering intensity $I_{sca}(\theta)$. Figure 2.8 plots the far field scattering intensity distribution for an Ag nanorod with D = 20 nm and $\xi = 25$ at $\lambda = 2.5$, 1.2, 1.0, 0.9, and 0.675 μm, respectively. For $\lambda = 2.5$ and 1.2 μm, the wavelength is in between the two major resonant peaks, $l = 1$ and $l = 2$. Figures 2.8(a) and (b) show that $I_{sca}(\theta)$ is similar to those at lower R, i.e., Fig. 2.6, and Eq. (2.3) fits the data (solid curves in Fig. 2.8(a) and(b)) very well. This is characteristic of the scattering for a dipole. At $\lambda = 1.0$ μm, i.e., the resonant peak at $l = 2$, the shape of $I_{sca}(\theta)$ (Fig. 2.8(c)) is much different from those in Figs. 2.8 (a) and (b): although at $\theta = 0^o$ and 180^o $I_{sca}(\theta)$ reaches the maximum, the intensity drops very quickly to the minimum. The solid curve in Fig. 2.8(c) shows an attempted fitting using Eq. (2.3). Qualitatively Eq.(2.3) follows the trend of the data, however, the difference between the fitting and the calculated data shown in Fig. 2.8(d) exhibit a double period within 180^o. This difference is consistent with the angular distribution of the scattering intensity for a quadrupole, i.e., Eq. (2.2). Thus, at λ = 1.0 μm, the scattering intensity is a result of a combination from a dipole and a quadrupole. The shape of $I_{sca}(\theta)$ at λ = 0.9 μm (Fig. 2.8(e)) and at λ = 0.675 μm (Fig. 2.8(f)) can not be fitted by Eq. (2.3), demonstrating that there are higher order multipole effects other than dipole effect contributing to the scattering.

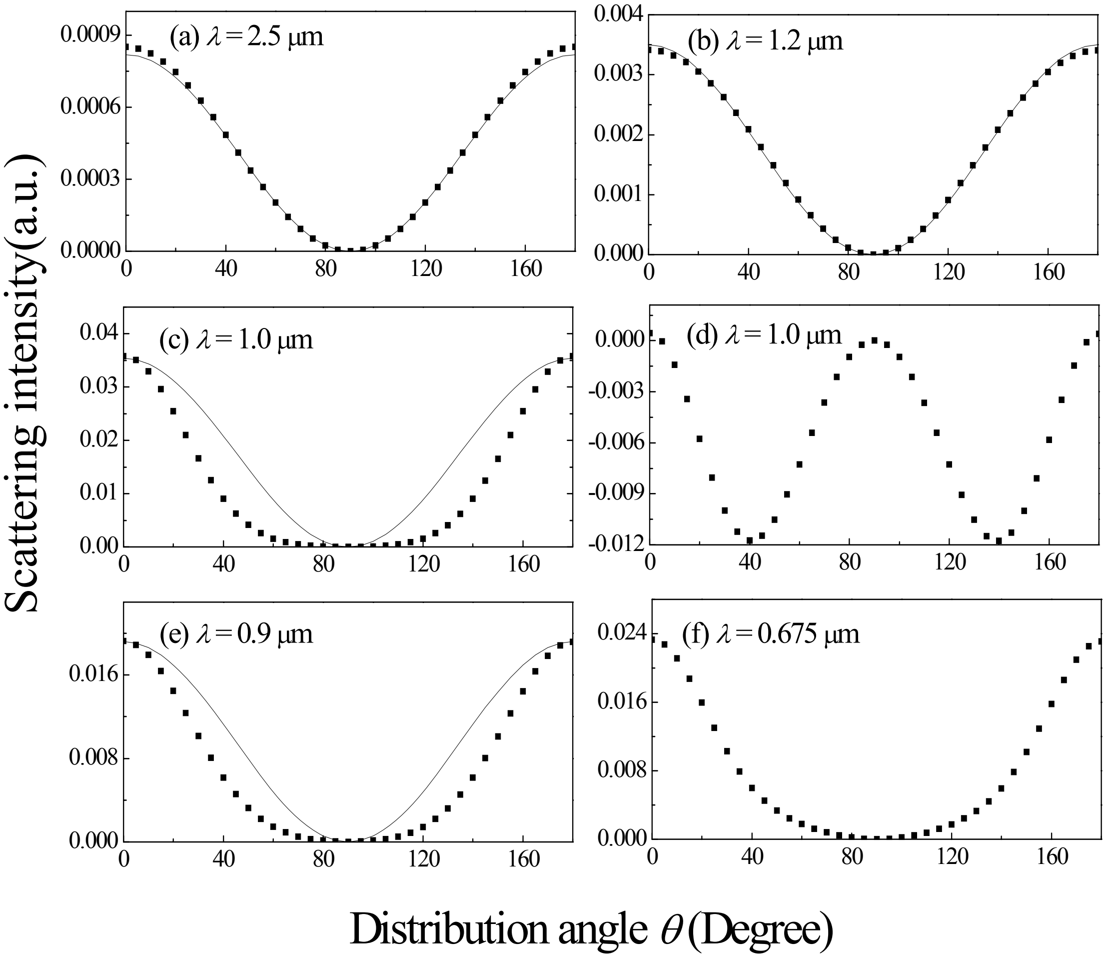

Figure 2.8 The angular distribution of scattering intensity in *x*-*z* plane at *p*-polarization incident with different incident wavelength (a) λ = 1.2 μm, (b) λ = 2.5 μm, (c) λ = 1.0 μm (d) the difference of approximation with the scattering intensity with λ = 1.0 μm incident, (e) λ = 0.9 μm, and (f) λ = 0.675 μm , the solid curves are the fitting.

The above results demonstrate that for large aspect ratio nanorods, when the wavelength is comparable to, or smaller than the length of the nanorod, the incident light cannot polarize the particle homogeneously, and higher-order plasmon modes appear in the extinction spectra. With increasing particle size, these higher-order modes become more and more important. These multiple well-separated plasmon resonant peaks are found at higher resonance frequencies than the resonance frequency of the dipolar plasmon excitation (not appearing in Fig. 2.7).

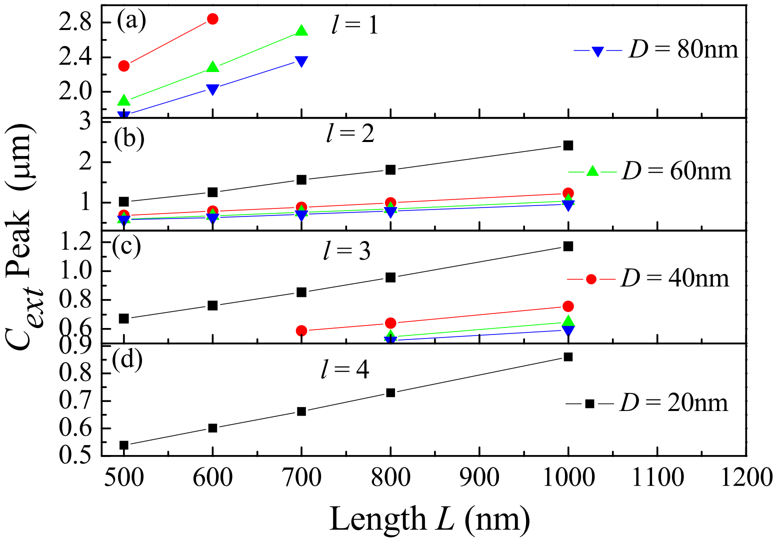

Figure 2.9 Multipolar plasmon peak wavelength as function of aspect ratio *R* for different diameter Ag nanorods at *p*-polarization incidence calculated by DDA

The resonant wavelengths for multipole plasmon also shift as aspect ratio and diameter (Fig. 2.9) [120]. For fixed nanorod diameters, multipole plasmon peaks red shift linearly with increasing aspect ratio. However, the dipole plasmon position is more sensitive to the aspect ratio of nanorod than other high order plasmon peaks. As for the same order multipole plasmon mode of nanorods with the same length, larger aspect ratio nanorods have larger resonant wavelengths. Because of the higher aspect ratio, for the same order multipole plasmon mode, the plasmon peak of smaller diameter nanorods linearly increase faster than larger diameter ones. For the same length nanorod, with a increasing aspect ratio of the nanorod, a higher order resonance appears. For example, for the D = 40 nm and ξ = 12.5 nanorod, there are two multipole modes: l = 2 and 3. When the aspect ratio increases to 25, the 4th order multipole mode appears.

For s polarization incidence, at longer nanorod length, the extinction spectra also exhibit two resonant peaks, TDM and TQM, as shown in Fig. 2.10(a). However, the TQM peak is much stronger than the TDM peak. With the increasing of the aspect ratio, both the intensities of TDM and TQM peaks increase. But the intensity of TQM peak increases faster than TDM peak.

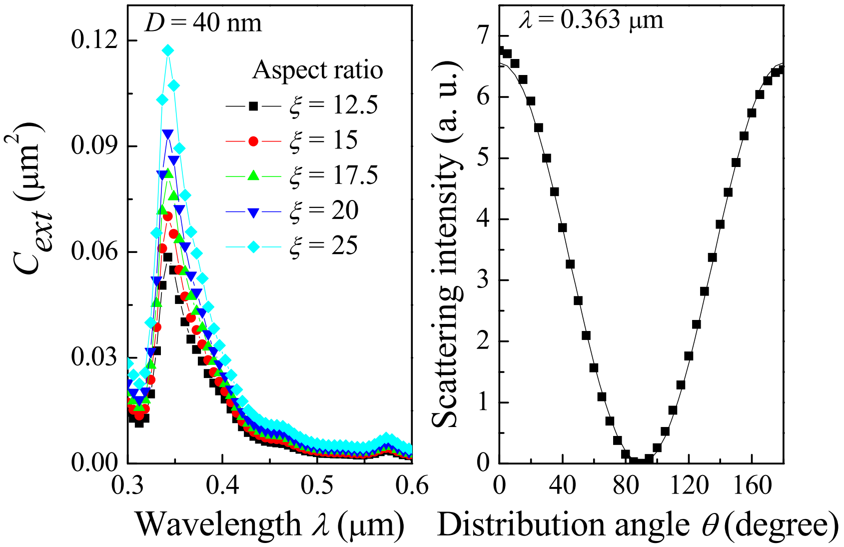

Figure 2.10 (a) Extinction cross section C_{ext} of Ag nanorod with D = 40 nm at s-polarization incidence calculated by DDA method, and (b) the angular distribution of scattering intensity in y-z plane of D = 40 nm and ξ = 25 nanorod with s-polarization incidence λ = 0.363 μm incidence. Solid curve is the fitting.

The angular distribution of the far field scattering intensity $I_{sca}(\theta)$ at λ_{TM2} = 0.363 μm for an Ag nanorod with D = 40 nm and ξ = 12.5 is calculated, and shown in Fig. 2.10(b). Since the diameter of the nanorod is smaller than the wavelength, one can still apply the Rayleigh-Gans-Debye approximation to fit the data. We also use a series of parallel dipoles to fit the intensity distribution using Eq. (2.4). The fitted curve is plotted as a solid line in Fig. *2.10*(b), and shows good agreement with the calculated data. Therefore, for long nanorods at *s* polarization incidence, the electric field can polarize the rod homogenously.

2.4 Conclusion

We have performed systematic numerical calculations of Ag nanorods using the DDA method. For short length nanorods, when light is incident with *p*-polarization, nanorods can be considered as an ideal dipole, the LM plasmon peak red shift linearly with the aspect ratio of Ag nanorods, and the rate of the resonant wavelength shift increases with the diameter of the nanorod. When light is incident with *s*-polarization, the nanorod can be considered as a series of parallel dipoles, and the TM mode of the Ag nanorod consists of two peaks. For even larger aspect ratios, the *p*-polarization light will induce a multipolar plasmon resonant mode. Multipolar plasmon peaks also increase linearly with the aspect ratio of nanorods and lower-order plasmon peaks increase faster than high-order plasmon peaks. For the same length Ag nanorods, the larger the diameter, the more blue shifted the multipolar plasmon resonance becomes with respect to the primary resonant wavelength.

CHAPTER 3

OPTICAL PROPERTIES OF NANORODS WITH DIFFERENT TOPOLOGIC SHAPES

3.1 Introduction

As a surface plasmon-mediated phenomenon, SERS is strongly dependent on the *E* field enhancement distribution. Usually, the maximum *E* field enhancement occurs at the surface or the tips. When the nanostructure becomes more complex, more plasmon peaks appear. For example, Hao *et al.* investigated the plasmon resonances of the gold star-shaped nanostructure[121]. They showed that different plasmon resonances had significant surface charges associated with individual tips and that the scattering intensities of different plasmon resonances strongly depend on the incident polarization. So far, most of the nanostructures studied are of simple geometrical shapes, such as triangle, squares, etc., with protruding corners. More complicated nanostructures with different topological shapes such as corners, recesses etc., have not been studied, yet those topological structures could greatly influence their plasmonic properties and can be fabricated experimentally.

Ag nanorod arrays can be fabricated through a so-called oblique angle deposition method and have been proved to have high SERS enhancement factors [106]. The SERS signal from nanorod array is also polarization dependent, and the SERS anisotropy is coincident with the appearance of the polarization dependent absorbance spectra of the substrate [107]. Figure 3.1 shows the polarization absorption spectra of an Ag nanorod array fabricated by oblique angle deposition method. Excitation light incidents normally to the substrate. When the incident polarization is parallel to the nanorod tilted direction, as the insert in Fig. 3(a), a very broad absorption peak appears at the visible wavelength region. When the incident polarization is perpendicular to the nanorod, a sharp absorption peak appears at the UV wavelength region.

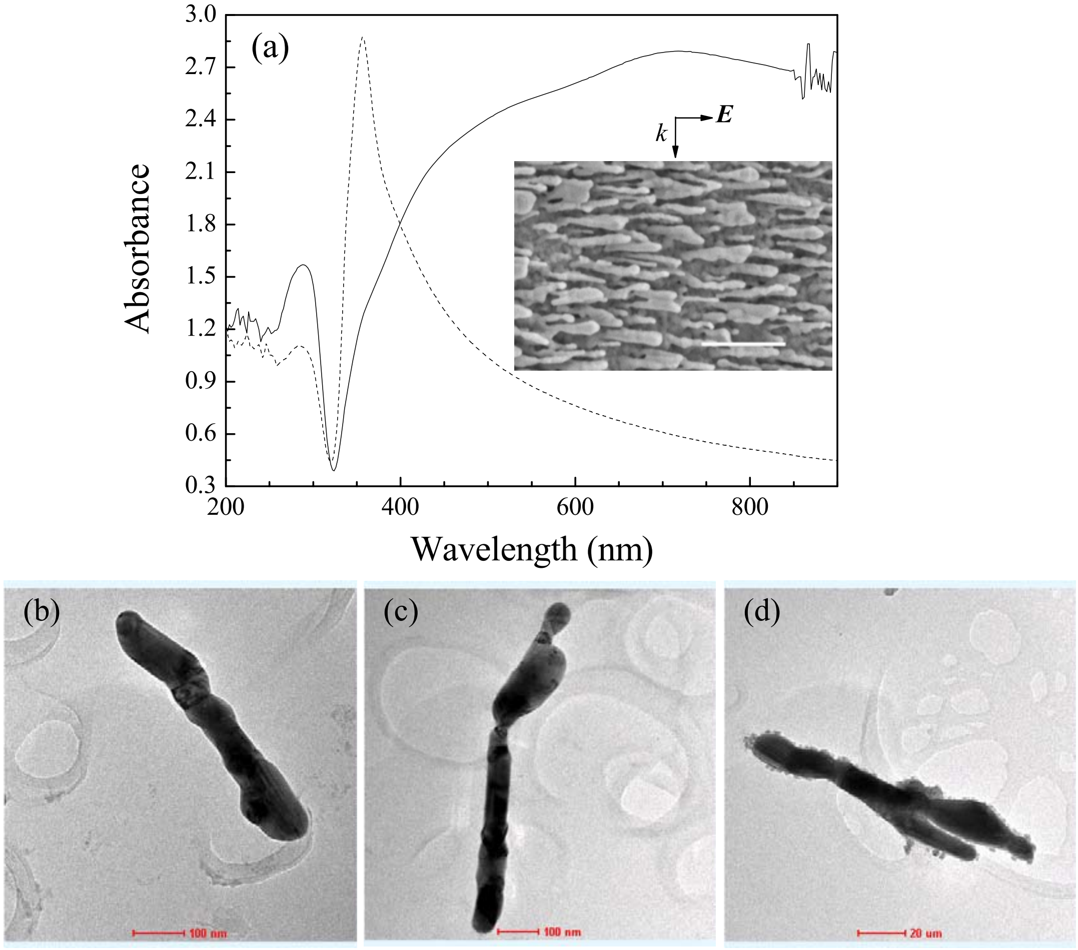

Figure 3.1 (a) The polarized absorbance spectra of Ag nanorod arrays fabricated by OAD method. The insert shows a sampling SEM image of the Ag nanorod array. (b) – (d) TEM images of individual Ag nanorods obtained from Ag nanorod substrate. They represent corrugation (b), bending (c), and (d) bifurcation, respectively.

Theoretically, those nanorod array substrates were treated as a spheroid nanorod array [122, 123], and their optical properties are modeled based on the anisotropic effective medium theory [123]. However, the nanorods in the array are not perfect spheroids; they have various shapes, such as corrugation, bending, and bifurcation. Those imperfections, or the three-dimensional topological structure, may significantly alter the optical properties. The three dimensional shaped nanorod structures can also be fabricated through a simple physical vapor deposition technique called glancing angle deposition (GLAD) [124-128]. By programming the substrate rotations, the nanorod array structures such as C shape and zigzag have all been fabricated [124-128]. Yet the ability to use this technique to tune the LSPR has not been reported. These nanostructures with different topological shapes could significantly tune the LSPR and may have significant effect on designing future plasmonic devices [129].

For the nanorod array substrate [106], a base layer of 500 nm Ag film is first deposited onto glass slides, and then Ag nanorod arrays are coated on top of the Ag film. Driskell *et. al.*. have investigated how the Ag base layer affects the Raman intensity [111]. The results show that the absolute Raman intensity of *trans*-1,2-bits(4-pyridyl)ethane (BPE) for silver nanorods on Ag film is three orders of magnitude stronger than that for silver nanorods on bare glass slides. This result demonstrates that when the additional Ag base layer is added, there could be stronger *E* field coupling between the Ag film layer and the nanorods; and more SERS hot spots could be generated in between the Ag film and Ag nanorods. So far, theoretically, the effect of the underlying Ag film on the optical property of the SERS substrate is not known. Structurely, the aligned nanorod arrays on an Ag thin film can be treated as a blanket structure and the simple unit in one dimension for such a structure is a U-shaped nanostructure. Once such U-shaped structure is arranged in a two-dimensional fashion, one obtains the Ag nanorod array substrate.

Thus, the optical properties of U-shaped nanostructures could shine some light on the understanding of the film effect and can be used as a crude model for the Ag nanorod SERS substrate.

In this chapter, extinction spectra and the *E* field enhancement distributions of the needle-shaped nanorods, the period-shaped nanorods, the *L*-shaped nanorods, and the *Y*-shaped nanorods are compared with those of cylindrical nanorods. The extinction spectra and the *E* field enhancement distributions of the U-shaped nanorods are compared with those of the parallel-nanorod structure. In order to understand the anisotropic SERS signal and polarization dependent extinction spectra, the angular dependent optical properties are also studied.

3.2 Cylindrical nanorods

The cylindrical Ag nanorods used in the calculation has a diameter of 20 nm and the length varies from 40 to 160 nm. As shown in Fig. 2.1, light propagates perpendicular to the nanorod axis. The *p*-polarization is defined as the *E* field along the cylindrical nanorods long axis. The *s*-polarization is defined as the *E* field perpendicular to the long axis.

Figure 3.2(a) plots the extinction efficiencies of cylindrical nanorod with *p*-polarized incident light. When the length *L* increases from 40 to 120 nm, there is only one extinction peak at the wavelength λ_p = 0.485, 0.681, and 0.873 μm for *L* = 40, 80, and 120 nm, respectively, in each of the spectrum, resulting from the longitudinal mode (LM) of LSPR. When the length increases to 160 nm, besides the main plasmon peak at λ_p = 1.084 μm (LM mode), another small peak appears at λ = 1.274 μm. With the increase of the length, the resonant wavelength of LM mode is red shifted linearly as shown in Fig. 3.3, which is well known from Gans theory[62, 64]. Figure 3.2(b) presents the *E* field enhancement distribution γ ($\gamma = |E_l|^2 / |E_0|^2$, where E_l is the local field and E_0 is the incident field) of a cylindrical nanorod with L = 80 nm at λ_p = 0.681 μm. A dipole-like E field is demonstrated, and the maximum enhancement occurs at the tips of the cylinder, which is consistent with the so-called lightening-rod effect. Other cylindrical nanorods with different lengths at λ_p have similar E field distribution. At off-resonance wavelength, for example, for L = 160 nm and λ = 1.274 μm, there is also a dipole like E field distribution, but the E field enhancement γ is much smaller than that at λ_p.

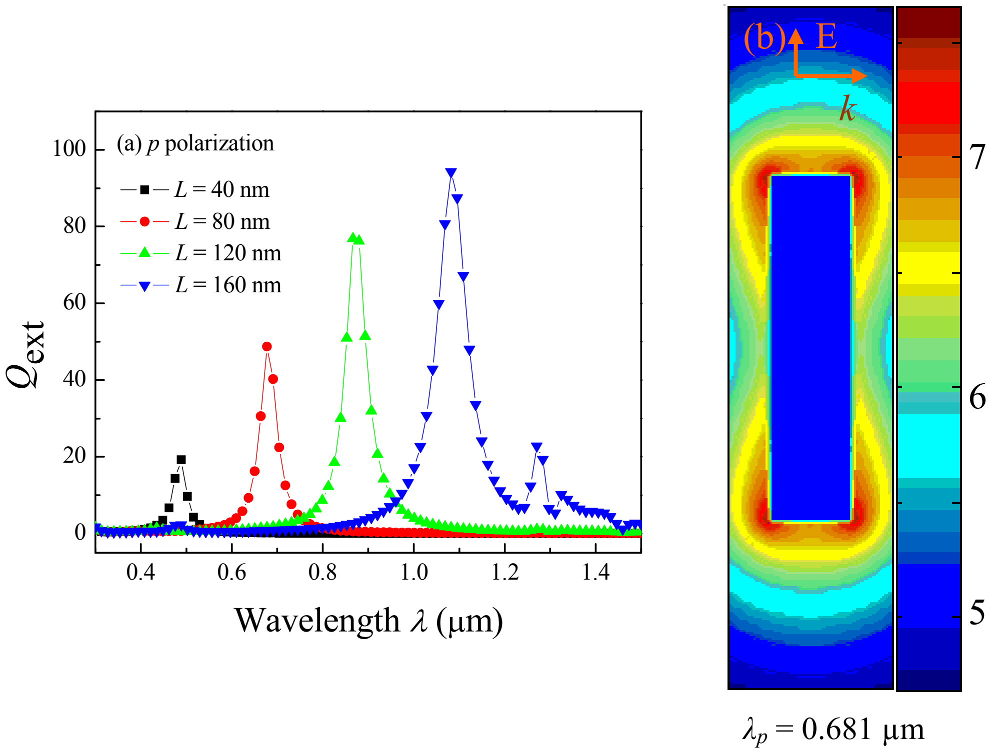

Figure 3.2 Cylindrical nanorods at p-polarization incidence (a) Extinction efficiency, and (b) E field enhancement contours ($\log_{10}\gamma$) of L = 80 nm cylindrical nanorod at λ_p = 0.681 μm.

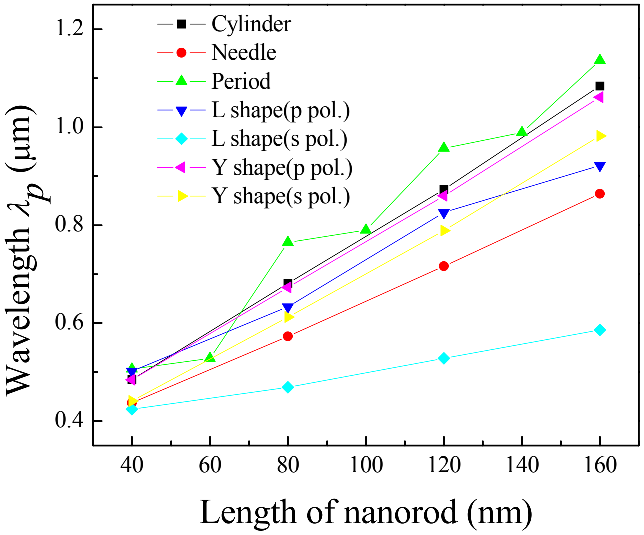

Figure 3.3 Plasmon peak wavelengths as a function of length for different shaped nanorods.

For *s*-polarized light, the extinction spectra have two extinction peaks regardless the length of the nanorods., The peak located at a longer wavelength (λ_{TDM} and λ_{TQM})[99]. The maximum *E* field enhancement at the TM mode is significantly smaller than that at the LM mode (at least two orders of magnitude less). At TDM incidence, the maximum *E* field enhancement occurs around the cylinder. At TQM incidence, the maximum enhancement occurs not at the tips but at the side, the top, and the bottom. A quadrupole-like *E* field distribution is demonstrated. The Rayleigh-Gans-Debye approximation[118] works well for *s*-polarization incidence. When light is exciting the TM plasmon modes, the nanorod can be considered as a series of parallel dipoles. This principle can also be used to describe the TM plasmon modes of other nanostructures.

3.3 Needle-shaped nanorods

For the needle-shaped nanorod, the diameters of the two ends are fixed to be 20 and 40 nm, and the length L_N varies from 40 nm to 160 nm. As shown in Fig. 3.4, light propagates perpendicular to the long axis of the needle. The *p*-polarization is defined as the *E* field along the long axis. The *s*-polarization is defined as the *E* field perpendicular to the long axis.

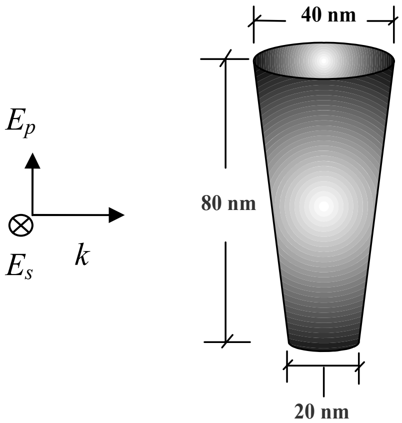

Figure 3.4 Schematics for needle-shaped nanorod and the definition of the incident polarizations in the DDA calculation.

For the needle-shaped nanorods, all the *p*-polarization spectra have a strong extinction peak at $\lambda_p > 0.4$ μm as shown in Fig. 3.5(a), which corresponds to LM plasmon resonance. Compared with the spectra of cylindrical nanorods, no additional plasmon peak appears at the right shoulder of the main plasmon peak even for $L_N = 160$ nm. With the increase of L_N, the LM plasmon peak red shifts linearly from $\lambda_p = 0.437$ μm for $L_N = 40$ nm to $\lambda_p = 0.864$ μm for $L_N = 160$ nm. The amplitude of the peak also increases, but is still smaller than that of a cylindrical nanorod with the same length. Compared to a cylindrical nanorod with the same length, the plasmon peaks of needle-shaped nanorod are blue shifted. This is because the effective diameter of needle-shaped nanorod is larger than that of cylindrical nanorod. Among nanorods with the same length, the plasmon peak blue shifts with increasing diameter. With the increase of the nanorod length, the plasmon peaks of needle-shaped nanorods do not red shift as dramatically as that of cylindrical nanorods, as shown in Fig. 3.3. Compared to cylindrical nanorods, all the main plasmon peaks for needle-shaped nanorods become broader. For example, the full width-at-half-maximum (FWHM) of L = 160 nm cylindrical nanorod is 78 nm and the FWHM of L_N = 160 nm needle-shaped nanorod is 89 nm. The broader plasmon peak is due to the tilted side surface which increases the number of oscillation modes of plasmon resonance.

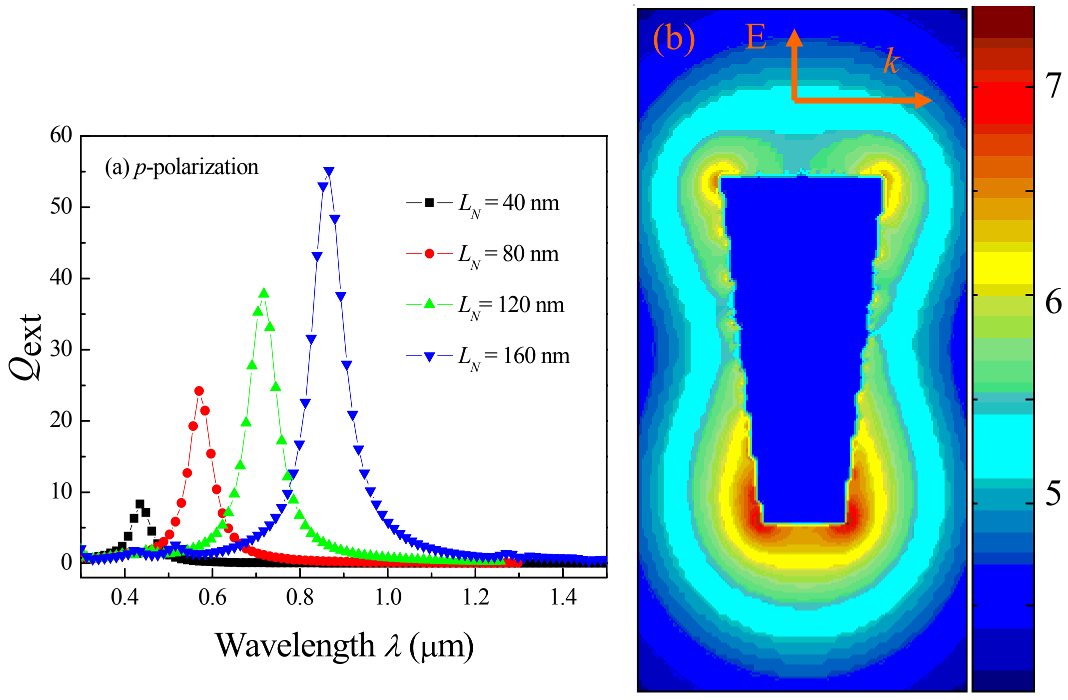

λ_p = 0.573 µm

Figure 3.5 Needle-shaped nanorods at p-polarization incidence (a) Extinction efficiency, and (b) E field enhancement contours ($\log_{10} \gamma$) of L_N = 80 nm needle-shaped nanorod at λ_p = 0.573 µm.

Figure 3.5(b) illustrates the E field enhancement distribution γ of a needle-shaped nanorod of L_N = 80 nm at λ_p = 0.573 µm. The E field congregates to the sharp tip of the needle, as compared to the maximum field distribution on the two ends of a cylindrical rod. Other needle-shaped nanorods at λ_p incidence have similar E field distribution.

There are also two TM resonance modes for s-polarized incidence, and the spectra almost do not change with $L_{N.}$. At TDM incidence, the maximum enhancement is distributed at the two ends of the needle and a dipole-like E field distribution is also demonstrated. At TQM incidence, the maximum E field occurs at the side, the top, and the bottom and has a quadrupole-like E field distribution. The scattering E field distribution can also be treated as the result from a series of parallel dipoles.

To better understand the polarization dependent extinction spectra, angular dependent polarized spectra were calculated every 10° from the direction of p-polarization. The nanorod length is fixed at 160 nm for needle-shaped nanorods.

Figure 3.6(a) plots the angular dependent spectra of the needle-shaped nanorod, where β denotes the polarization angle with respect to p-polarization direction. With the increase of β from 0° to 90°, the Q_{ext} at λ_p = 0.864 µm decreases and the Q_{ext} at λ_{TQM} = 0.342 µm and λ_{TDM} = 0.382 µm increases. Figure 3.6(b) shows the polar plot of the extinction efficiency with three incident wavelengths, λ_{TQM} = 0.342 µm, λ_{TDM} = 0.382 µm and λ_p = 0.864 µm, respectively. The polar plot of TM modes has a 90° phase shift with respect to the plot at LM mode. The best equation to fit the data is given by

$$Q_{ext} = A + B\sin^2\beta\,. \tag{3.1}$$

The solid curves in Fig. 3.6(b) result from the fitting of Eq. 3.1. The goodness of fit, *R*, is better than 0.998. The *E* field enhancement distribution of L_N = 160 nm nanorod irradiated by the light with different polarization angle β are also calculated.

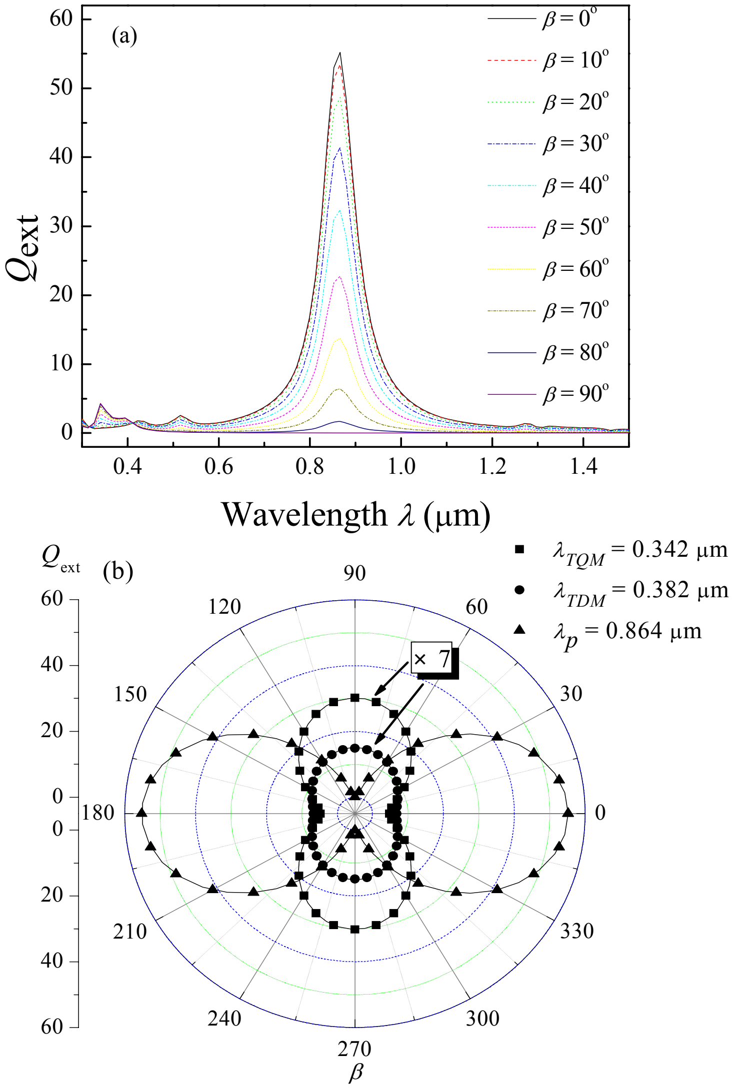

Figure 3.6 Extinction efficiency for needle-shaped nanorod of L_N = 160 nm (a) polarization dependent spectra and (b) polar plot at λ_{TQM} = 0.342 μm, λ_{TDM} = 0.382 μm, and λ_p = 0.864 μm. For better view, the Q_{ext} at λ_{TQM} = 0.342 μm and λ_{TDM} = 0.382 μm time 7.

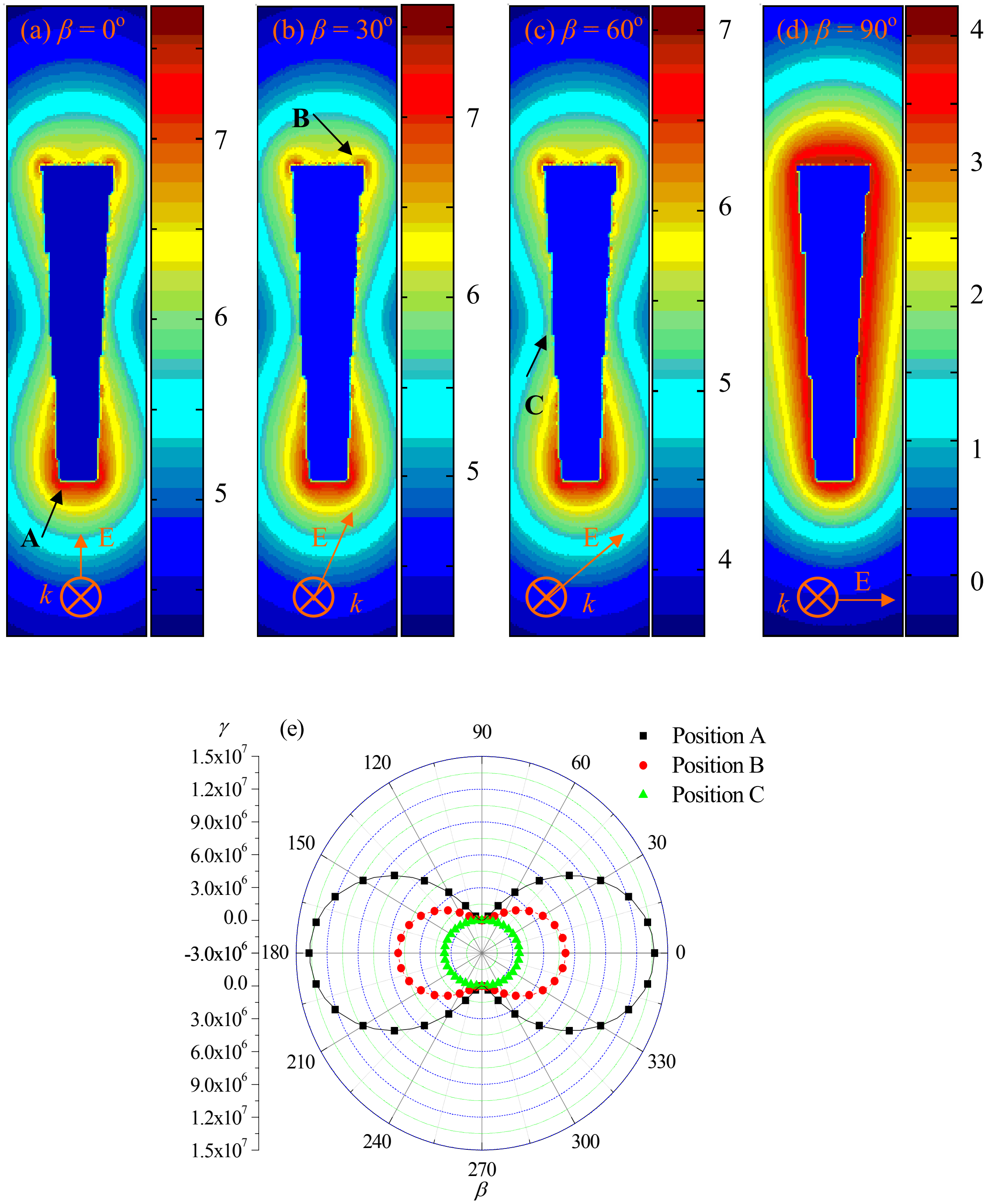

Figure 3.7 *E* field enhancement contours of L_N = 160 nm needle-shaped nanorod at λ_p = 0.864 μm with different polarization angle β (a) β = 0°, (b) β = 30°, (c) β = 60°, and (d) β = 90°, respectively. (e) Polarization dependent field enhancement γ for several locations around the nanorod surface (Solid curves calculated by fitting Eq. 3.1).

Figure 3.7 illustrates the E field enhancement distribution at β = 0°, 30°, 60° and 90°, respectively at λ_p = 0.864 μm, along with the fit according to Eq. 3.1. With the increasing polarization angle, the magnitude of the maximum E field enhancement decreases. When the polarization angle varies from 0° to 80°, the maximum E field occurs around the needle tip. When the polarization angle reaches 90°, the maximum E field occurs around the outer surface of the needle. In order to investigate how the E field around the surface changes with the incident polarization, the E field enhancement at several particular locations as a function of incident polarization angle are plotted in Fig. 3.7(e). Position A and B are close the bottom and top corner of the needle as shown in Fig. 3.7(a) and (b). Position C is close to the middle of the side surface as shown in Fig. 3.7(c). The solid curves are also the fitting plots using Eq. 3.1. For all three locations, the maximum E field enhancement occurs at p polarization, and the minimum enhancement at s polarization. Regardless of the polarization angle, the needle top (Position A) always has the maximum E field. The shape of the polar plot also depends on the incident wavelength. If the incident wavelength changes to the TM modes, the maximum E field enhancement occurs when β = 90°, and the minimum E field enhancement occurs at β = 0°.

3.4 Periodically shaped nanorods

For the period-shaped nanorods, each disk-like section of the nanorod has a fixed height of 20 nm, but the diameter of the disk varies periodically along the height, alternating between 20 nm and 40 nm. The period-shaped nanorods are divided into two groups, integer-period nanorods and half-period nanorods. For integer-period nanorods, the structure contains equal numbers of large and small disks. For example, the period-shaped nanorod of L_P = 40 nm (Period = 1) contains two disks with a height of 20 nm; the bottom disk has a diameter of 40 nm and the upper disk has a diameter of 20 nm. For half-period nanorods, the structure contains unequal numbers of large and small disks. For example, the L_P = 140 nm period-shaped nanorod has four small disks of diameter 20 nm and three large disks of diameter 40 nm. For DDA calculation, the total length L_P of the periodic nanorod increases from 40 nm to 160 nm. The *p* polarization is defined as the *E* field parallel to the long axis of the structure; the *s* polarization is defined as the *E* field perpendicular to the long axis, as shown in Fig. 3.8.

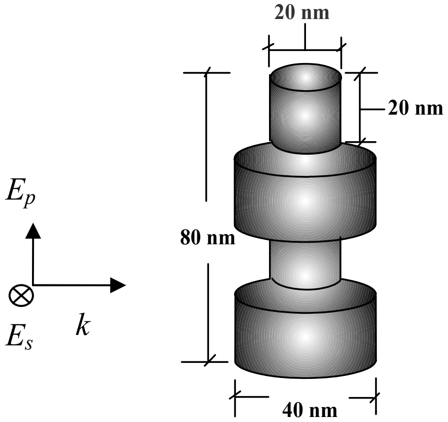

Figure 3.8 Schematics for period-shaped nanorod and the definition of the incident polarizations in the DDA calculation.

The period-shaped nanorods are divided into two groups: integer-period nanorods (L_N = 40, 80, 120, and 160 nm) and half-period nanorods (L_N = 60, 100, and 140 nm). Integer-period nanorods show several extinction peaks in the *p* polarization spectra, as plotted in Fig. 3.9(a). For L_P = 40 nm nanorods, there are two plasmon peaks at λ = 0.377 µm and λ_p = 0.506 µm. For L_P = 80 nm nanorod, other than the main plasmon peak that appears at λ_p = 0.765 µm, there are two additional plasmon peaks appearing at λ = 0.383 µm and 0.503 µm, similar to L_P = 40 nm nanorod. When L_P increases from 80 nm to 160 nm, the spectra always have three extinction peaks, two located at ~ 0.377 µm and ~ 0.506 µm, the other several extinction peaks changing from 0.765 μm to 1.136 μm. The plasmon peaks located around 0.38 and 0.5 μm only slightly shift, as shown in Fig. 3.9(b). The *E* field enhancement distribution γ gives a good explanation of the induced charge oscillation mode for each extinction peak.

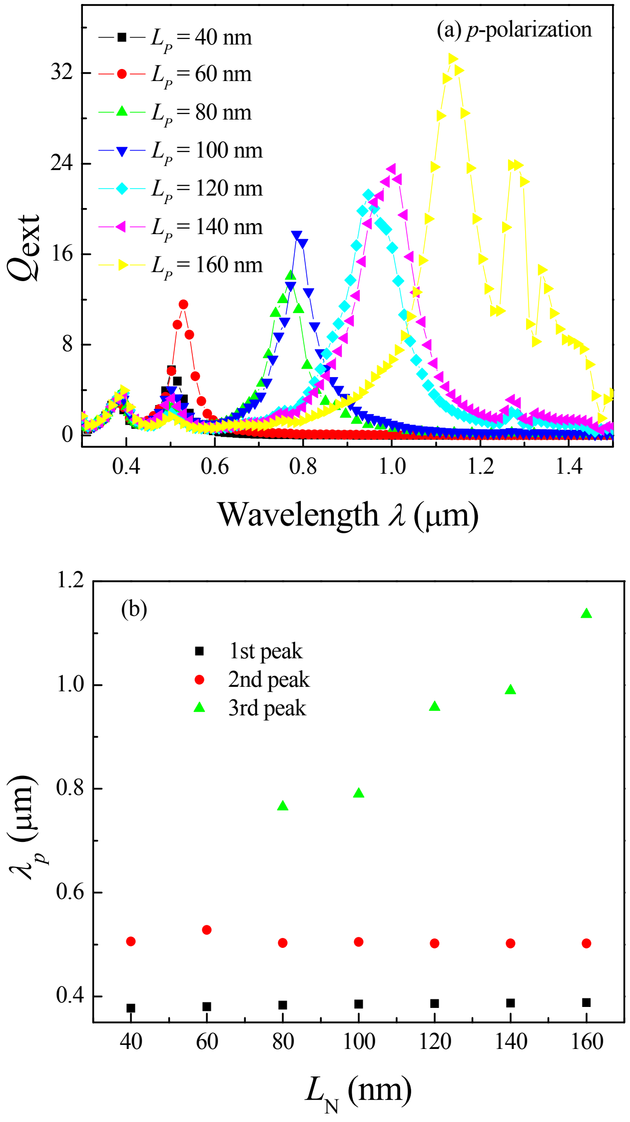

Figure 3.9 Extinction efficiency for period-shaped nanorods with different lengths at different incident polarization: (a) *p*-polarization, (b) plot of the wavelengths of different extinction peaks versus nanorod length L_P under *p*-polarized incidence.

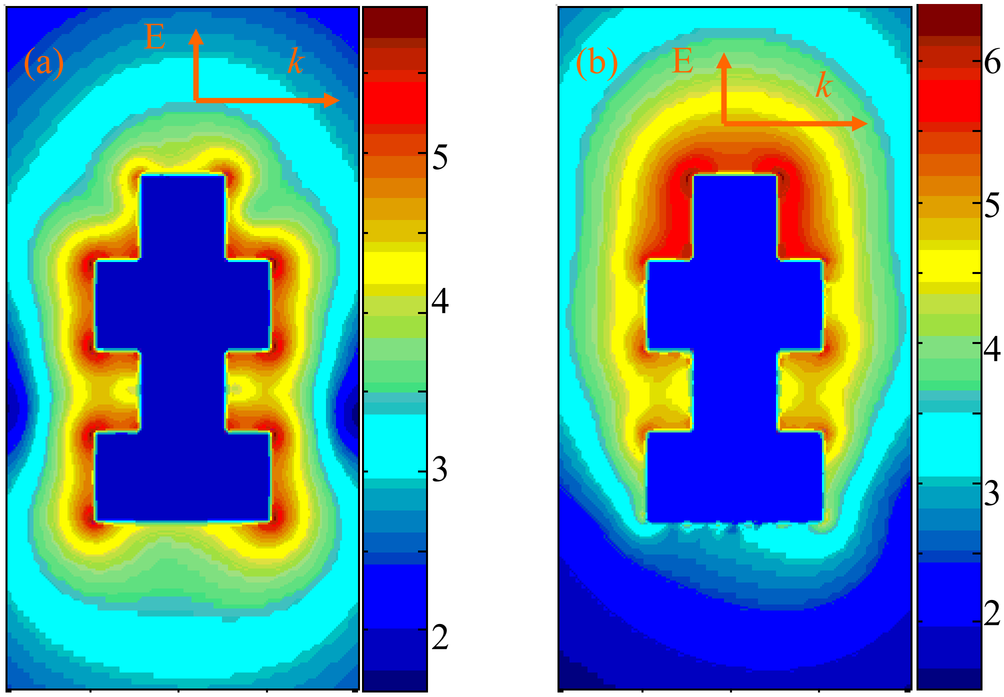

$\lambda = 0.383$ μm $\lambda = 0.503$ μm

Figure 3.10 *E* field enhancement contours ($\log_{10} \gamma$) of $L_P = 80$ nm period-shaped nanorod with *p*-polarized incidence at different wavelengths: (a) $\lambda = 0.383$ μm, (b) $\lambda = 0.503$ μm

Figure 3.10(a) illustrates the *E* field enhancement distribution γ of $L_P = 80$ nm nanorod at $\lambda = 0.383$ μm. The maximum *E* field is located around the corners of the large disks. For other period-shaped nanorods at the plasmon peaks around 0.38 μm, there are similar *E* field distributions. In addition, when an individual large disk (40 nm diameter and 20 nm length) is irradiated by the light with polarization along the axis of the disk, the plasmon peak is located at $\lambda_p = 0.374$ μm and the maximum *E* field enhancement occurs around the corners of the disk. These results demonstrate that the plasmon peaks around 0.38 μm for all the periodic nanorods are mainly due to the induce charge oscillations in the large disks, i.e. the oscillation in the protruded sections. Figure 3.10(b) illustrates the *E* field enhancement distribution of the $L_P = 80$ nm nanorod at $\lambda = 0.503$ μm. The maximum *E* field enhancement only distributes on the top small disk (20 nm diameter and 20 nm length). Other period-shaped nanorods at the plasmon peaks around 0.5 μm also have similar *E* field distributions on the top section. For an individual small disk (20 nm diameter and 20 nm length) with polarization along the disk axis, the plasmon peak is located at λ = 0.401 μm and the maximum *E* field enhancement occurs around the side surface. When another larger disk is added at the bottom, i.e., the L_N = 40 nm nanorod, the plasmon peak red shifts to λ_p = 0.506 μm and the maximum *E* field distributes around the top small disk, which is similar to the field distribution on the top 40-20 structure for L_P = 80 nm. Thus, we can conclude that the plasmon peak around 0.5 μm is mainly due to the induced charge oscillation in the top 40-20 disks. For L_P = 80 nm, at the main plasmon peak incidence (λ_p = 0.765 μm), the maximum *E* field occurs around the corners of top small disk and the bottom large disk. The main plasmon peak is due to the induced charge oscillation in the entire structure from the bottom to the top. Period-shaped nanorods of L_P = 120 and 160 nm at λ_p have a similar *E* field distribution, and λ_p increases monotonically with L_P. Compared to the cylindrical nanorods with the same length, the integer-period nanorods have a smaller *E* field enhancement, but more maximum field sites along the rod and a larger λ_p. This result infers that roughness along the Ag nanorods could alter the LSPR and the field distribution, and generates more hot spots for SERS. This is a benefit if the structured is used for chemical/biological sensors.

For half-period nanorods, the *p* polarization spectra also show two to three extinction peaks. For L_P = 60 nm nanorods, there are two plasmon peak located at λ = 0.38 μm and λ_p =0.528 μm. For L_P = 100 nm nanorods, besides the main plasmon peak at λ_p = 0.79 μm, there are two plasmon peaks located at λ = 0.385, and 0.505 μm. With the increase of the length from L_P =60 nm to 140 nm, main plasmon peaks λ_p red shift from λ_p = 0.528 μm to λ_p = 0.989 μm. The plasmon peaks located around 0.38 and 0.5 μm are also slightly shifted as shown in Fig. 3.9(b).

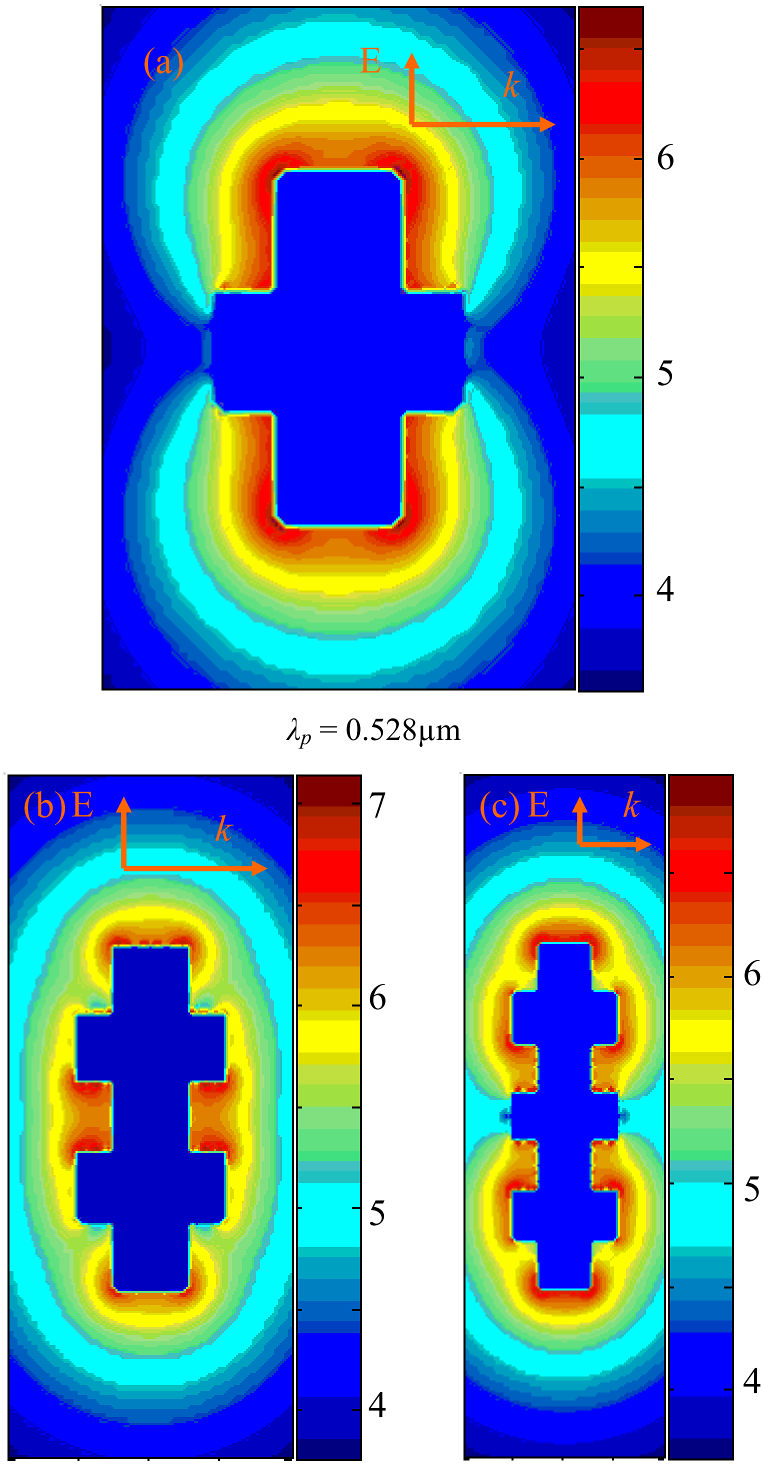

$\lambda_p = 0.528\mu m$

$\lambda_p = 0.79\mu m$

$\lambda_p = 0.989\mu m$

Figure 3.11 *E* field enhancement contours ($\log_{10}\gamma$) for period-shaped nanorod with different lengths with *p*-polarized incidence: (a) L_P = 60 nm at λ_p = 0.528 μm, (b) L_P = 100 nm at λ_p = 0.79 μm and (c) L_P = 140 nm at λ_p = 0.989 μm.

Half-period nanorods irradiated at plasmon peaks of around 0.38 and 0.5 μm also have similar *E*-field distributions as integer-period nanorods. The maximum *E* field enhancement distribution γ occurs at the corner of large disks, and around small disks at two ends, respectively, thus they have similar origins. For L_P = 60 nm nanorod at λ_p = 0.528 μm, the maximum *E* field enhancement occurs around two small disks (Fig. 3.11(a)). Figures 3.11(b) and 3.11(c) illustrate the *E*-field enhancement distribution γ of L_P = 100 and 140 nm nanorod at λ_p = 0.79 and 0.989 μm, respectively. The maximum *E* field enhancement occurs around the corners of two small disks at two ends. There is a symmetric *E* field distribution in the vertical direction. Compared to the cylindrical nanorods with the same length, the half-period nanorods also have smaller *E* field enhancement.

Integer-period nanorods break the symmetry in the vertical direction and the plasmon peak is red shifted when compared to cylindrical nanorods of the same length. When another small disk is added to the bottom of the integer-period nanorods, the structures become symmetric at vertical direction and show plasmon peaks similar to those of cylindrical nanorods with the same length, as shown in Fig. 3.3. All period-shaped nanorods have a smaller extinction efficiency compared to same length cylindrical nanorods. At resonant wavelength λ_p, period-shaped nanorods provide more hot spots due to near field plasmon coupling and increased geometrical singularities. Therefore, period-shaped nanorods may have more ability to capture and detect small amount of molecules through the SERS technique.

For *s*-polarized incidence, the position and magnitude of TDM change very little while the intensity of TQM slightly increases. The maximum *E* field at TDM incidence (λ_{TDM} = 0.402 μm) is distributed not only at the corners but also at the top and the bottom of the whole period structure. At TQM incidence (λ_{TQM} = 0.351μm), the maximum *E* field is distributed at the side of small disks and the top of the period structure. There are also significant *E* fields at the sides of large disks and the bottom of the period structure, but there is no larger enhancement around the corners. The field enhancements are significantly smaller than those at LM modes.

For the period-shaped nanorod, the angular dependent extinctions spectra have similar trend as shown in Eq. 3.1 and similar *E* field distribution to needle-shaped nanorod: the maximum *E* field enhancement occurs when $\beta = 90^o$, and the minimum *E* field enhancement occurs at $\beta = 0^o$.

3.5 L-shaped nanorods

For the L-shaped nanorods, the arms each have a diameter of 20 nm and the angle between two arms is fixed at 100°. The length of each arm varies from 20 nm to 80 nm, so that the total length L_L (the sum of the two arms) increases from 40 nm to 160 nm. The incident polarization is defined as shown in Fig. 3.12.

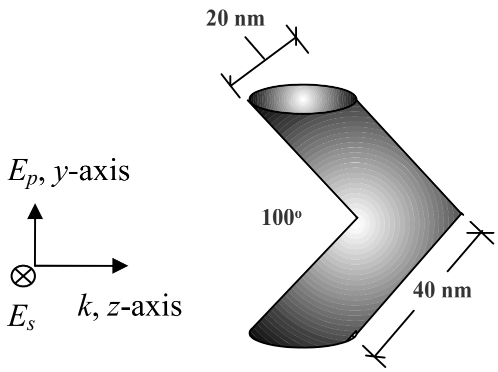

Figure 3.12 Schematics for L-shaped nanorod and the definition of the incident polarizations in the DDA calculation.

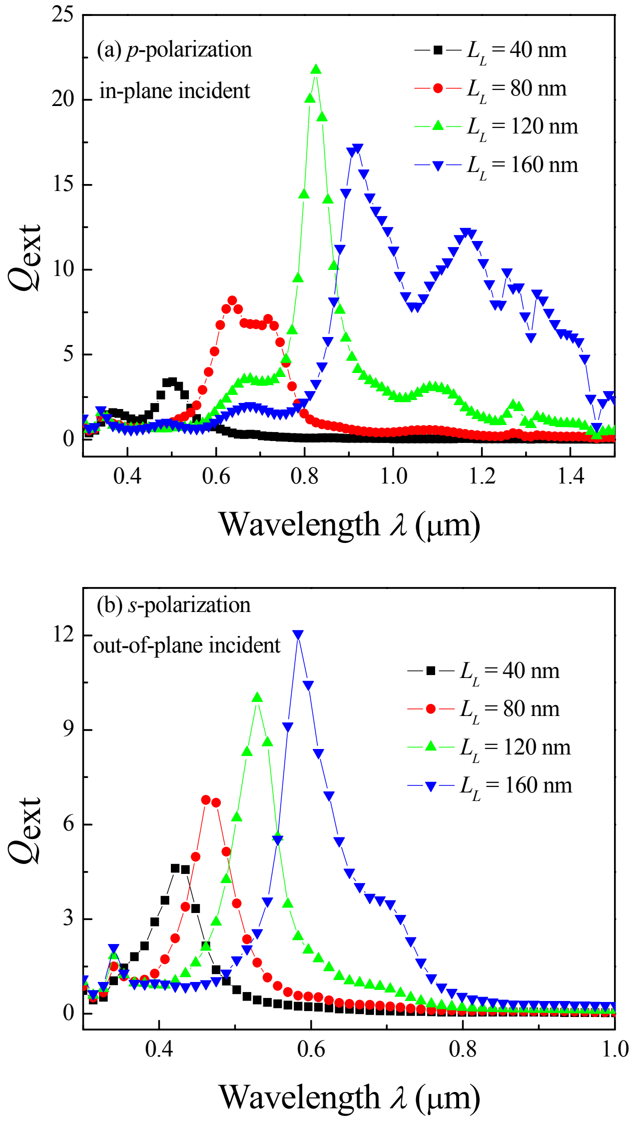

Figure 3.13 Extinction efficiency of L-shaped nanorods with different lengths at different incident polarizations: (a) *p*-polarization and (b) *s*-polarization.

For L-shaped nanorod with *p*-polarization and in-plane incidence, more complicated multiple peaks appear as shown in Fig. 3.13(a). For L_L = 40 nm nanorod, there are two plasmon peaks, located at λ = 0.376 μm and λ_p = 0.502 μm. The peak at λ_p = 0.502 μm has the higher extinction. For L_L = 80 nm nanorod, there are also two main plasmon peaks, located at λ_p = 0.633

μm and λ = 0.725μm. The peak at λ_p = 0.633 μm has the higher extinction The L_L = 120 and 160 nm nanorods have similar extinction spectra. Besides the main plasmon peaks located at λ_p = 0.826 μm and λ_p = 0.922 μm, all the main peaks have shoulders. The left shoulder of the main plasmon peaks is located at λ = 0.678 μm and the right shoulder has two peaks, λ = 1.091 μm and λ = 1.164 μm. When the length increases to L_L = 120 nm, the extinction at the main plasmon peak increases and is at the maximum, but is still small compared to that of a cylindrical nanorod with the same length. As shown in Fig. 3.3, the plasmon peaks of L-shaped nanorods also do not linearly red shift with length. When the length increases to 80 nm, the main plasmon peak of L-shaped nanorods are slightly blue shifted compared to cylindrical nanorods of the same length.

Figure 3.14(a) and (b) illustrate the *E* field enhancement distribution of L_L = 80 nm nanorod at λ_p = 0.633 and λ = 0.725 μm, respectively. The maximum *E* field congregates at the inside of the elbow and around the tips, creating a dipole like *E* field distribution. When a tilted 40nm-length cylinder (one section of the L-shape) is irradiated with *p*-polarization (*y*-axis direction), the plasmon peak appears at λ = 0.513 μm and the maximum *E* field enhancement γ appears around the sharp angle. When two tilted cylinders are connected together to form one L shape, the main plasmon peak is red shifted 0.119 μm and the maximum *E* field around the interface disappears. When each L-shaped nanorod is irradiated, at the main plasmon peak wavelength λ_p, all the L-shaped nanorods have the similar *E* field distribution. Comparing to the cylindrical nanorod with the same length, the *E* field enhancements of L-shaped nanorods are much smaller. When irradiated with *s* polarized light (not shown), one broad plasmon peak appears for L_L = 40 nm nanorod. This is due to the maximum γ being distributed around the outer surface of the entire L-shaped nanorod. As the length increases, this broad peak changes to an asymmetric peak, the center of which represents the TQM mode, and the shoulder represents

TDM plasmon mode at the right side. When the length is increased further, the extinction of the TQM plasmon mode increases.

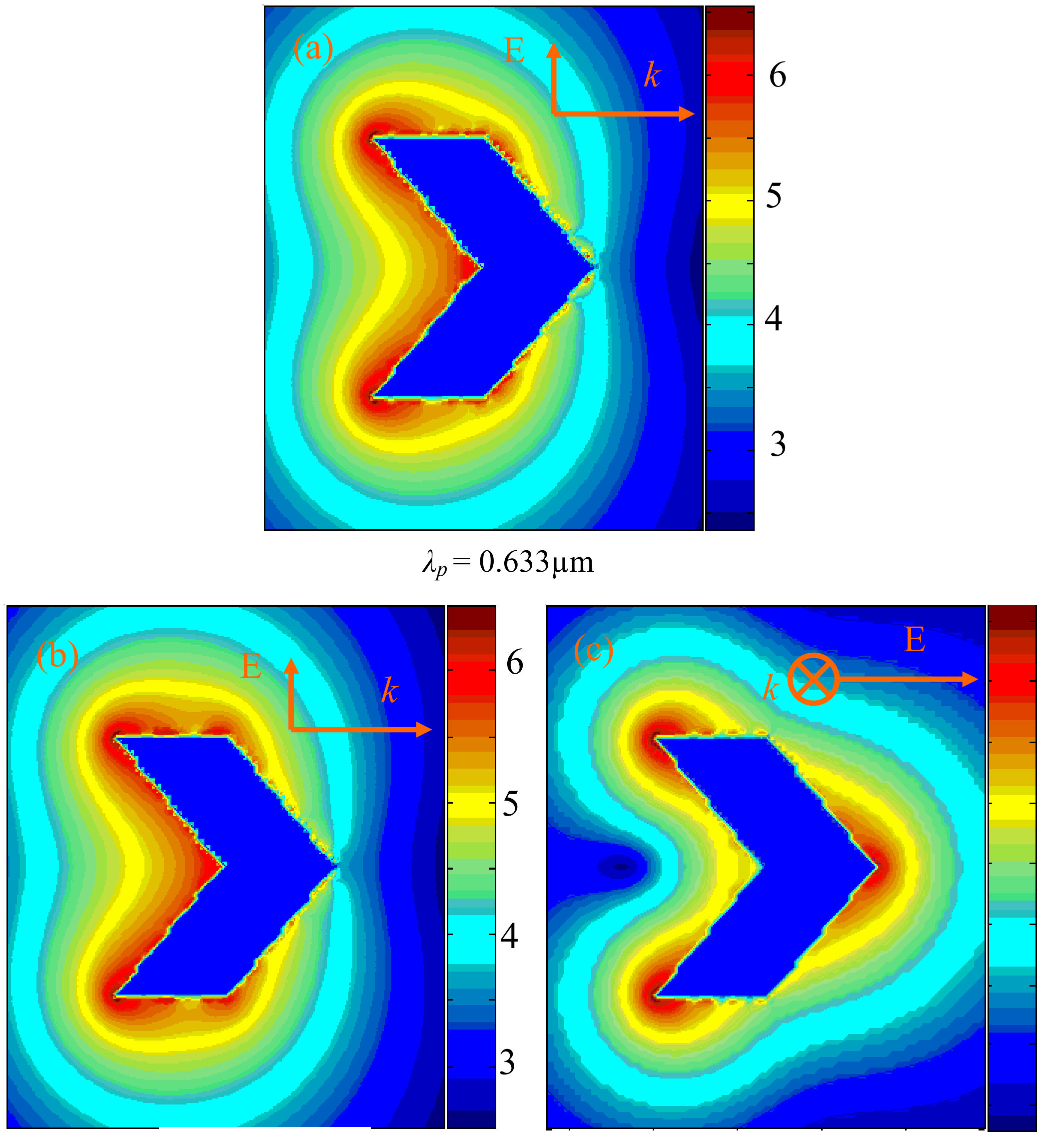

$\lambda_p = 0.633\mu\text{m}$

$\lambda = 0.725\mu\text{m}$

$\lambda_p = 0.469\mu\text{m}$

Figure 3.14 *E* field enhancement contours ($\log_{10}\gamma$) of L_L = 80 nm L-shaped nanorod with *p*-polarized incidence at: (a) λ_p = 0.633 μm and (b) λ = 0.725 μm; and *s*-polarized incidence at: (c) λ_p = 0.469 μm.

Because L shape breaks cylindrical symmetry, the change of incident direction may also affect the extinction spectra. The extinction spectra of out-of-plane incidence (incident direction *k* along the *x*-axis as shown in Fig. 3.12) are also calculated. The *p*-polarization is defined as the *E* field along *y*-axis direction, and the *s*-polarization is along *z*-axis direction. For *p*-polarization, the extinction spectra are the same as those of in-plane incidence, as in Fig. 3.13(a). For *s* polarization, the spectra change significantly as shown in Fig. 3.13(b). At L_L = 40 nm, there is a broad peak located at λ_p = 0.424 μm and a shoulder at λ = 0.366 μm. For L_L = 80 nm nanorod, the broad band is red shifted to λ_p = 0.469 μm, and another plasmon peak appears at λ = 0.34 μm which does not change position when the length increases further. The main plasmon peak red shifts linearly with the increase of length from λ_p = 0.424 μm at L_L = 40 nm to λ_p = 0.586 μm at L_L = 160 nm as shown in Fig. 3.3. The plasmon peak of L-shaped nanorods are blue shifted compared with a cylindrical nanorod with the same length. With the increase of the nanorod length, the plasmon peaks of L-shaped nanorods do not red shift as dramatically as those of cylindrical nanorods. Compared to the in-plane *p*-polarized incidence, the main plasmon peaks of out-of-plane *s*-polarized incidence are blue shifted. Figure 3.14(c) illustrates the *E* field enhancement distribution of L_L = 80 nm nanorod at λ_p = 0.469 μm. The maximum *E* field congregates around the tips and the outside of the elbow. At the main plasmon peak wavelength, other L-shaped nanorods have a similar *E* field distribution. The fields are much lower than those for the cylindrical nanorods with the same length but with more hot spots. For L_L = 40 and 80 nm nanorods, out-of-plane *s*-polarization and in-plane *p*-polarization have similar *E* field enhancement, but when the length increases to L_L = 120 and 160 nm, *E* field enhancements of in-plane *p*-polarization are much higher than those of out-of-plane *s*-polarization.

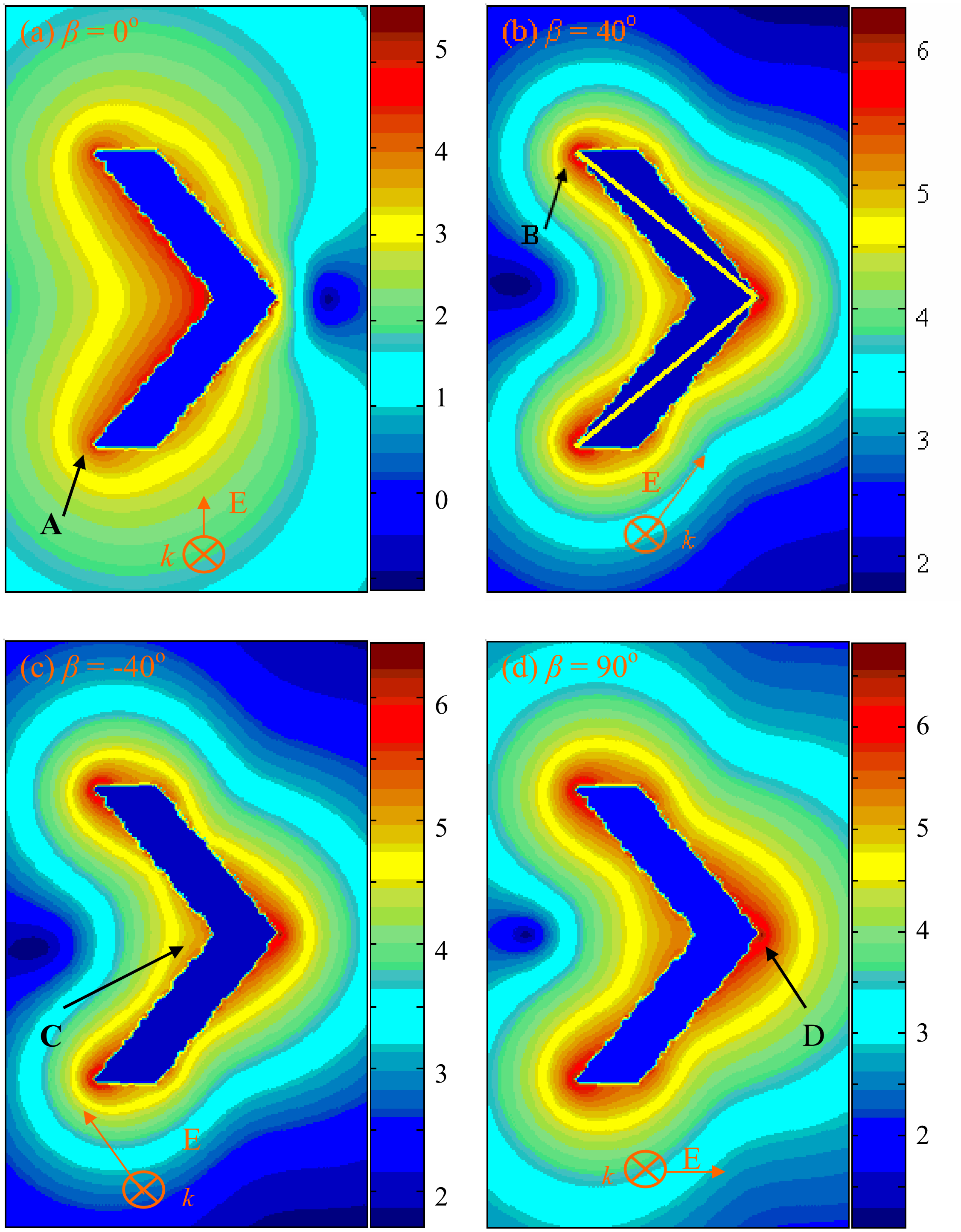
(a) β = 0°
5
4
3
2
1
0
A
E
k
(b) β = 40°
6
5
4
3
2
B
E
k
(c) β = -40°
6
5
4
3
2
C
E
k
(d) β = 90°
6
5
4
3
2
D
k
E

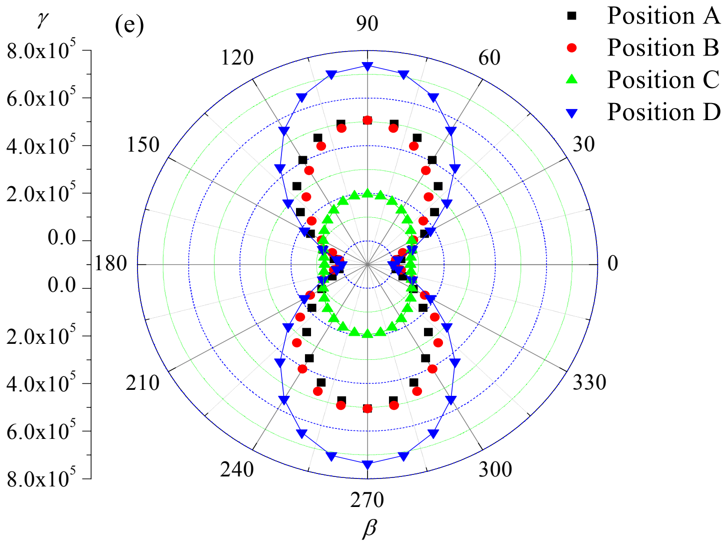

Figure 3.15 *E* field enhancement contours of L_L = 160 nm L-shaped nanorod at λ_p = 0.586 μm with different polarization angle β (a) $\beta = 0^{\circ}$, (b) $\beta = 40^{\circ}$, (c) $\beta = -40^{\circ}$, and (d) $\beta = 90^{\circ}$, respectively. (e) Polarization dependent field enhancement γ for several locations around the nanorod surface (Solid curves calculated by fitting Eq. 3.1).

For L-shaped nanorods, the plasmon peak can be tuned not only by the structural parameters but also by the polarization and the incident direction of the light. In addition, the polarization direction of the incident light can change the spatial distribution of the maximum *E* field, which may provide a simple way to spatially resolve analyte distribution on nanorods for detection.

Unlike the needle shape nanorod, the L-shaped nanorod does not have a cylindrical symmetry. Rather, it has a reflective symmetry. One could expect as a result a different polarization dependent *E* field distribution. Figure 3.15 (a-d) illustrates the *E* field enhancement distribution with different polarization angles β = 0°, 40°, -40° and 90°, respectively. Incident light was in the *x*-axis direction (out-of-plane) with λ_p = 0.586 μm, which is the main plasmon peak at *s* polarization incidence. For *p* polarization incidence (β = 0°), the maximum *E* field congregates into the intersection and around the tips. The maximum *E* field enhancement increased with the increase of the polarization angle, and the maximum *E* field congregated around the tips and the outside of the elbow. The polar plots of the enhancement at several particular locations are given in Fig. 3.15(e). Positions A and B are located around the bottom and top corners, position C is located inside of the elbow, and position D around the acute tip. With the increase of the polarization angle, the enhancement at these positions increases. The polar plots for position C and D can be fitted by Eq. 3.1. When the polarization angle β increases from 0° to 90°, position A has higher enhancement than position B. At $\beta \approx 45^o$ and 135°, the difference of the enhancement between position A and B is at maximum. This is caused by the electron oscillation along the maximum distance in one arm, as illustrated by the lines in Fig. 3.15(b), i.e. from position A to position D and from position B to position D.

3.6 Y-shaped nanorods

For the Y-shaped nanorods, the arms also each have a diameter of 20 nm, and the angle between two top arms is fixed at 50°. The length of the two top arms and the bottom cylinder varies from 20 to 80 nm, so that the total length L_Y (the sum of the bottom arm and one of the top arms) also varies from 40 nm to 160 nm. The incident polarizations are illustrated in Fig. 3.16.

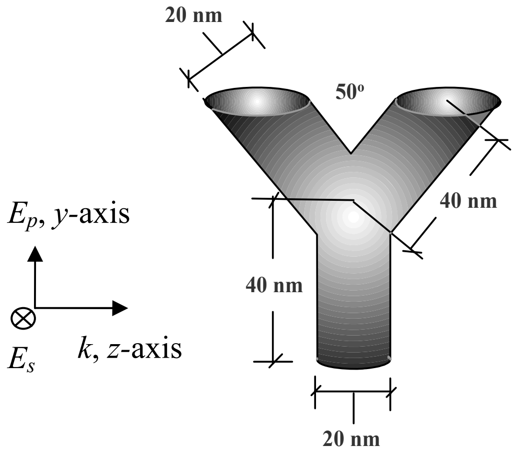

Figure 3.16 Schematics for L-shaped nanorod and the definition of the incident polarizations in the DDA calculation.

For Y-shaped nanorods with *p*-polarized incidence, there is only one main plasmon peak dominating the extinction spectra for different lengths as shown in Fig. 3.17(a). Note that at the right side of main plasmon peak for L_{Y} = 160 nm, one small peak appears at $\lambda = 1.274$ µm and at the left side of main plasmon peak, two small peaks appear at $\lambda = 0.475$ and 0.562 µm. At L_Y = 40 nm, a Y-shaped nanorod almost has a similar resonance wavelength as a cylindrical nanorod with the same length. For other Y-shaped nanorods, the plasmon peaks are blue shifted compared to the cylindrical nanorods with the same length. Figure 3.3 show that the plasmon peaks red shift linearly with the increase of L_Y, but at a slower rate than the cylindrical nanorods. For the nanorods with the same length, Y-shaped nanorods also have smaller extinction efficiency than cylindrical nanorods.

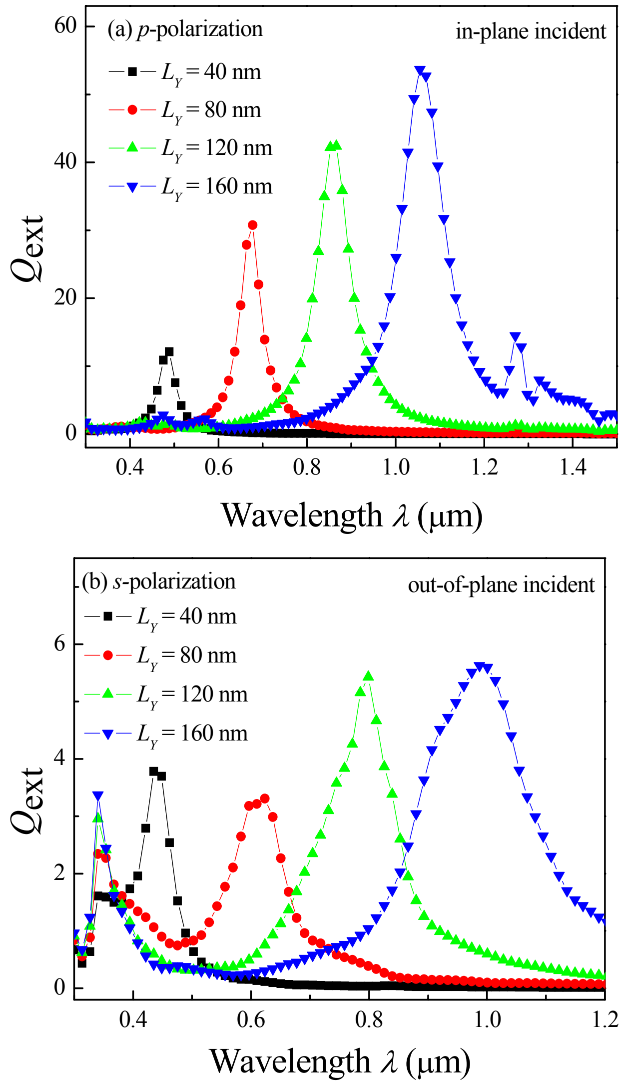

Figure 3.17 Extinction efficiency for Y-shaped nanorods with different lengths at different incident polarizations: (a) *p*-polarization, and (b) *s*-polarization.

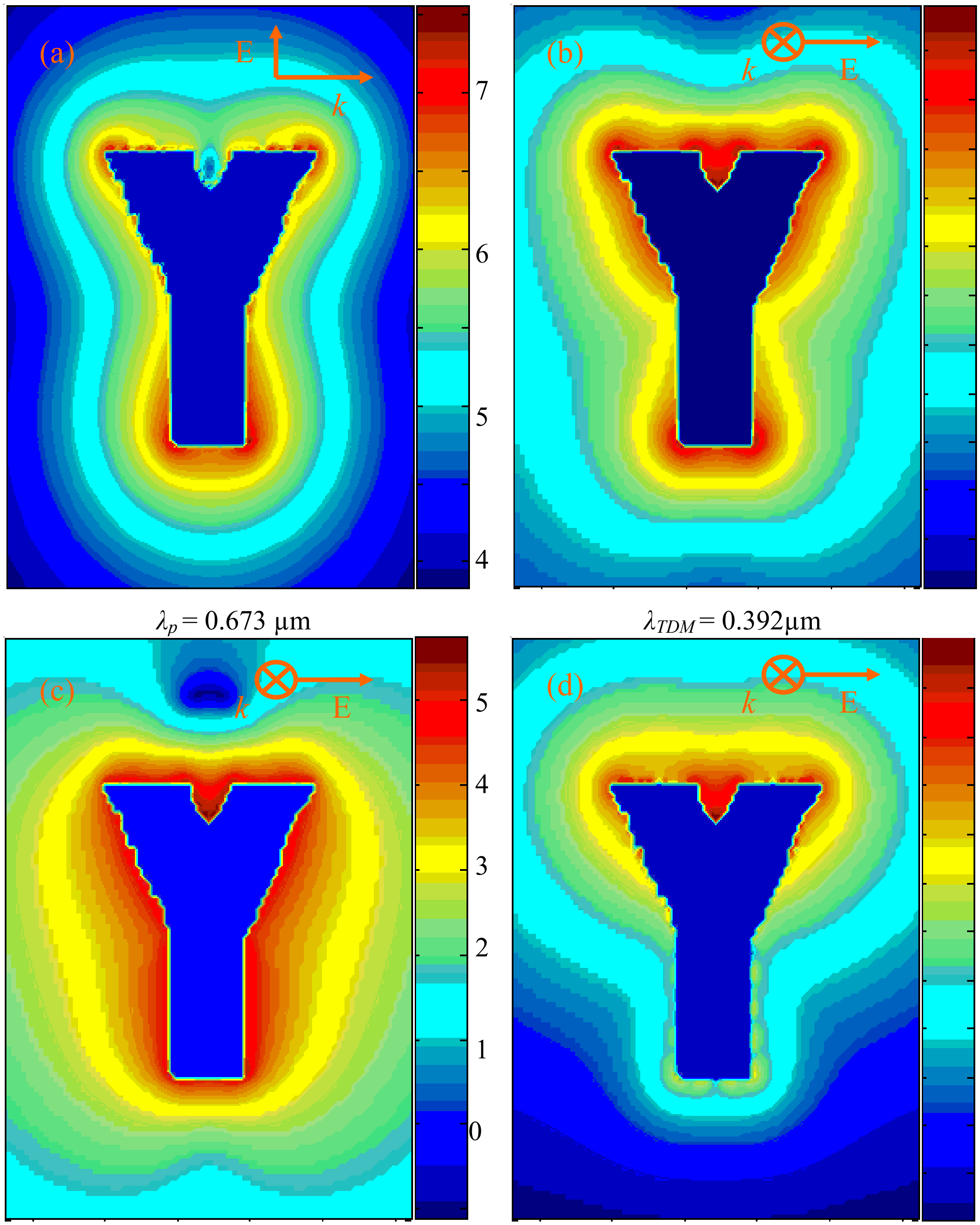

$\lambda_p = 0.673$ µm

$\lambda_{TDM} = 0.392$µm

$\lambda_{TQM} = 0.347$µm

$\lambda_p = 0.612$µm

Figure 3.18 *E* field enhancement contours ($\log_{10} \gamma$) of $L_Y = 80$ nm Y-shaped nanorod at different incident polarizations: (a) *p*-polarization at $\lambda_p = 0.673$ µm; and *s*-polarization with *x*-axis direction incidence at (b) $\lambda = 0.392$ µm, (c) $\lambda = 0.347$ µm and (d) $\lambda_p = 0.612$ µm

Figure 3.18(a) shows the E field enhancement distribution γ for $L_Y = 80$ nm nanorods at $\lambda_p = 0.673$ μm. The maximum E field occurs on the top of the two arms and around the bottom of the Y-shape structure. Because of the short arms of $L_Y = 40$ nm nanorod, this distribution looks similar to that for the needle-shaped nanorod and the E field enhancement occurs around the corners at $\lambda_p = 0.484$ μm. For other Y-shaped nanorods at λ_p, the maximum E fields also occur on the top of the two arms and around the bottom. When the length L_Y is equal to 40 and 160 nm, Y-shaped nanorods have a higher E field enhancement than cylindrical nanorods. Note that for the $L_Y = 160$ nm nanorod at $\lambda = 0.475$ and 0.562 μm, the maximum E fields not only occur on the top of two arms and around the bottom but also at the locations around ~1/3 and ~2/3 of the side surface of the Y-shaped nanorod, which shows the multiple mode E field distribution. With *s*-polarization incidence, the nanorod with $L_Y = 40$ nm has one broad plasmon peak. With the increase of length, this broad peak splits into two peaks, λ_{TDM} and λ_{TQM}. At λ_{TDM} and λ_{TQM}, the maximum E field enhancement occurs around outer surface of entire Y-shaped nanorods.

When the incident direction changes to out-of-plane, the extinction spectra and the E field distribution for *p*-polarized incident light do not change. The spectra for *s*-polarization incident light become more complicated, as shown in Fig. 3.17 (b). At $L_Y = 40$ nm, two extinction peaks appear at $\lambda = 0.365$ μm and $\lambda_p = 0.441$ μm, respectively. For other Y-shaped nanorods, except for the TDM and TQM located around $\lambda_{TDM} \approx 0.37$ μm and $\lambda_{TQM} \approx 0.345$ μm, the main plasmon peak dominating the spectra has a wavelength larger than 0.5 μm. With the increase of L_Y from 40 nm to 160 nm, the main plasmon peak red shifts linearly from $\lambda_p = 0.441$ μm to $\lambda_p = 0.982$ μm, as shown in Fig. 3.3. This change shows a similar slope as that of Y-shaped nanorods with in-plane *p* polarized incidence. However, for Y-shaped nanorods of the same length, the plasmon peaks of out-of-plane *s*-polarization are blue shifted compared to those of in-plane *p*-polarization. When

L_Y = 40 nm nanorod is irradiated at λ = 0.441 μm, the maximum E field occurs at the top. Figure 3.14(b-d) plots the E field distribution of L_Y = 80 nm Y-shaped nanorod for λ_{TDM} = 0.392 μm, λ_{TQM} = 0.347 μm, and λ = 0.612 μm, respectively. When the Y-shaped nanorods are irradiated at the TDM plasmon peak wavelength, the E-fields congregate at the top and the bottom. When the Y-shaped nanorods are irradiated at the TQM plasmon wavelength, the maximum E field enhancements occur around the outer surface. When irradiated at the wavelength of the main plasmon peak, the E field congregated into the top elbow and around the top arms. For other Y-shaped nanorods at main plasmon peak wavelengths, there are the similar E field distributions.

For Y-shaped nanorods, the plasmon peak can be tuned not only by changing the structure parameters but also by changing the incident polarization angle. For out-of-plane *s* polarized incidence, the maximum E field congregates into the top elbow structure where it is also easy to keep an analyte. Therefore, Y-shaped nanorods have the potential to be used as the substrate to obtain higher SRES signal.

Y-shaped nanorods also break cylindrical symmetry and would be expected to show a different polarization dependent E field distribution. Figure 3.19(a) shows the extinction spectra of L_Y = 160 nm Y-shaped nanorod with incidence in the *x*-axis direction (out-of-plane) at different polarization angles. With the increase of the polarization angle, the extinction of the main plasmon peak decreases in intensity and is blue shifted. The extinction of the multiple excitations at λ = 0.475 and 0.562 μm also decrease but the plasmon peaks do not shift with the increase of the polarization angle. Figure 3.19(b) plots the main plasmon peak as a function of the polarization angle. When the polarization angle increases from $\beta = 0^o$ to $\beta = 60^o$, the main plasmon peak is slightly blue shifted from λ_p = 1.061 μm to λ_p = 1.053 μm. When the polarization angle further increases to $\beta = 90^{o}$, the main plasmon peak dramatically blue shifts to$\lambda_p = 0.982$ µm.

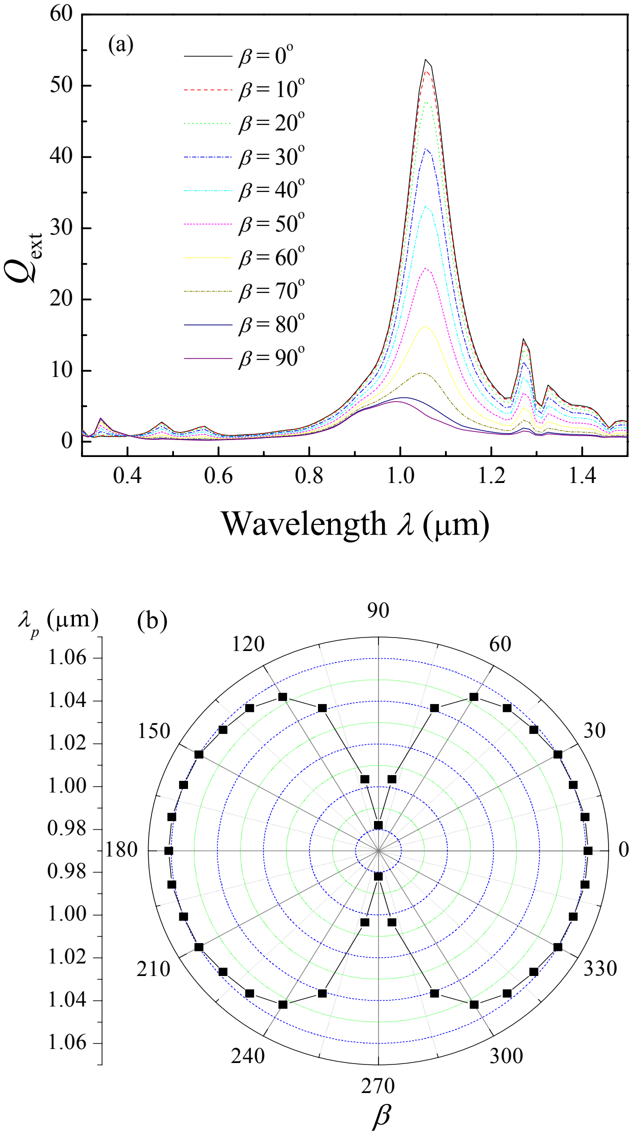

Figure 3.19 (a) Polarization dependent extinction spectra for Y-shaped nanorod of L_Y = 160 nm with x-axis direction incidence. (b) Plasmon peak wavelength as a function of incident polarization angle.

Figure 3.20 (a-d) illustrates the *E* field enhancement distribution with different polarization angles β = 0°, 30°, 60° and 90°, respectively, with light incidence in the *x*-axis direction at λ_p = 0.982 μm. For *p* polarized incidence (β = 0°), the *E* field distribution reveals the existence of large surface charges on the bottom of the nanorod. The *E* field enhancement of the upward arms is relatively small, indicating that only small surface charges are induced at this wavelength. When the polarization angle β = 30° and 60°, the contour plots, Figs. 3.20(b) and 3.20(c), illustrate the tilted *E*-field distribution. When the polarization angle increase to 90° and becomes *s* polarized incidence (Fig. 3.20(d)), the *E*-field distribution congregates into the groove of the V-shape formed by the top two arms. Figure 3.20(e) gives the polar plots of four particular locations around the Y-shaped nanorod. Position A is located around the corner of the bottom cylinder, positions B and C around the corners of two top arms and position D inside the top elbow. The maximum *E* field enhancement is located at Position A. With the increase of the polarization angle β, the enhancement γ decreases.

The polar plots can be fitted by

$$\gamma = C + D \sin^2(\beta + \varphi) \quad . \tag{3.2}$$

For the polar plot of position A, φ = 0°, which means the maximum *E* field enhancement occurs when the incident light is *p* polarized. For the polar plot of position D, φ = 90°, which means the maximum *E* field enhancement occurs at *s* polarization incidence. The polar plots of position B and C have φ = 28.5° and 151.5°, respectively. As the polarization angle β increases, the main plasmon peak λ_p decreases. The polar plots of the enhancement at position B and C also show the unequal *E* field distribution at a particular polarization. When the polarization angle increases from β = 0° to β = 60° (λ_p decrease from 1.061 μm to 1.053 μm), φ keeps a value close to 15°. When the angle continues to increase to β = 90° (λ_p = 0.982 μm), φ increases rapidly to 28.5°.

The two lines in Fig. 3.20(b) have angles of ~ 15° and ~25° with respect to the *p* polarization direction, respectively, which can be thought as the oscillation distance of induced charges in the Y-shaped nanorod.

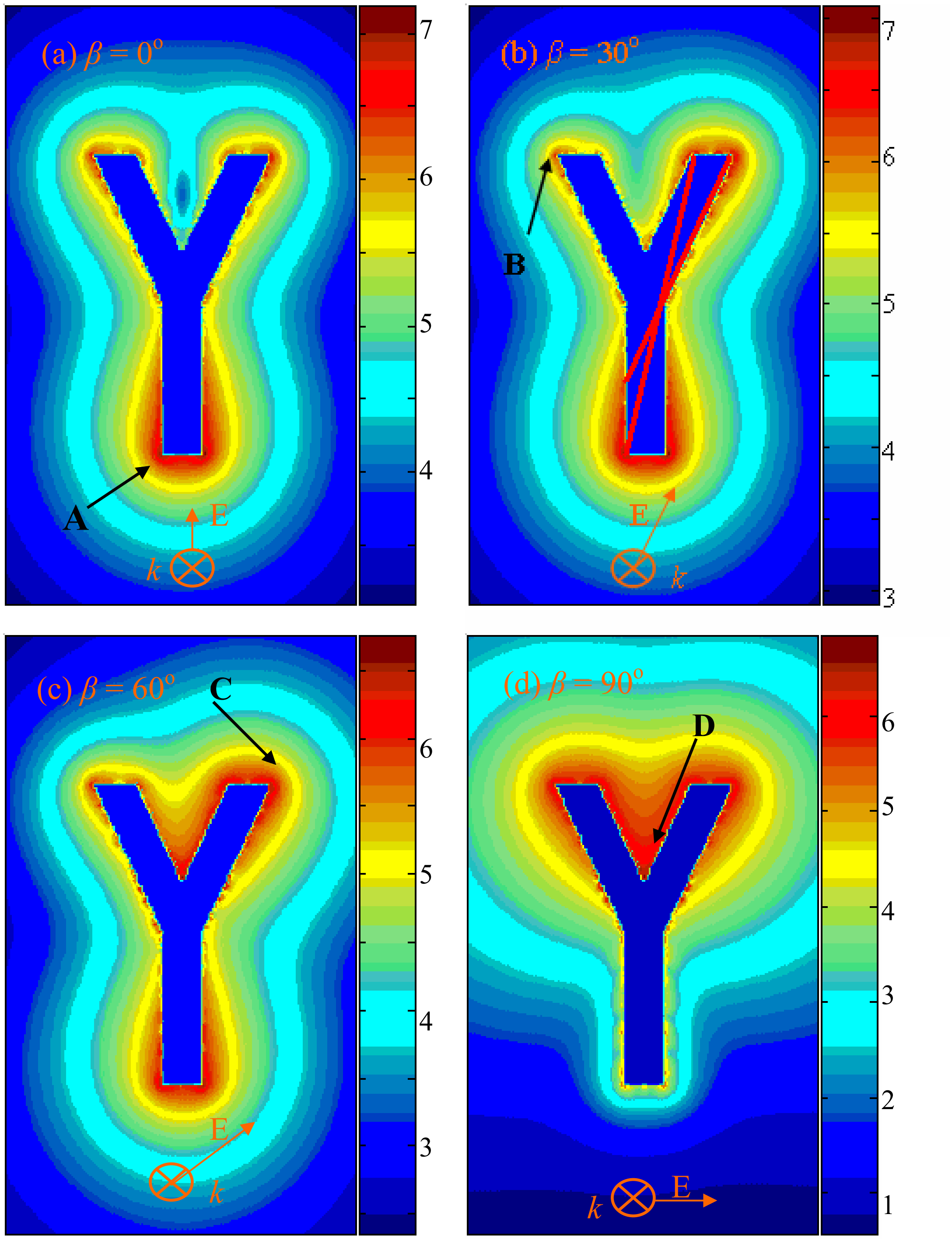

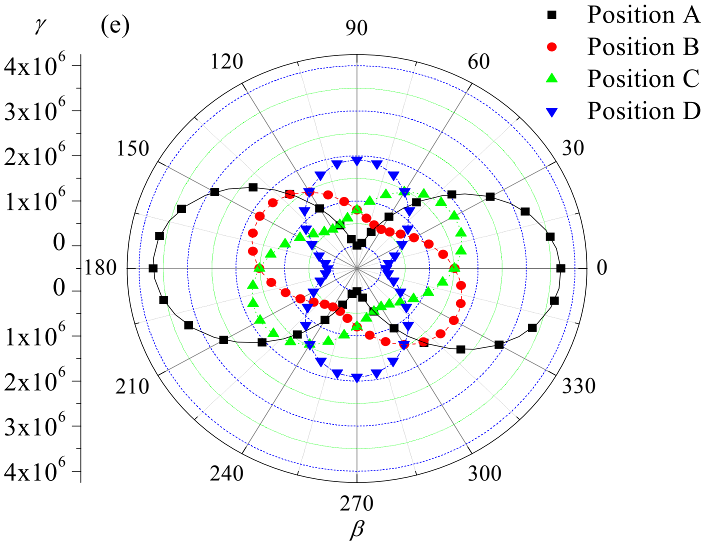

Figure 3.20 *E* field enhancement contours of L_Y = 160 nm Y-shaped nanorod at λ_p = 0.982 μm with different polarization angle β (a) $\beta = 0^{\circ}$, (b) $\beta = 30^{\circ}$, (c) $\beta = 60^{\circ}$, and (d) $\beta = 90^{\circ}$, respectively. (e) Polarization dependent field enhancement γ for several locations around the nanorod surface (Solid curves calculated by fitting Eq. 3.2).

As the slope of the lines in Fig. 3.20(b) increase the oscillation distance decreases, which results in the blue shift of the main plasmon peak. This makes the maximum *E* field enhancements occur around the top of two upper arms. This polarization dependent extinction spectra could be the reason for the anomalous absorbance spectra we have observed for Ag nanorod arrays[129], since the Ag nanorod array has branched nanorods similar to a Y-shape; they are aligned but randomly distributed on the surface. For the Y-shaped nanorods, the plasmon peak can also be tuned by changing the incident polarization angle. The *E* field enhancement distribution is tilted at a different angle with different incident polarization direction. These results would give more spatial information of the analyte when Y-shaped nanorods are used as the substrate for SERS detection.

3.7 Parallel-nanorod structure and U-shaped nanostructure

Figure 3.21 illustrates the topological structures of a U-shaped and a parallel-nanorod structure, and the polarization configuration of the incident light used in the calculations. The parallel-nanorod structure consists of two nanorods in the vertical direction with a radius *r* and a height *H*. The U-shaped nanostructure has an additional bottom cylinder in the horizontal direction with a radius *R* and a length *L* connecting the two vertical rods. In all the calculations, the excitation light propagates along the vertical direction with a horizontal polarization.

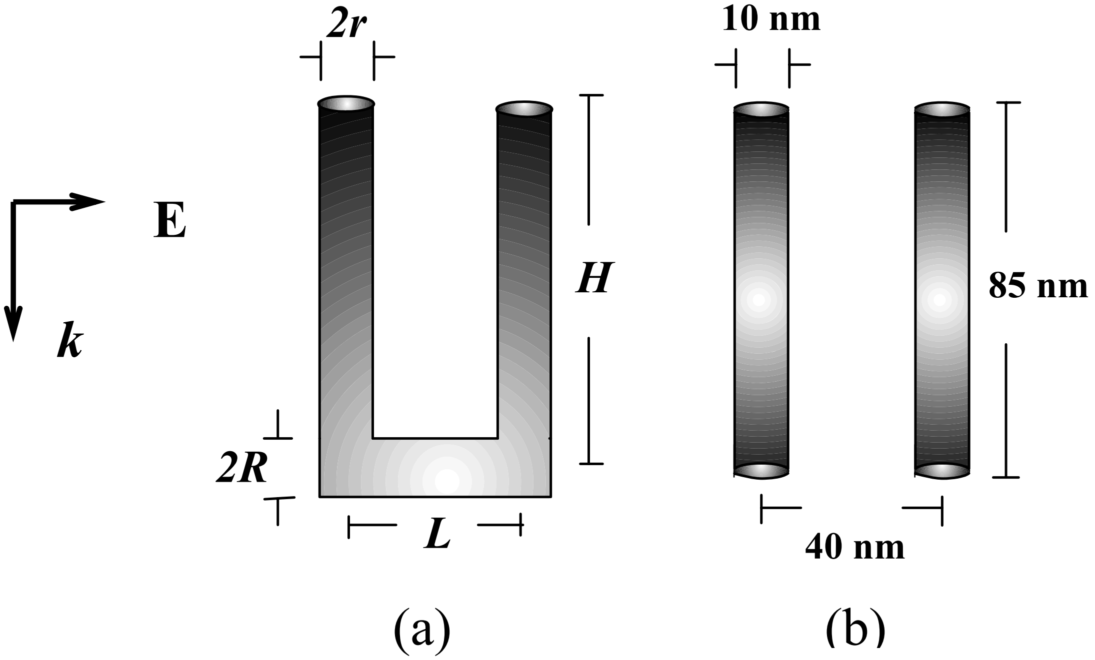

Figure 3.21 Schematics for the incident polarization, and (a) the U-shaped nanostructure and (b) the parallel-nanorod structure

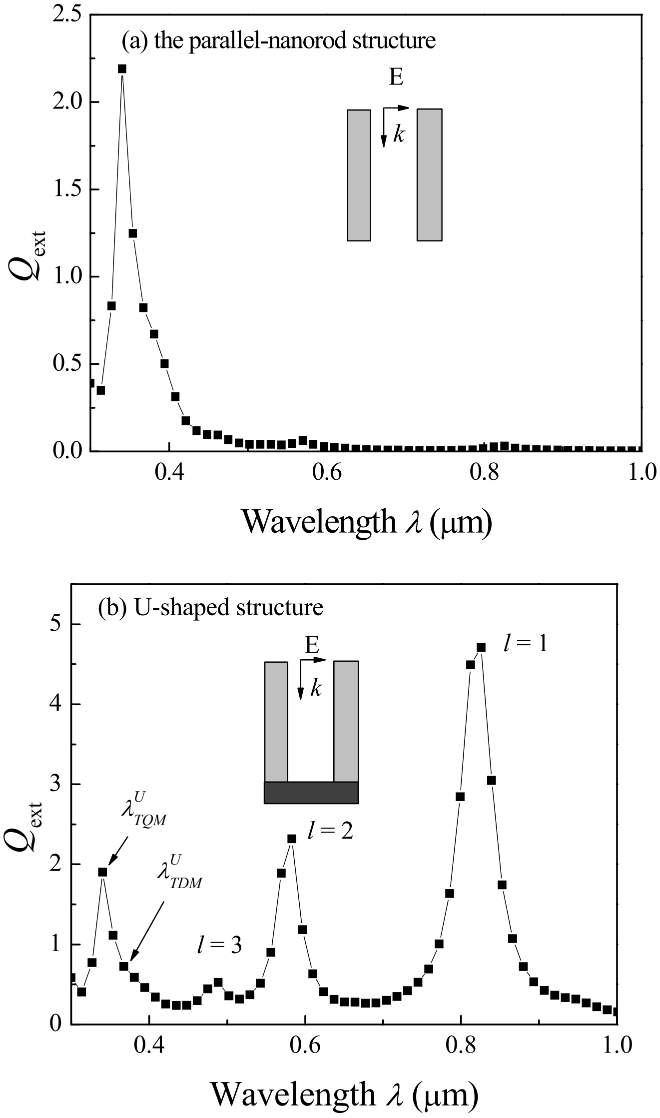

Figure 3.22 Calculated extinction spectra of (a) the parallel-nanorod structure and (b) the U-shaped nanostructure

Figure 3.22(a) plots the extinction spectrum of a parallel-nanorod structure with $r = 5$ nm, $H = 85$ nm, and $L = 40$ nm. The extinction spectrum has two peaks: the peak located at the longer wavelength (λ^{C}_{TDM} = 0.359 μm) is called the transverse dipole mode (TDM); and the peak located at the shorter wavelength (λ^{C}_{TQM} = 0.341 μm) is called the transverse quadrupole mode (TQM). When the incident light has a TDM wavelength, the maximum *E* field enhancement (γ ~3.4×10^{5}) occurs around the side wall of each individual nanorod (Figure 3.23 (a)) and demonstrates a weak field coupling between the two nanorods. When the incident light has a TQM wavelength, the *E* fields are also coupled into the space between two nanorods (Figure 3.23 (b)). However, the maximum *E* field enhancement occurs not only at the tip of the nanorods but also around the contour of the parallel-nanorod surfaces. The maximum field enhancement γ is ~ 6.8×10^{4}.

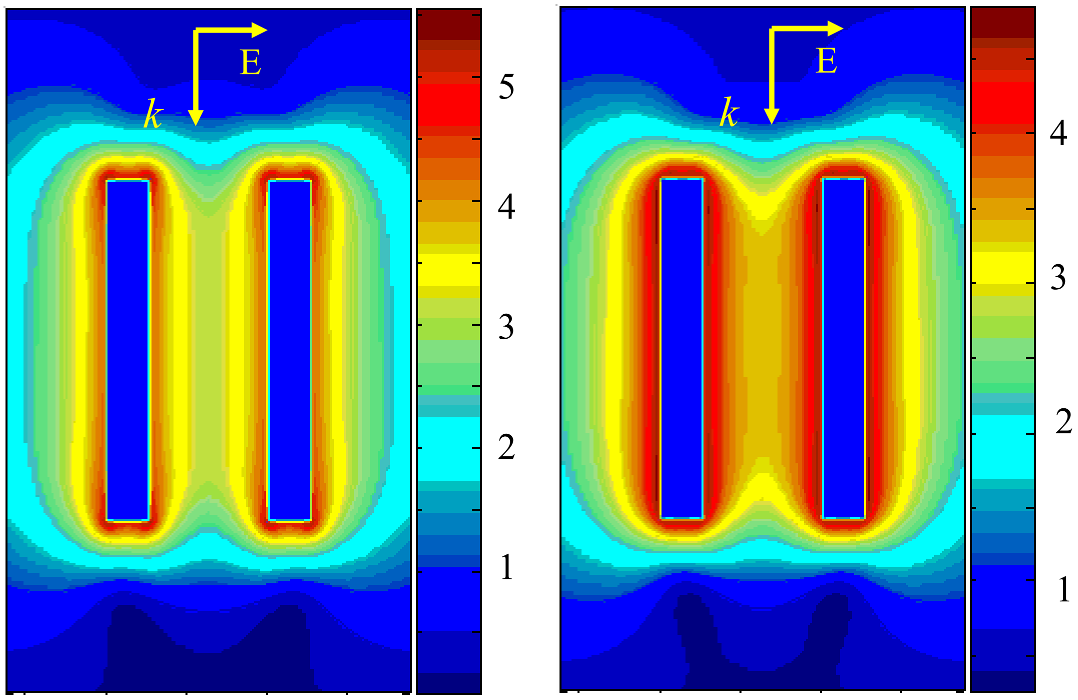

(a) λ^{C}_{TDM} = 0.359 μm (b) λ^{C}_{TQM} = 0.341 μm

Figure 3.23 *E* field enhancement contours ($\log_{10}\gamma$) of the parallel-nanorod structure at different incident wavelengths: (a) λ^{C}_{TDM} = 0.359 μm and (b) λ^{C}_{TQM} = 0.341 μm

When a bottom nanorod is used to connect the two parallel nanorods, a U-shaped nanostructure is formed. Figure 3.22(b) plots the extinction spectrum of a U-shaped nanostructure with R = 5 nm, H = 80 nm, L = 40 nm, and r = 5 nm. Besides the plasmon peaks around λ_{TDM}^{C} = 0.36 μm and λ_{TQM}^{C} = 0.34 μm, which are observed in the parallel-nanorod structure, three more peaks appear at λ_p = 0.82 μm, 0.579 μm, and 0.485 μm, respectively. The extinction efficiency at λ_p = 0.82 μm has the highest value, and the plasmon peak at λ_p = 0.485 μm has the smallest magnitude. The E field enhancement distributions are determined by the induced charge oscillation modes for each of the extinction peaks, as shown in Fig. 3.24.

At λ_p = 0.82 μm, as shown in Fig. 3.24(a), E fields are coupled in the space between two vertical nanorods. A pins-like distribution occurs around the surface of each vertical nanorod. The maximum E field enhancement is ~ 6.7×10^6, which is much larger than those at TM wavelengths of the parallel structure. Under this condition, one could vision that there are three dipole oscillations that have been excited along the U-shaped nanostructure: One dipole oscillation occurs along the long axis of the bottom nanorod and two dipole oscillations occur in the vertical nanorods, as indicated by the arrows in Fig. 3.24(a). There is strong E field coupling between the two vertical nanorods. This oscillation behavior is similar to the longitudinal plasmon mode (LM) of the vertical nanorods. In fact, for the parallel-nanorod structure with r = 5 nm, H = 85 nm, and L = 40 nm, its LM mode wavelength is λ_p = 1.043 μm. We use l = 1 to denote this resonance mode. At λ_p = 0.579 μm, as shown in Fig. 3.24(b), the E fields between the two vertical nanorods are coupled. The maximum E fields distribute around the top, the middle, and the bottom of the U-shaped nanostructure, and the magnitude is ~1.5×10^6, which is also much larger than those of the parallel-nanorod structure. One could use five dipoles to simulate the field oscillations as illustrated by the arrows in Fig. 3.24(b). We use l = 2 to denote this

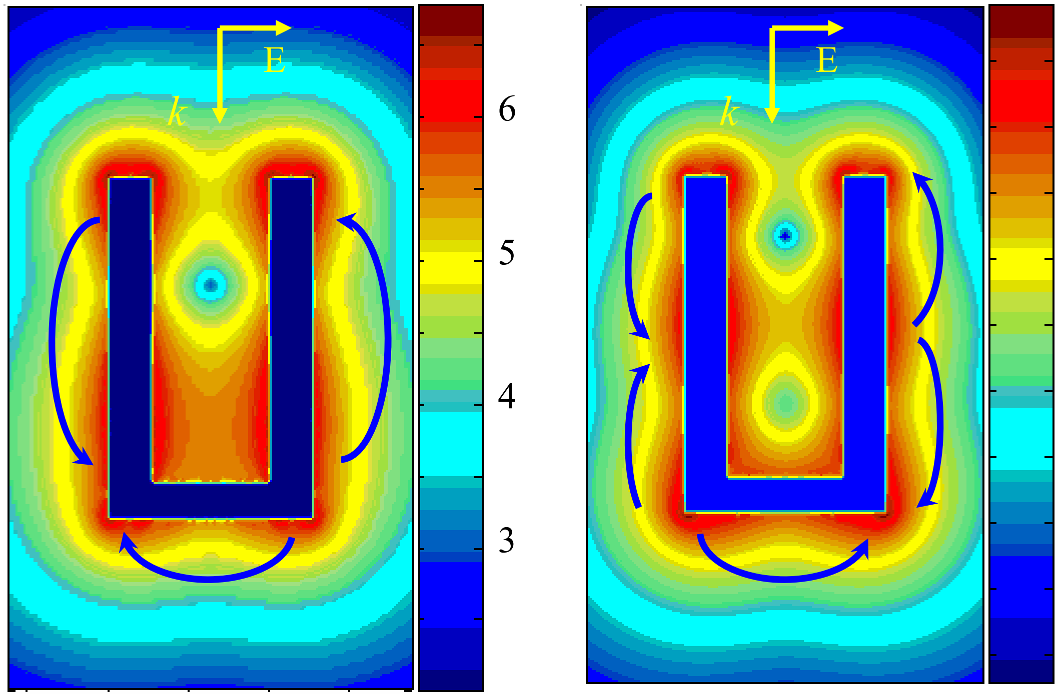

(a) $\lambda_p = 0.820$ µm (b) $\lambda_p = 0.579$ µm

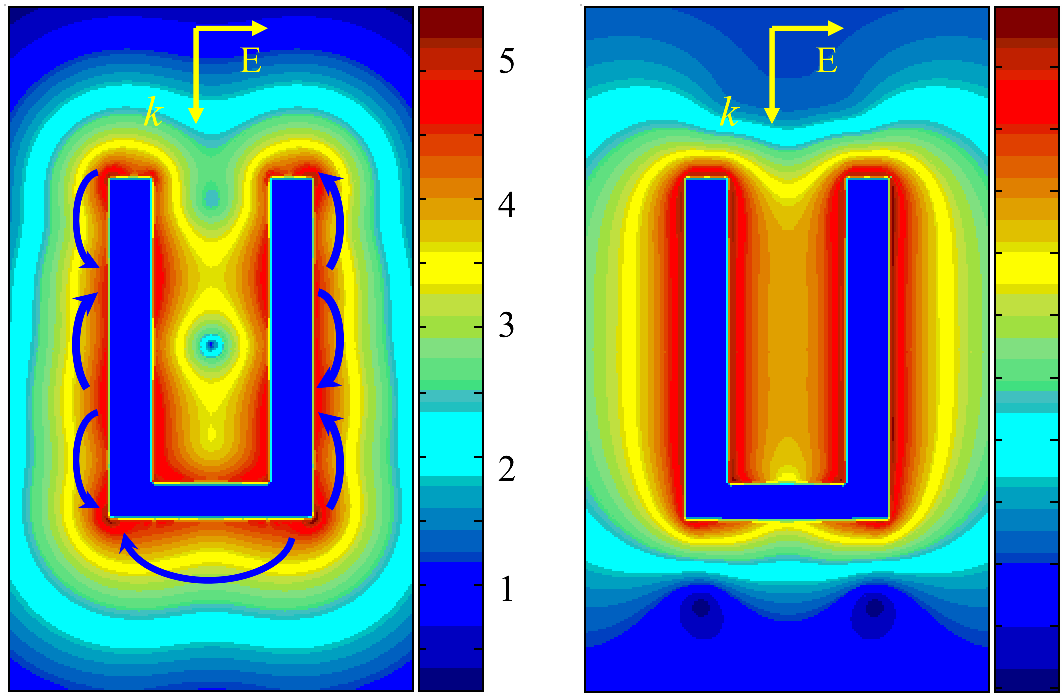

(c) $\lambda_p = 0.485$ µm (d) $\lambda_{TQM}^{U} = 0.341$ µm

Figure 3.24 *E* field enhancement contours ($\log_{10}\gamma$) of the U-shaped nanostructure at different incident wavelengths: (a) $\lambda_p = 0.82$ µm, (b) $\lambda_p = 0.579$ µm, (c) $\lambda_p = 0.485$ µm, and (d) $\lambda_{TQM}^{U} = 0.341$ µm plasmon resonance mode. At λ_p = 0.485 μm, as shown in Fig. 3.24(c), the maximum *E* fields occur at the top, ¼ from the top, ¾ from the top, and the bottom of the U-shaped nanostructure, with a magnitude $\gamma \sim 2.2\times10^5$, which is one order of magnitude smaller than those at $l = 1$ and $l = 2$ modes. When a single nanorod with the radius of 5 nm and the height of 85 nm is irradiated under longitudinal mode (the incident *E* field is parallel to the height), the quadrupole plasmon peak occurs at 0.488μm and the maximum *E* fields also occur around the two ends and ¼ from two ends. The similar plasmon peak and *E* field distribution demonstrate that this plasmon mode consists of the quadrupole oscillations in two vertical nanorods and the dipole oscillation in the bottom nanorods, as illustrated by the arrows in Fig. 3.24(c). We use $l = 3$ to denote this resonance mode. The plasmon wavelength seems inversely proportional to the number of the dipoles illustrated in Fig. 3.24. The l = 1, 2, and 3 mode with a wavelength ratio of 0.82 : 0.579 : 0.485 ≈ 1.69 : 1.19 : 1, while the inverse number ratio of dipole on the nanostructure is 1/3 : 1/5 : 1/7 ≈ 2.33 : 1.4 : 1. A monotonic relationship is revealed. The peaks at λ_{TQM}^{U} = 0.341 μm and λ_{TDM}^{U} = 0.36 μm are due to the TM modes of the two vertical nanorods. Figure 3.24(d) shows the *E* field enhancement distribution of U-shaped nanostructure at λ_{TQM}^{U} = 0.341 μm. The *E* field distribution is very similar to that of Fig. 3.24(b), in fact the field at the bottom looks like it is penetrating the bottom nanorod. Thus, the plasmon peak at λ_{TQM}^{U} = 0.341 μm is due to the TQM mode of vertical nanorods. Similarly, the plasmon peak at λ_{TDM}^{U} = 0.36 μm is due to the TDM mode of vertical nanorods.

The comparison of the U-shaped and parallel-nanorod structure reveals that the addition of the bottom nanorod to bridge the two vertical nanorods can help to induce multiple plasmon resonance modes. Meanwhile, since the incident *E* field is perpendicular to the vertical nanorods in the parallel-nanorod structure, it can only excite the TM plasmon oscillation, while for the U-shaped nanorod, the horizontal incident *E* field could produce excitation in the bottom nanorod, and those electrons can transport through the vertical nanorods to induced multimode LM plasmon resonance along the vertical nanorods. Moreover, when light incident with the wavelengths of $l = 1, 2, 3$ modes, the *E* fields at the bottom of the U-shaped nanostructure are at least one order of magnitude larger than those at the bottom of the parallel structure when light is incident with TM modes, and there are more surface areas that have large field distribution. These greatly benefit the SERS enhancement when U-shaped nanostructures are used compared to parallel-nanorod structured substrates.

3.8 Conclusion

The extinction spectra and the *E* field enhancement distribution of cylindrical, needle-like, periodic, L-shaped nanorods, Y-shaped nanorods, parallel-nanorod structures and U-shaped nanostructures were investigated.

Cylindrical and needle-shaped nanorods have only one longitudinal mode and the maximum *E* field appears at the tips. Periodic nanorods have several longitudinal modes caused by the structure, resulting in many different *E* field distributions. L- and Y-shaped nanorods break cylindrical symmetry, causing further complications in the *E* field distribution. With specific polarization incident, the maximum *E* field can be located around the surface or congregated on the top of the Y shape. Although the maximum *E* field varies according the nanorod shape, they are mostly in the same order of magnitude. However, the nanorods with complicated shapes, such as periodic, L- and Y-shapes, have more hot spots than that of a perfectly cylindrical nanorod. Thus, one will have more opportunity to observe SERS from a small amount of molecules on irregular nanorods than a cylindrical nanorod. The polarization dependent extinction spectra have also been calculated using DDA. Because L- and Y-shaped nanorods break the cylindrical symmetry, they can be used to vary the *E* field distribution shape by changing the polarization angle. All these results help us to understand the optical properties and field enhancement of irregular nanorod structures.

The electrons in the parallel-nanorod structure can only oscillate within the individual nanorods, and only when these two rods are close enough, the coupling could affect the plasmon resonance frequency. For the U-shaped nanostructure, the bottom rod builds a path to connect the two vertical nanorods, so that electrons of the three sections are coupled together, and LM plasmon oscillation along the vertical nanorods can be excited by longitudinal *E* field excitation. For the parallel-nanorod structure, only TM plasmon mode in the UV region can be excited, while for the U-shaped nanostructure, not only TM modes can be excited, the LM modes and multiple modes can be also excited. The *E* field enhancements at these resonant peaks are much larger than those of the parallel-nanorod structure. The large enhancements distribute not only around two vertical nanorods but also on the bottom of the U-shaped nanostructure. Therefore, for sensing and analytical purposes, the U-shaped nanostructure has more hot surface areas to capture and detect small amount of molecules. This in part shows the importance of the under layer in the SERS nanorod substrate.

CHAPTER 4

OPTICAL PROPERTIES OF HELICAL NANOSTRUCTURES

4.1 Introduction

Polarized light will interact differently with helical structures than with conventional thin films. In particular, the helicity can rotate the polarization direction of a linear polarized light, which is termed as optical rotation or optical activity. These structures will also interact differently with left and right circularly polarized light, giving the well-known phenomena of circular birefringence and circular dichroism[130].

The phenomenon of optical activity has been studied in different material systems and engineered materials. In nature, liquid crystal molecules can possess helicity and can be used as display devices[131, 132]. Additionally, man-made helical structures can also be realized. In 1959, Yong and Kowal used physical vapor deposition (PVD) to fabricate helical fluorite films using a rotating substrate[133]. They demonstrated that this kind of thin film could rotate the plane of the polarization of normally incident light[133]. Later, Motohiro and Taga used an oblique angle deposition (OAD) technique to fabricate the simple chevron films of metal oxides, and studied their birefringent properties[134]. In 1992, Azzam proposed a method to deposit chiral thin solid films (CTSFs), which could be useful in making optical rotators and beam splitters [135]. Robbie and Brett fabricated the aligned three dimensional sculptured thin films using a glancing angle deposition (GLAD) method, and demonstrated their optical activity [124, 136]. They found that a porous TiO_2 helical thin film would select reflection of circularly polarized light and when the pitch height was increased, the reflection band was shifted to longer wavelength. In the above studies, all the helical structures are made from dielectrics, and they usually have small absorbance in the wavelength regions studied. However, metal helical structures have a large dielectric loss and a strong wavelength dependence of the dielectric constant, especially at the wavelength where surface plasmon resonance is occurred. Therefore, the optical properties of helical structures made from materials such as noble metals like Ag and Au will be expected to be very different from those made from dielectrics.

Experimentally, metal helical structures can be fabricated by the GLAD method as long as the metal can be evaporated. For example, Cu, Ni, and Cr helical structures are fabricated by etching the perforated thin films after GLAD deposition[124, 137]. One would expect that the metal helical nanostructures provide another way to tune the plasmon peak and rearrange the *E* field distribution.

4.2 DDA Calculation

Figure 4.1 shows the shape of a right-handed Ag helical nanostructure and the definitions of polarizations used in DDA calculations in our study. The *R* represents the helical radius and *r* represents the radius of the cross section. The *h* is the pitch height and the *H* is the total height of the helix. We consider two incident directions, one perpendicular to helical axis (*x*-axis) and the other along helical axis (*z*-axis) as shown in Fig. 4.1. With the incident direction perpendicular to the helix, the longitudinal polarization (LP) is defined as the *E* field along the helical axis and the transverse polarization (TP) is defined as the *E* field perpendicular to the helical axis. For *x*-axis polarization (XP), *y*-axis polarization (YP), right-handed circular polarization (RHCP), and left-handed circular polarization (LHCP), the incident direction is along the helical axis as shown in Fig. 4.1. The XP is defined as the direction of the *E* field parallel to *x*-axis; the YP is defined as the direction of the *E* field parallel to *y*-axis. For all the DDA calculation in this chapter, the lattice spacing of the dipoles is fixed at 2 nm.

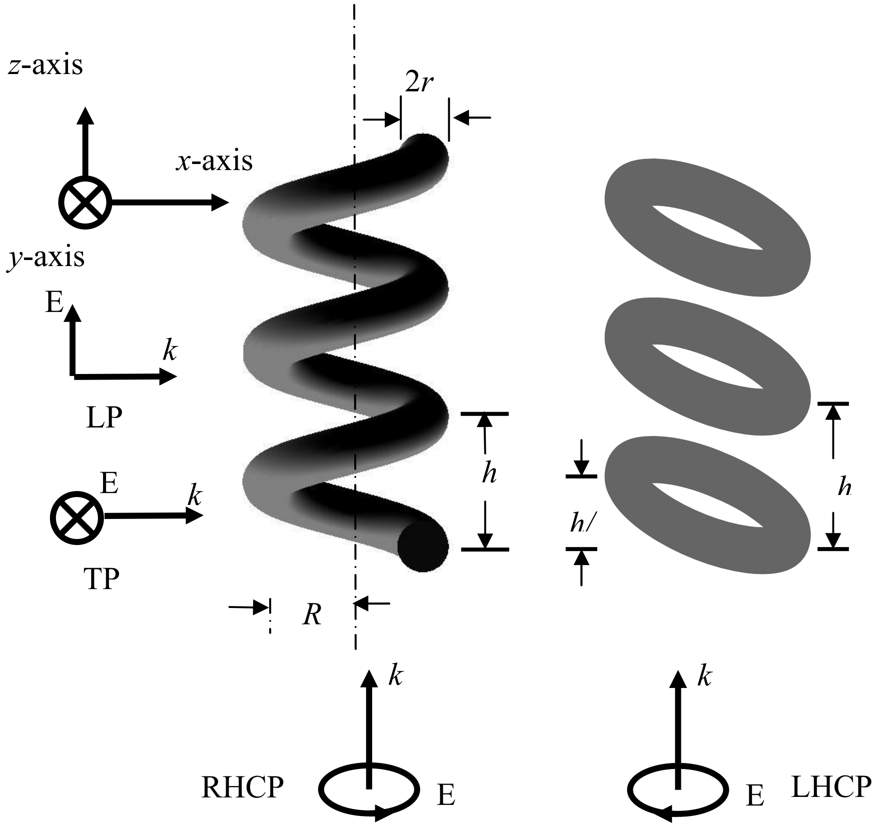

Figure 4.1 Schematics for the right-handed helical nanostructure and the multi-ring structure. The definitions of the incident polarization directions used in the DDA calculations are also shown.

4.3 Polarization dependence

For the polarization dependent calculations, the right-handed helical Ag structure has three pitches. The pitch height *h* is 50 nm. Therefore, the total height *H* is 150 nm. The helix radius *R* is 30 nm. The radius of the cross section *r* is 10 nm.

For a comparison, the optical properties of multi-ring structure are also studied. The multi-ring structures have three parallel rings (corresponding to three pitches of helix) which are tilted with respect to *x*-*y* plane as shown in Fig. 4.1. The tilting angle is determined by the corresponding helical structures. The height difference of the center of one ring at the tilting direction is *h*/2. Like the helical structure, the distance between two adjacent rings is the same as the pitch height *h* and *r* is the radius of the cross section of the tilted ring. The projected shape of the tilted rings along the main axis has a circular shape which has the same radius as that of helical structure.

Figure 4.2 summarizes the polarized extinction spectra of the helical and multi-ring nanostructures under LP, TP, *x*-axis, *y*-axis, RHCP, and LHCP incidences.

4.3.1 LP and TP incidences

For the helix under LP incidence, the extinction efficiency only has strong plasmon peaks at the UV region which is located at λ_{TM} = 0.365 μm and 0.345 μm. These peaks correspond to the transverse plasmon mode (TM) of Ag nanorods. One peak, located at a longer wavelength, is called the transverse dipole mode (TDM) while the other, located at a shorter wavelength, is called the transverse quadrupole mode (TQM) [99].

For comparison, Figure 4.2 (b) shows the extinction spectra of multi-ring structure under the LP incidence. Compared to the spectra of helical nanostructures, it has two major plasmon peaks: one located around λ = 0.35 μm, and the other located at λ = 0.594 μm. When the polarization direction is along the main axis of the multi-ring structure, the incident *E* field vector can be decomposed into two components, $E_{\perp}$ and $E_{//}$, where $E_{\perp}$ and $E_{//}$ are the components perpendicular and parallel to the tilting plane of each ring, respectively. The component $E_{\perp}$ excites the TM plasmon at a shorter wavelength while $E_{//}$ excites the longitudinal mode (LM) plasmon at a longer wavelength. Because the helical structure is a topologically continuous structure, there is no preferred tilt direction for the electron oscillation, and the excitation at any small section of the helix is the same. Therefore, there is no LM plasmon peak for the helical structures under LP incidence as compared to multi-ring structure.

Figure 4.3(a) and (b) illustrate the cross sectional view of the *E* field enhancement distribution for the helical nanostructure at the resonance wavelength λ_{TDM} = 0.365 μm and λ_{TQM} = 0.345 μm, respectively. The stronger *E* field occurs around the side surface of the helix and is coupled into the space between two adjacent pitches. At λ_{TDM} = 0.365 μm, the *E* fields around the right side of the pitch cross sections are much stronger than those around the left side of pitch cross sections. The *E* fields around the top and the bottom ends of the helical nanostructure are much stronger (~ 7.0×10^5) than those around two middle pitches (~ 1.0×10^5), which is similar to the *E* field enhancement distribution of cylinders excited at TDM wavelength[138]. At λ_{TQM} = 0.345 μm, there are similar *E* field enhancements around every pitch cross section. The *E* field enhancement distributions of the multi-ring structure excited at TM plasmon wavelength have a similar distribution as those of helical nanostructures. The stronger *E* field occurs near and surrounding the surface of the helix and there are electric field couplings in the space between two adjacent pitches. Under LP incidence, the collective oscillations across the cross-section are in-phase with the adjacent pitches, which produce strong electric couplings between adjacent pitches. Figure 4.3(c) illustrates the *E* field enhancement distribution of the multi-ring structure excited at λ_p = 0.594 μm. The maximum *E* field enhancements occur around the helix surface, and there are strong field couplings inside the helical structure, i.e., between the left pitch cross sections and the right pitch cross sections.

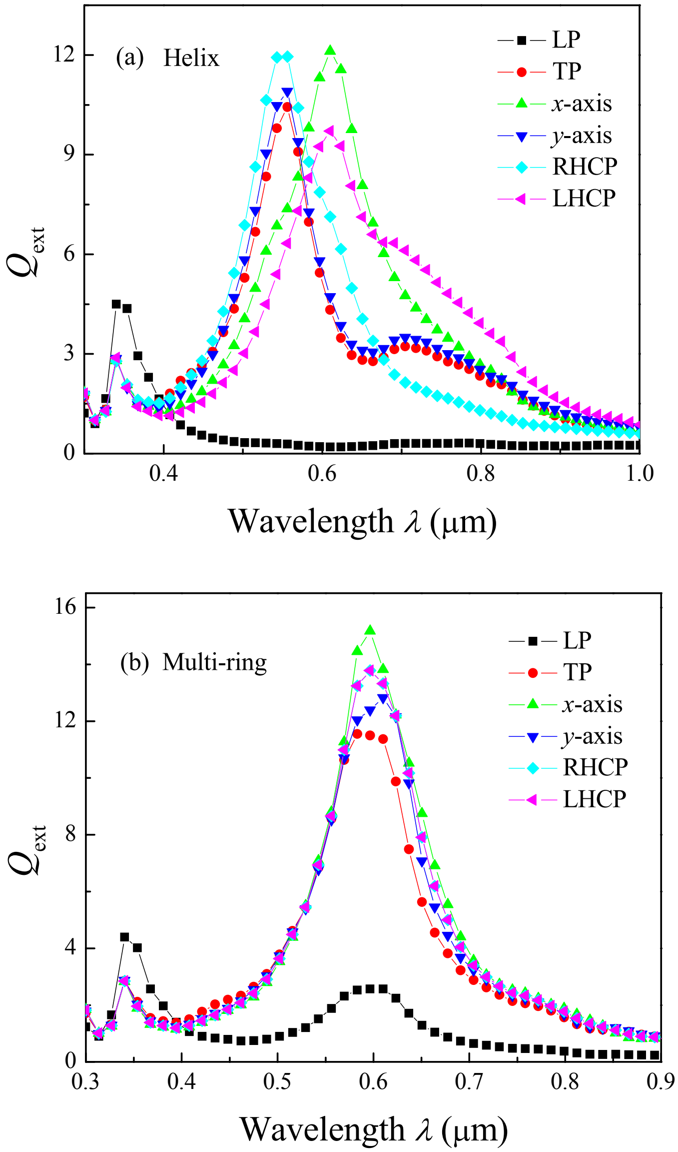

Figure 4.2 Calculated polarization dependent extinction spectra for (a) Ag helix and (b) Ag multi-ring

Under the TP incidence, multiple extinction peaks appear in the extinction spectra for helical nanostructures, as shown in Fig. 4.2(a). In addition to the UV absorbance peak at around $\lambda = 0.34$ μm, there are a strong plasmon peak at $\lambda_P = 0.554$ μm, and a broad extinction peak at $\lambda \sim$

0.7 μm on the right side of the plasmon peak. Figure 4.2(b) shows the extinction spectra of multi-rings under the TP incidence. The spectrum is very similar to that of helical nanostructure except with no broad extinction peaks at λ >0.6μm.

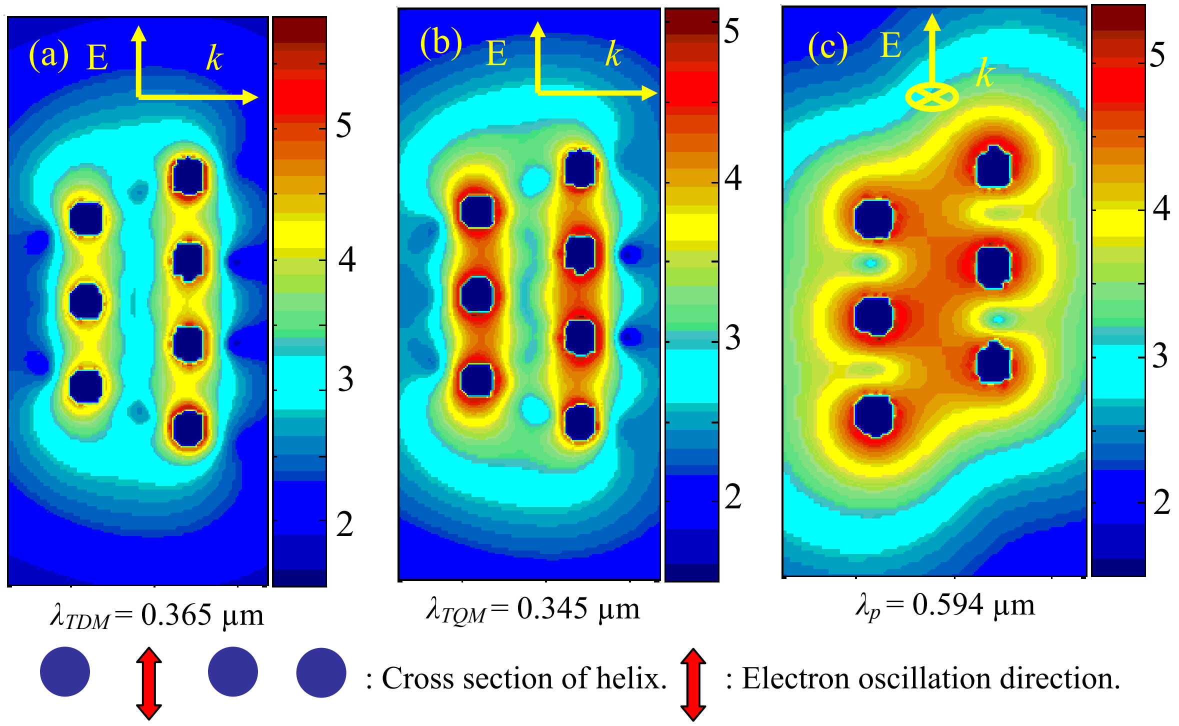

λ_{TDM} = 0.365 μm λ_{TQM} = 0.345 μm λ_p = 0.594 μm

Figure 4.3 The E field enhancement distribution contours ($\log_{10}\gamma$) of helical nanostructure at different incident wavelengths: (a) λ_{TDM} = 0.365 μm and (b) λ_{TQM} = 0.345 μm, and (c) multi-rings at λ_p = 0.594 μm. All the results are obtained under LP incidence.

Figure 4.4 illustrates the E field enhancement distribution of h = 50 nm helical nanostructure at λ_p = 0.554 μm. The maximum E field occurs around the surface of the helix, and there is strong coupling between the right pitch cross section and the left pitch cross section, which forms a zigzag shape inside the helix. The E field intensity (~ 10^6) is much stronger than those under the LP incidence (~ 10^5). At the incident wavelengths of the broad shoulder of main plasmon peak, there are the similar E field distributions as that of the main plasmon peak. For the multi-ring nanostructure excited at the main plasmon peak, there are similar *E* field distributions, as shown in Figs. 4.3(c).

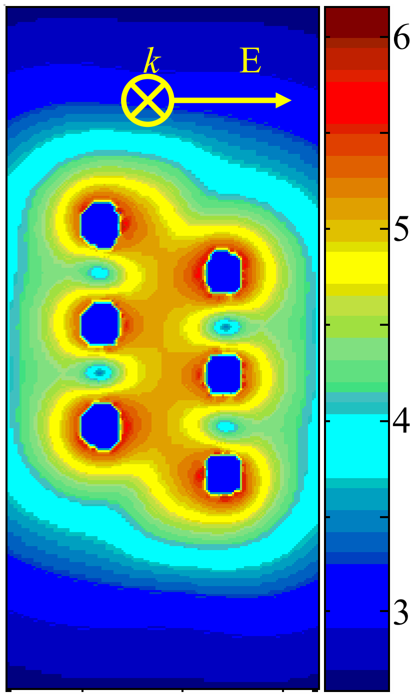

$\lambda_p = 0.554$ µm

Figure 4.4 *E* field enhancement contours ($\log_{10}\gamma$) of helical nanostructures under TP incidence at $\lambda_p = 0.554$ µm.

4.3.2 the *x*-axis and *y*-axis polarization incidences

For both XP and YP incidence, light propagates along the axis of the helix. Figure 4.2 (a) shows the extinction spectra under XP and YP incidence; the spectra are similar to those of multi-ring structure under TP incidence (Fig. 4.2(b)). In addition to the UV extinction peak at λ_{TM} = 0.34 µm, there is a strong plasmon peak appeared at λ_p = 0.614 µm for each spectrum. Compared to the spectra under TP incidence, there are no broad shoulders on the right side of the strong plasmon peak. The YP incidence has the same *E* field direction as that of TP incidence, thus they have the same extinction spectra (Fig. 4.2(a)). Under both XP and YP incident polarization, the E field enhancement distributions at the wavelength of the strong plasmon peak have a similar shape as those shown in Fig. 4.4, i.e., the distributions have the zigzag contour, and the maximum field enhancement is in the order of 10^6.

To better understand the polarization dependence of the extinction spectra, angular dependent polarized extinction spectra have been calculated every 10° by rotating the E field azimuthally starting under the XP incidence. Figure 4.5(a) plots the angular dependent extinction spectra of the helical nanostructure, where θ denotes the polarization angle with respect to the x-axis. With the increment of θ, the extinction efficiency Q_{ext} at the strong plasmon peak (λ = 0.553 μm) decreases, while the plasmon peak blue shifts. When $\theta > 40^{\circ}$, another observable plasmon peak at λ = 0.614 μm appears. The Q_{ext} at the new plasmon peak λ = 0.614 μm increases with θ until $\theta = 90^{\circ}$, and the Q_{ext} at the original plasmon peak λ = 0.553 μm decreases rapidly. Figure 4.5(b) shows the polar plots of the Q_{ext} at the wavelength λ_p = 0.614 μm and λ_p = 0.553 μm, respectively. The polar plot of extinction coefficient at λ_p = 0.614 μm has a 90° phase shift with respect to the plot at λ_p = 0.553 μm. The best equation to fit the data is given by

$$Q_{ext}(\theta) = A + B\sin^2\theta\,. \tag{4.1}$$

The solid curves in Figs. 4.8(b) and 4.8(c) are the results from the fitting using Eq. 4.1. In order to obtain the plasmon wavelength, since there are multiple peaks in the extinction spectra, Figure 4.5(c) shows the anisotropic polar plot of the weighted average wavelength $\bar{\lambda}_p$ ($\bar{\lambda}_p = \sum \lambda \cdot Q_{ext} / \sum Q_{ext}$) as a function of the polarization angle θ. When the incident direction is along the main axis of the helical nanostructure at an arbitrary polarization angle θ, the maximum E fields occur around the helix surface and there are field couplings inside the nanostructure, which is similar to the E field distribution under XP and YP incident light. It is clear that the plasmon peak can be tuned by changing the polarization angle θ.

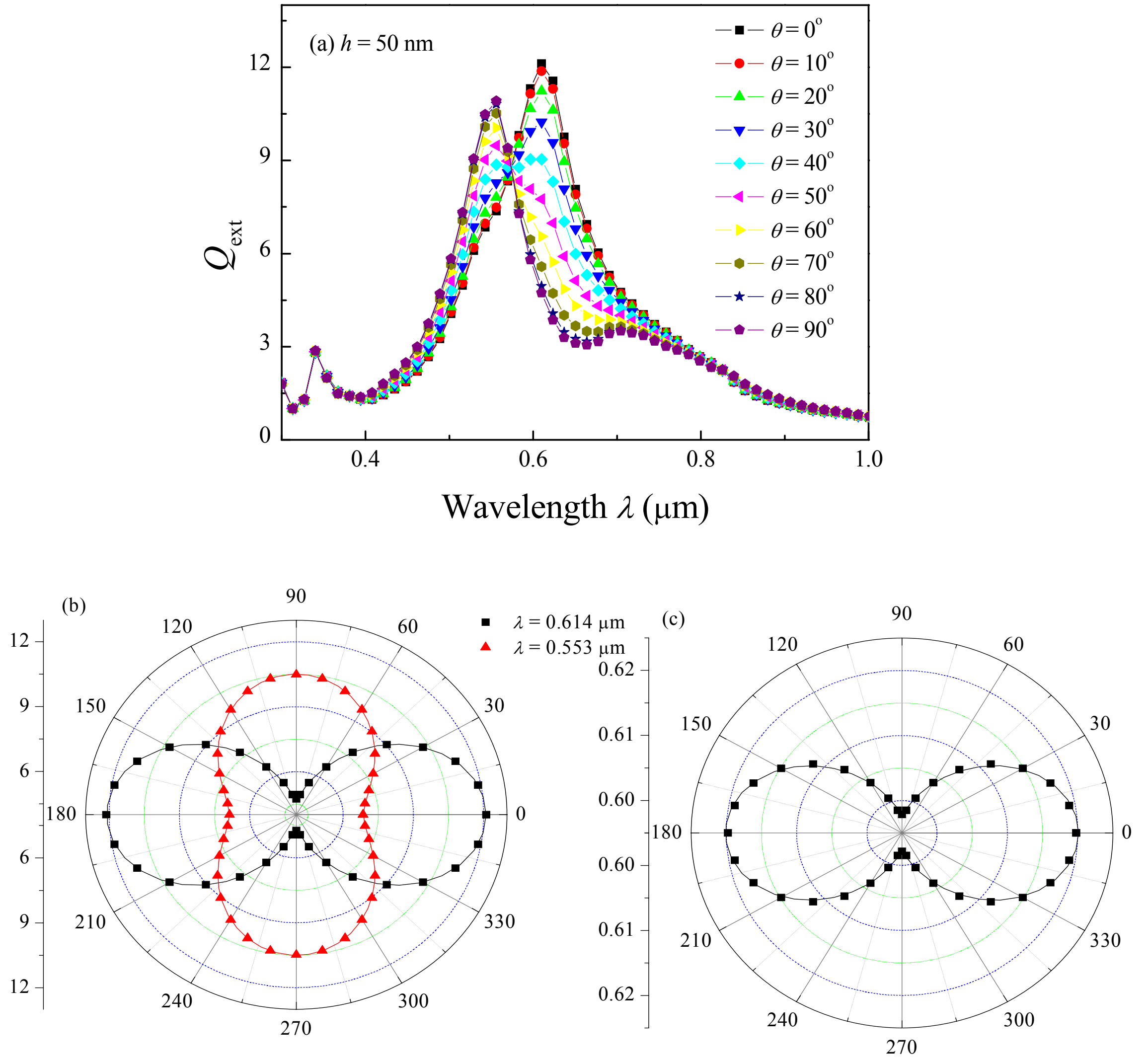

Figure 4.5 Extinction spectra for Ag helical nanostructure of h = 50 nm: (a) polarization dependent spectra, (b) polar plots of Q_{ext} at λ_p = 0.614 μm and λ_p = 0.553 μm, respectively; and (c) polar plot for weighted average plasmon peaks.

For the multi-ring nanostructure, under both XP and YP incidences, the extinction spectra are similar to those under TP incidence (Fig. 4.2(b)), and with the same plasmon resonance peaks. The extinction spectra are independent of the incident polarization angle θ and the polar plot of plasmon peak as a function of the polarization angle has a circular shape, a different result than that of helical nanostructures. Figures 4.6(a) and 4.6(b) illustrate the *E* field enhancement distributions of multi-ring structure at the plasmon peak λ_p = 0.6 μm under XP and YP incidences, respectively. The maximum *E* fields occur on the top ring of the multi-ring structures, and decreases from the top ring to the bottom ring. There are strong field couplings inside the top ring.

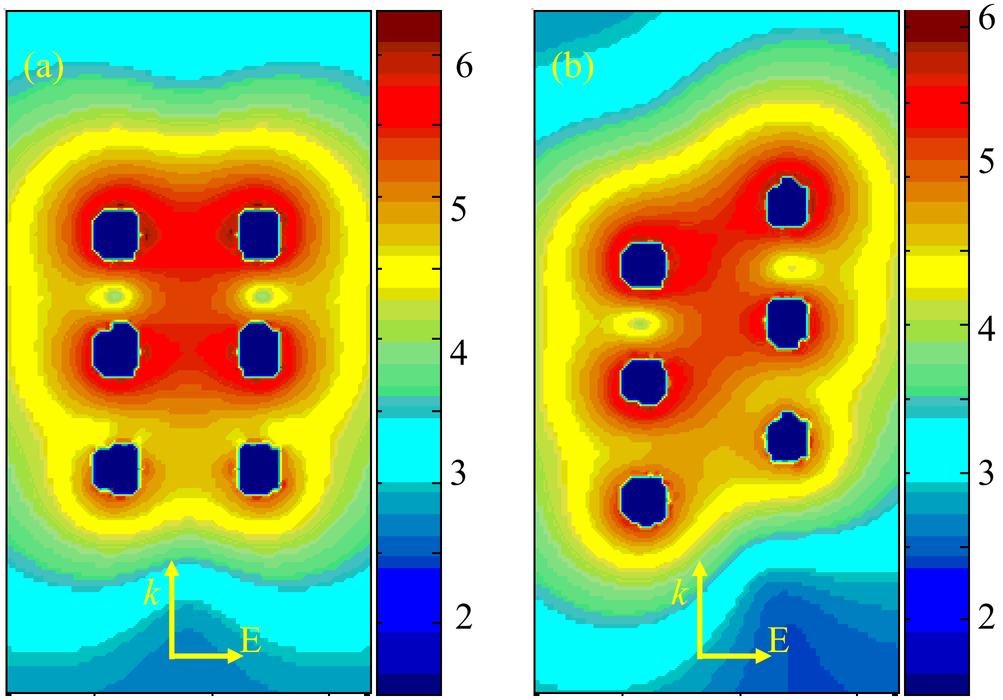

λ_p = 0.600 μm

λ_p = 0.600 μm

Figure 4.6 *E* field enhancement contours ($\log_{10}\gamma$) of multi-ring nanostructure at λ_p = 0.6 μm under different incident polarizations: (a) XP and (b) YP

4.3.3 RHCP and LHCP incidences

Under RHCP incidence, there are two plasmon peaks appeared in the extinction spectra for helical nanostructures: one small peak located around λ_{TM} = 0.34 μm and one dominant plasmon peak located at λ_p = 0.548 μm and under LHCP incidence, the plasmon peak red shifts to λ_p = 0.598μm, as shown in Fig. 4.2(a). The plasmon peaks at λ_p under LHCP incidence are broader than those under RHCP incidence. For the h = 50 nm helix, the FWHM under RHCP incidence is 130 nm, while the FWHM under LHCP incidence is 210 nm. It is well-known that circular polarization can be decomposed into two perpendicular linear polarizations, and we may use the following equation,

$$Q_{ext}(circular) = A(Q_{ext}(x)\cos^2\theta + Q_{ext}(y)\sin^2\theta), \tag{4.2}$$

to fit the extinction spectrum under circularly polarized incidence. Here $Q_{ext}(x)$ and $Q_{ext}(y)$ are the extinction spectra under the XP and YP incidences. The solid curves in Fig. 4.7 are the fittings resulted from Eq. 4.2. For both cases, the spectral portions at $\lambda \le \lambda_p$ can be fitted very well while the fitting at $\lambda > \lambda_p$ is not very good, especially at the shoulder. For the spectra obtained under RHCP incidence, the parameter θ_R increases from $\theta_R = 45^\circ$ at h = 24 nm monotonically to $\theta_R = 88^\circ$ at h = 60 nm. For the spectra obtained under LHCP incidence, the parameter θ_L decreases from $\theta_L = 45^\circ$ at h = 24 nm monotonically to $\theta_L = 2^\circ$ at h = 60 nm. It is interesting to note that $\theta_R + \theta_L = 90^\circ$.

Figure 4.8(a) illustrates the E field enhancement distribution of the h = 50 nm helix at λ_p = 0.548 μm under RHCP incidence. The maximum E fields (~ 2.0×10^6) congregate at the bottom of the helical nanostructure. Figure 4.8(b) illustrates the E field enhancement distribution of the h = 50 nm helix at λ_p = 0.598 μm under LHCP incidence. The maximum E field enhancement (~ 6.0×10^6) is distributed at the top of the helix. In our calculation, the helix is a right-handed helical nanostructure. Therefore, when the nanostructures have the same helicity with incident polarized light, the maximum E field occurs at the bottom of the helix. When the nanostructures have the opposite helicity compared to the incident polarized light, the maximum E field occurs on the top of the helix.

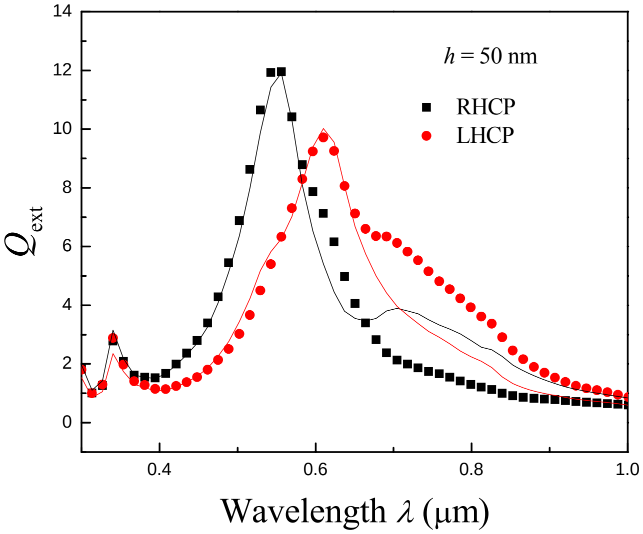

Figure 4.7 Extinction spectra of h = 50 nm helix under circularly polarized incidence and the fitting curves using Eq. 4.2.

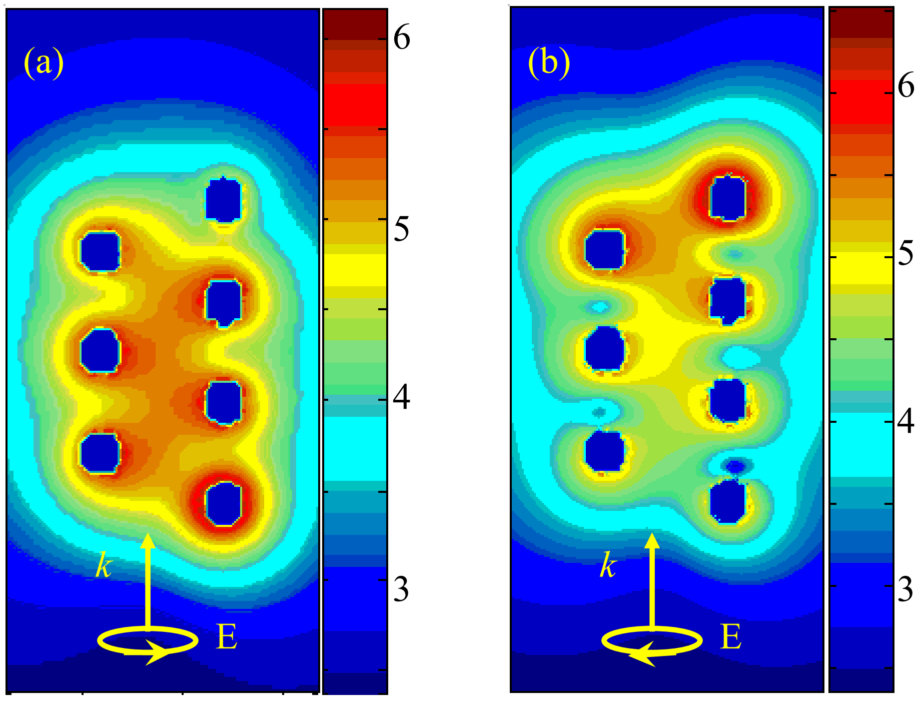

$\lambda_p = 0.548$ μm

$\lambda_p = 0.598$ μm

Figure 4.8 E field enhancement contours ($\log_{10}\gamma$) of the helix under different circular polarization and wavelength (a) RHCP *and* $\lambda_p = 0.548$ μm; (b) LHCP and $\lambda_p = 0.598$ μm.

For the multi-ring nanostructures, RHCP and LHCP give similar extinction spectra as the polarization perpendicular to the main axis (Fig. 4.2(b)). The maximum *E* field always occurs on the top of the structure, which has a similar *E* field distribution as shown in Fig. 4.6.

4.3.4 Conclusion

From the above calculations, it is found that the Ag helical nanostructure is another good structure to tune the plasmon peak and arrange the *E* field distribution. Even without changing the structure, the plasmon peak can be tuned by changing the polarization of the incident light. In addition, the spatial distribution of the maximum *E* field can be adjusted by changing the polarization directions of the incident light. Therefore, for sensing and analytical purpose, different polarizations of incident provide a simple way to spatially distinguish the analyte's location in the helix. Thus, a spatially resolved analyte's information can be obtained. In fact, this can be used to resolve the spatial distribution of the analyte in submicrometer length scale.

Because there is no helicity of the multi-ring structure, when light incident along the axis of the rings, the extinction spectra are polarization independent and the maximum *E* fields always occur on the top.

4.4 Pitch height dependence

For the pitch height dependent calculation, the right-handed helical Ag structures have pitches. The pitch height h varies from 24 to 60 nm. The total height H changes from 72 to 180 nm. The helix radius is $R = 30$ nm. The radius of the cross section is $r = 10$ nm.

4.4.1 LP and TP incidences

The extinction efficiencies of Ag helices with different pitch heights under the LP incidence are shown in Fig. 4.9. With the increase of the pitch height *h*, the plasmon peaks blue shift from λ_{TDM} = 0.399 μm and λ_{TQM} = 0.362 μm at *h* = 24 nm to λ_{TDM} = 0.363 μm and λ_{TQM} = 0.344 μm at *h* = 60 nm. The full-width-at-half-maximum (FWHM) of two combined strong plasmon peaks decreases from 90 nm at *h* = 24 nm to 45 nm at *h* = 60 nm.

Under LP incidence, there are similar *E* field distributions as shown in Fig. 4.3(a, b). With the increase of the pitch height *h*, the coupling between two adjacent pitches becomes weaker, which decreases the effective induced charge separation and blue shifts the plasmon peak to λ_{TDM} = 0.363 μm and λ_{TQM} = 0.342 μm for a single-pitch helix.

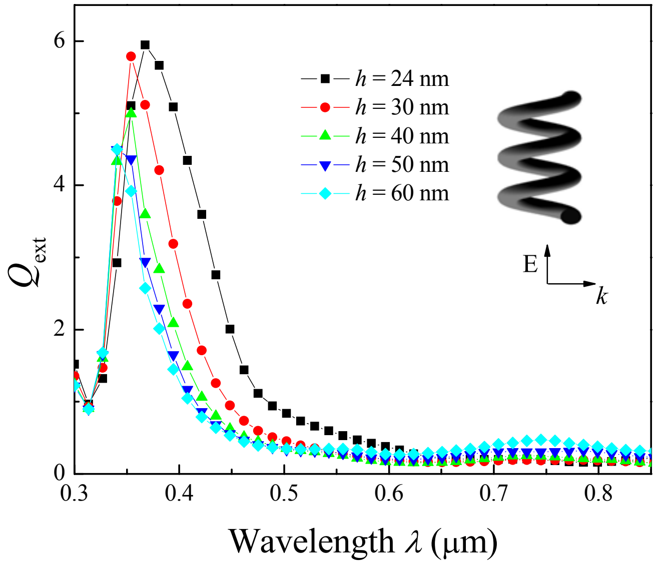

Figure 4.9 Pitch height dependent extinction spectra for Ag helical nanostructures under LP incidence.

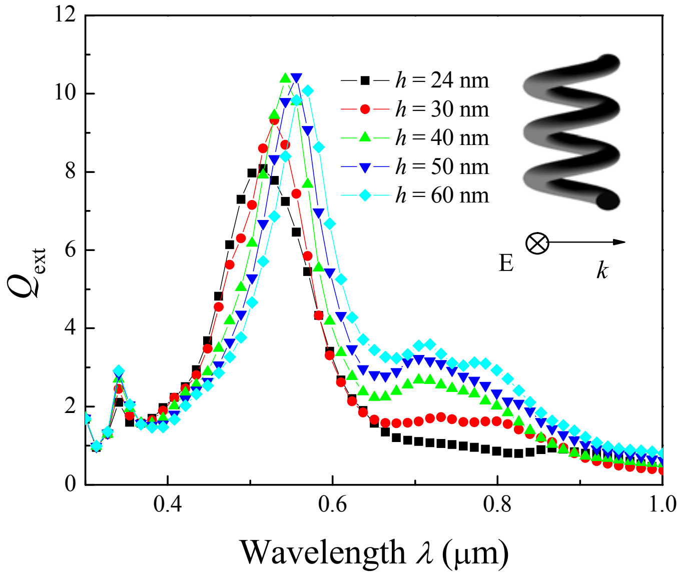

Figure 4.10 Pitch height dependent extinction spectra for helical nanostructures under TP incidence.

Under the TP incidence, multiple extinction peaks appear in the extinction spectra for helical nanostructures, as shown in Fig. 4.10. In addition to the UV absorbance peak at around $\lambda = 0.34$ μm, there are a strong plasmon peak at $\lambda_P \sim 0.5 - 0.56$ μm, and a broad extinction peak at $\lambda \sim 0.65 - 0.8$ μm on the right side of the plasmon peak. For different h, the UV extinction peaks located around $\lambda_{TM} = 0.34$ μm are due to the electron oscillation perpendicular to the cross section of each pitch. With the increase of h, the strong plasmon peaks red shift from $\lambda_p = 0.518$ μm at $h = 24$ nm to $\lambda_p = 0.564$ μm at $h = 60$ nm, as shown in Fig. 4.11. On the right side of the strong plasmon peaks, there is one broad shoulder. Figure 4.12 illustrates the E field enhancement distribution of $h = 30$ nm helical nanostructure at $\lambda_p = 0.532$ μm. The field distribution also has a zigzag shape. However, with the decrease of h, the total height of the zigzag shaped E field distribution decreases and strong coupling between two adjacent pitches occur.

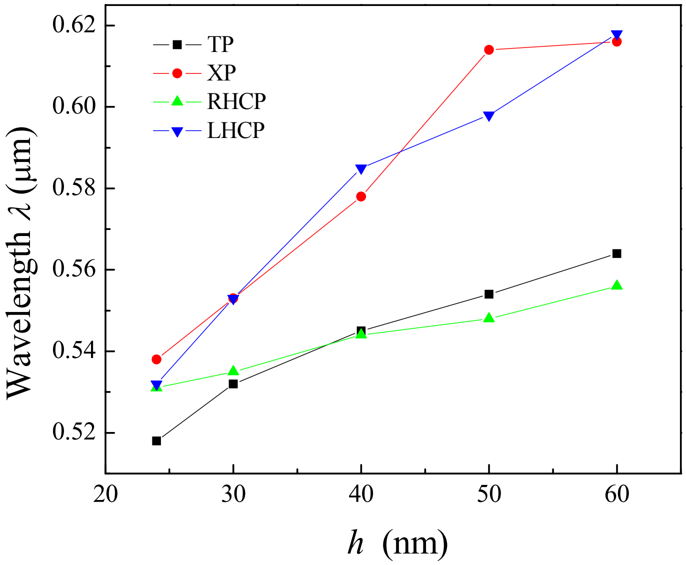

Figure 4.11 The wavelength of plasmon peaks under different incident polarizations as a function of *h*.

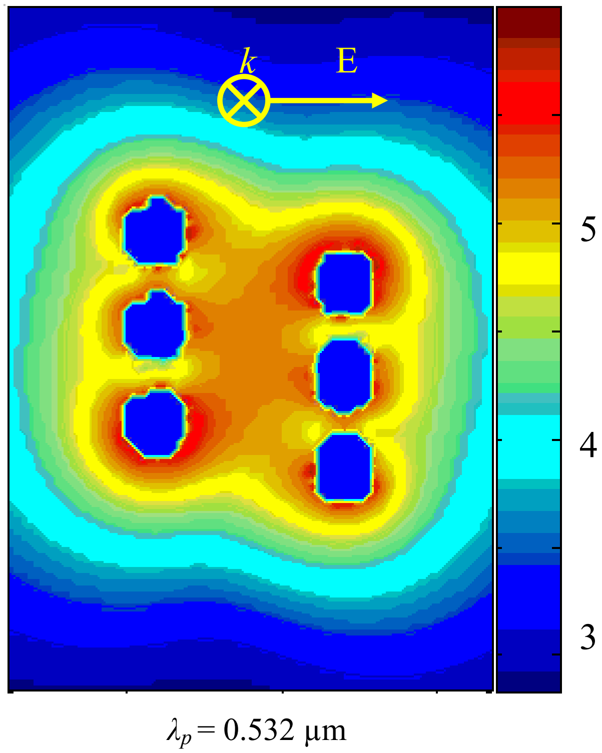

Figure 4.12 *E* field enhancement contours ($\log_{10}\gamma$) of helical nanostructures under TP incidence for helix with $h = 30$ nm and $\lambda_p = 0.532$ μm.

4.4.2 the *x*-axis and *y*-axis polarized incidence

For both XP and YP incidence, light propagates along the axis of the helix. Figure 4.13 shows the extinction spectra under XP incidence. In addition to the UV extinction peak at λ_{TM} = 0.34 μm, there is a strong plasmon peak appeared at λ_p ~ 0.538 – 0.616 μm for each spectrum. Compared to the spectra under TP incidence, there are no broad shoulders on the right side of the strong plasmon peak. For *h* = 24 nm helix, there is a narrow peak located at λ_p = 0.538 μm with a shoulder located around 0.63 μm. With the increase of the pitch height *h*, the strong plasmon peak red shifts to λ_p = 0.616 μm at *h* = 60 nm (Fig. 4.11) and the strong plasmon peak becomes broader. The FWHM of this plasmon peak increases from 100 nm at *h* = 24 nm to 170 nm at *h* = 60 nm. The YP incidence has the same *E* field direction as that of TP incidence, thus they have the same extinction spectra (Fig. 4.10).

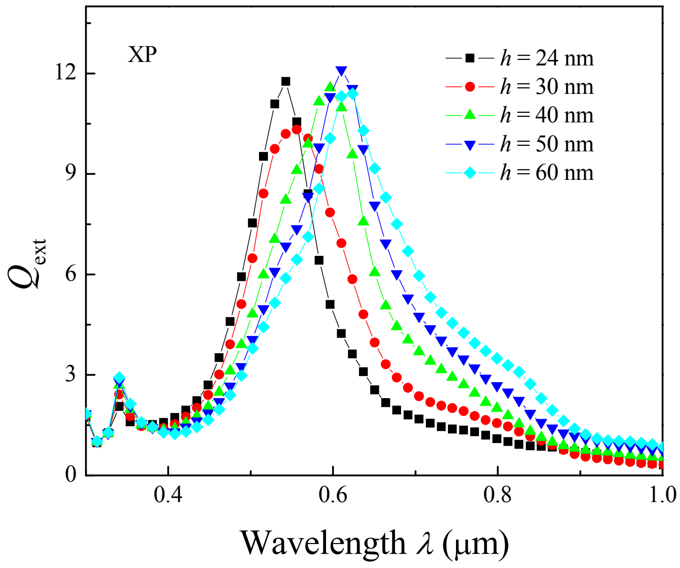

Figure 4.13 Pitch height dependent extinction spectra for Ag helical nanostructures under XP incidence.

As shown in Fig. 4.11, for the same helical structure, the resonant wavelength of the strong plasmon peak under the XP incidence is always larger than that under the YP incidence. When *h* increases from $h = 30$ nm to $h = 60$ nm, the extinction spectra under XP incidence are broader than those under YP incidence. For example, the FWHM of $h = 50$ nm helix under YP incidence is 100 nm and the FWHM under XP incidence is 150 nm. Under both XP and YP incident polarization, the *E* field enhancement distributions at the wavelength of the strong plasmon peak have a similar shape as those shown in Fig. 4.12, i.e., the distributions have the zigzag contour, and the maximum field enhancement is in the order of 10^6.

4.4.3 RHCP and LHCP incidences

Under RHCP incidence, there are two plasmon peaks appeared in the extinction spectra for helical nanostructures: one small peak located around $\lambda_{TM} = 0.34$ μm and one dominant plasmon peak located at $\lambda_p > 0.5$ μm, as shown in Fig. 4.14(a). When the pitch height increases from $h = 24$ nm to $h = 60$ nm, this main plasmon peak λ_p red shifts slightly from $\lambda_p = 0.531$ μm to $\lambda_p = 0.556$ μm, as shown in Fig. 4.11. However, under LHCP incidence, the plasmon peak λ_p changes dramatically with the pitch height *h*, as shown in Fig. 4.14(b). In this case, with the increase of the pitch height *h*, the main plasmon peak red shifts from $\lambda_p = 0.532$ μm at $h = 24$ nm to $\lambda_p = 0.618$ μm at $h = 60$ nm (Fig. 4.11). Also, on the right hand side of the main plasmon peak at λ_p, there is a broad shoulder in the extinction spectrum of helical nanostructures, which becomes more prominent with increasing *h*. For the helix with the same *h*, the plasmon peaks at λ_p under LHCP incidence are broader than those under RHCP incidence. For the $h = 50$ nm helix, the FWHM under RHCP incidence is 130 nm, while the FWHM under LHCP incidence is 210 nm. The difference between the plasmon peaks under LHCP and RHCP incidences also becomes larger with the increase in *h* as shown in Fig. 4.11.

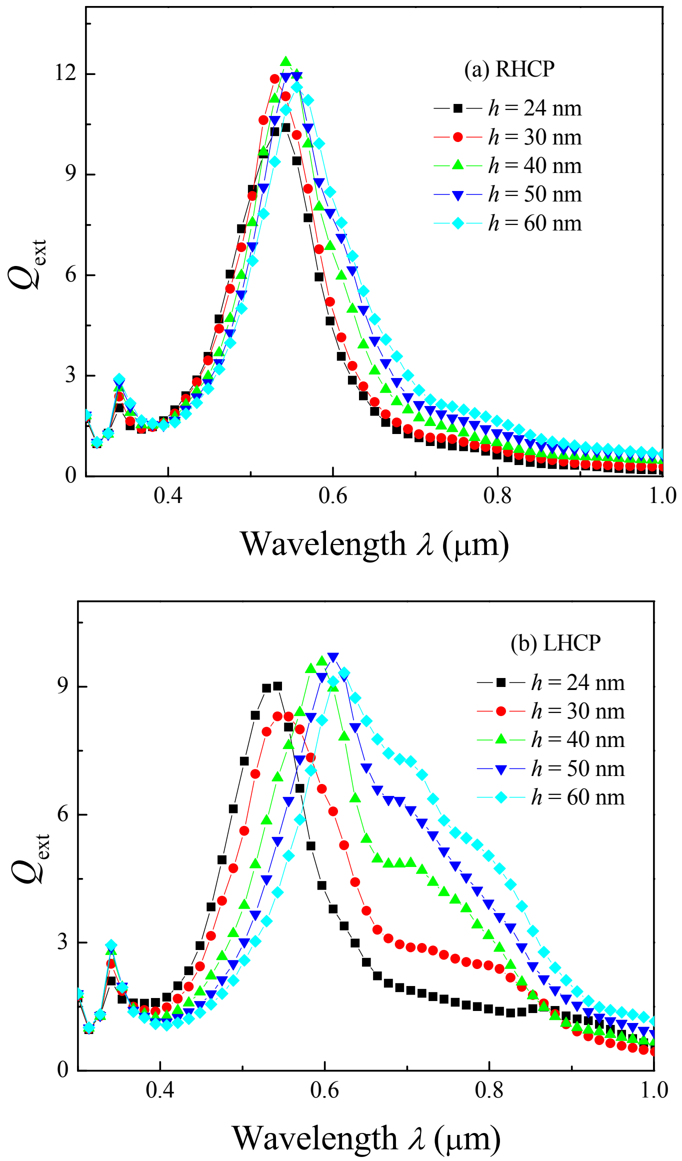

Figure 4.14 Pitch height dependent extinction spectra for Ag helical nanostructures under different polarization incidences: (a) RHCP (b) LHCP.

Figures 4.15(a) and (b) illustrate the *E* field enhancement distributions of the $h = 30$ nm helix at $\lambda_p = 0.535$ μm and $\lambda_p = 0.553$ μm under RHCP and LHCP incidence, respectively. Under

RHCP incidence, the maximum *E* fields also occur at the bottom of the helix. Between two adjacent pitches, strong field coupling occurs. Under LHCP incidence, the strong *E* fields not only congregate to the top of the helix but also are coupled inside the helix. In our calculation, the helix is a right-handed helical nanostructure. Therefore, when the nanostructures have the same helicity with incident polarized light, the maximum *E* field occurs at the bottom of the helix. When the nanostructures have the opposite helicity compared to the incident polarized light, the maximum *E* field occurs on the top of the helix.

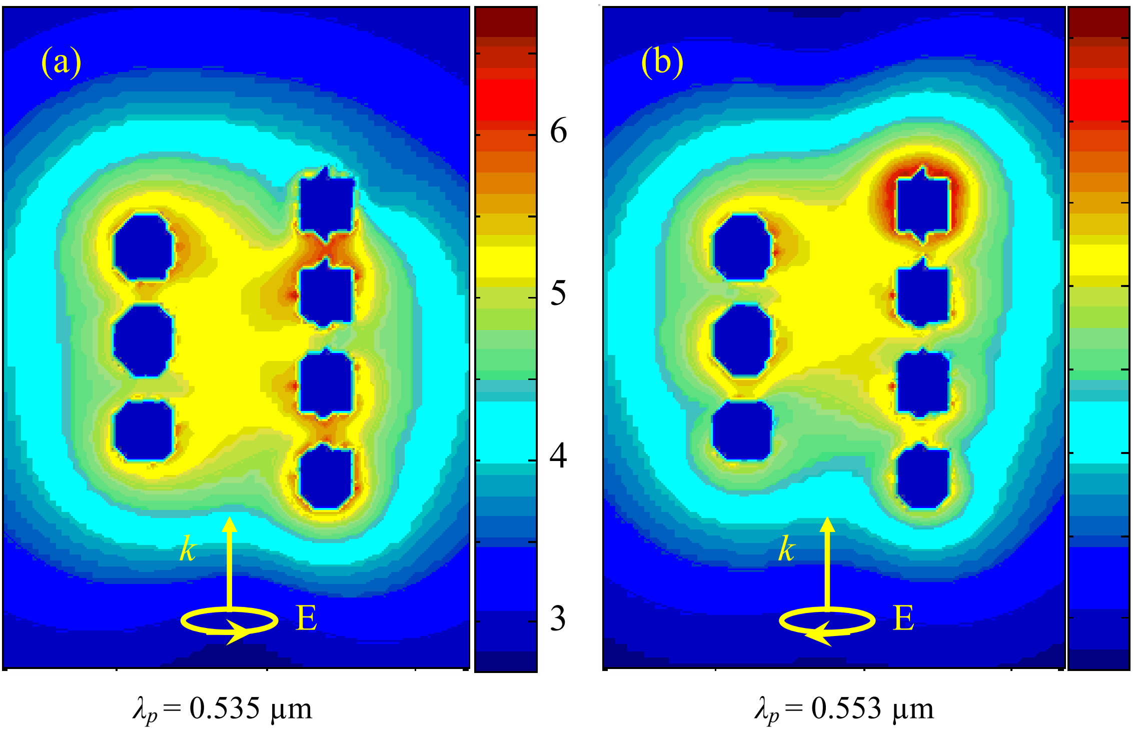

Figure 4.15 *E* field enhancement contours ($\log_{10}\gamma$) of the helix under different circular polarization and wavelength (a) RHCP and $\lambda_p = 0.535$ µm and (b) LHCP and $\lambda_p = 0.553$ µm for $h = 30$ nm.

4.4.4 Conclusion

It is found that the pitch height of the helix is a good parameter to tune the plasmon peak. When light propagates along the helix axis, the *E* field distribution of a helical nanostructure also depends on the incident polarization. For plane polarized incidence, a zigzag-shaped field distribution contour occurs in the helix. For helical structures, when the circularly polarized incidence is in the same direction as the helicity, the maximum *E* field occurs at the bottom of the helix. When the circular polarization direction is opposite to the helicity of the structure, the maximum *E* field occurs on the top of the helix. These results help us to understand the optical properties of helical nanostructures and engineer helical nanostructures in order to tune their plasmonics properties and rearrange the *E* field distribution.

4.5 Localized surface plasmon of Ag nano-helix structures

The collective oscillation of electrons within noble metal particles enables the resonant extinction of light at a particular wavelength, which is called surface plasmon resonance.[5] The surface plasmon resonances are strongly dependent on the topological shape of the metal particles.[15-17, 20, 113, 121, 138] For the particles with conventional shapes, such as spheres and cylinders, dipole plasmon peaks appear in the extinction spectra of the particles with smaller size. With the increase of the radius (for spheres) or the length (for cylinders), dipole plasmon peaks red shift linearly and higher order multiple modes appear at the blue side of the dipole mode.[15, 113] For the nano-helix, due to the complicated topologic shape, one can expect that there are some interesting plasmon modes.

It is quite clear that the plasmon modes in UV region are due to the electron oscillation perpendicular to the helix rod. However, the origins of the localized surface plasmon modes of the helical nanostructure in the visible wavelength region are not clear. In this section, we investigate the plasmon modes of the Ag helix in visible wavelengths under LHCP incidence. This study would help us understand the nature of the optical properties of the helix.

Right-handed helical nanostructures are used in the numerical calculation. Mathematically, the helix is defined by the following,

$$x = R\cos\varphi,\ y = R\sin\varphi,\ \text{and}\ z = h\varphi / 2\pi \tag{4.2}$$

where R is helix radius, h is the pitch height, φ is the helix azimuthal angle. The LHCP incidence is used in the calculation. The incident direction is along the axis of the helix (z-axis direction) from $\varphi = 0^{\circ}$ end to $\varphi = \varphi_{\mathrm{H}}$ end. The φ_{H} is used to describe the total height of the helix.

We first investigate how the helix height φ_{H} affect the plasmon peaks by fixing $R = 30$ nm, $h = 40$ nm, and cross section radius $r = 10$ nm. The total length φ_{H} of the helix varies from 4π to 8π with a $1/12\ \pi$ step. Figure 4.16(a) shows the extinction spectra of the helix under LHCP incidence with the total height of the helix from $\varphi_{\mathrm{H}} = 5.0\ \pi$ to $\varphi_{\mathrm{H}} = 6.0\ \pi$. In addition to the transverse plasmon peaks around 0.34 μm, two combined plasmon peaks locate around 0.55 μm ~ 0.75 μm which corresponding to the longitudinal mode (LM) of Ag nanospring. We use λ_{R} to denote longer wavelength peak and λ_{L} for the short wavelength peak. For the helix with $\varphi_{\mathrm{H}} = 5.0\ \pi$, the main plasmon peak locates at $\lambda_{\mathrm{R}} = 0.601$ μm and there is a weak shoulder located around $\lambda_{\mathrm{L}} = 0.538$ μm. With the increase of φ_{H}, both λ_{L} and λ_{R} red shift. However, the extinction coefficient $Q(\lambda_{\mathrm{R}})$ decreases while $Q(\lambda_{\mathrm{L}})$ increases. When φ_{H} reaches 5.67 π, the $Q(\lambda_{\mathrm{L}})$ is larger than $Q(\lambda_{\mathrm{R}})$ and becomes the dominate plasmon peak. When φ_{H} increases to 6.17 π (not show in Fig. 4.16 (a)), at the left side of the dominate plasmon peak one shoulder appears and becomes the new λ_{L} peak. With the increase of the total height, there is the similar behavior within a period of π.

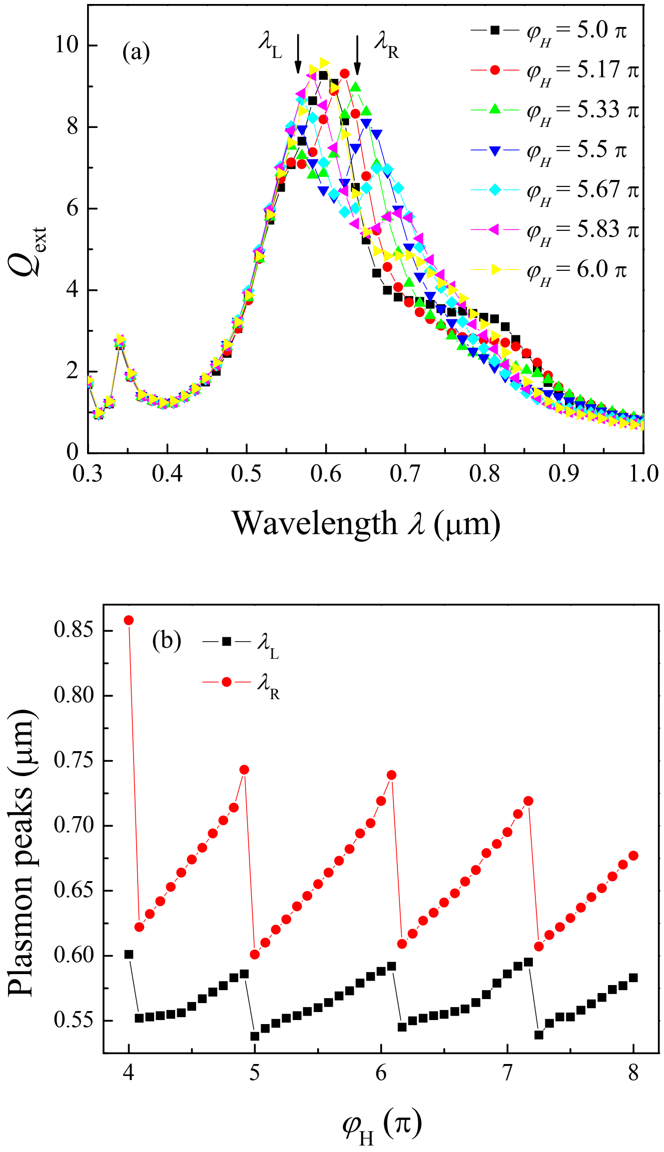

Figure 4.16 Under LHCP incidence: (a) Calculated extinction spectra of helical nanostructures with φ_H from 5.0 π to 6.0 π, and (b) plasmon peaks shift as a function of φ_H.

The change of λ_L and λ_R is plotted as a function of φ_H as shown in Fig. 4.16 (b). Both λ_L and λ_R red shift periodically with the increasing helix height with a period of π. The plasmon peaks of λ_R and λ_L switch at $\varphi_H \approx n \cdot \pi + 0.08\pi$, where n is an integer. This behavior is very different from other nanostructures. Usually, the plasmon peaks of the conventional shape structures red shift monotonically with the increase of the size of nanostructure. For a small sphere, the dipole plasmon wavelength red shifts with the increase of the radius.[66, 113] For triangular nanoprisms, the dipole surface plasmon resonance linearly red shift with the edge length.[21] For nanorod, LM plasmon peak red shifts linearly with the increase of the length or the aspect ratio.[120, 138] For the helix, if we define the effective aspect ratio, $L/2r$, where L is the total arc length of the helix, $L = l \cdot \varphi_H / 2\pi$, l is the arc length of one pitch, $l = \sqrt{(2\pi R)^2 + h^2}$, when the height is increased from $\varphi_H = 5.0\ \pi$ to $\varphi_H = 6.0\ \pi$, the effective aspect ratio is increased from 24 to 29. From the Gans theory, the extinction plasmon peak will red shift from ~ 3.5 μm to ~ 4.2 μm .[64] Therefore, the location and the change of the plasmon peaks of helix is much different from those predicted by Gans theory.

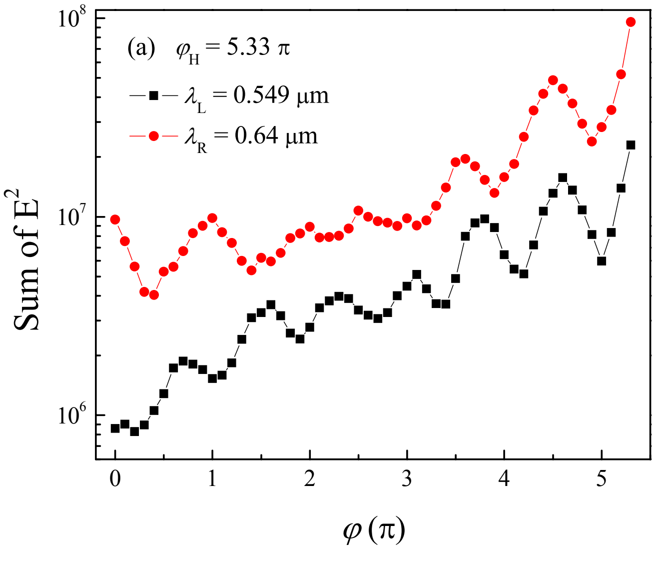

(b) Possible charge distribution for λ_L

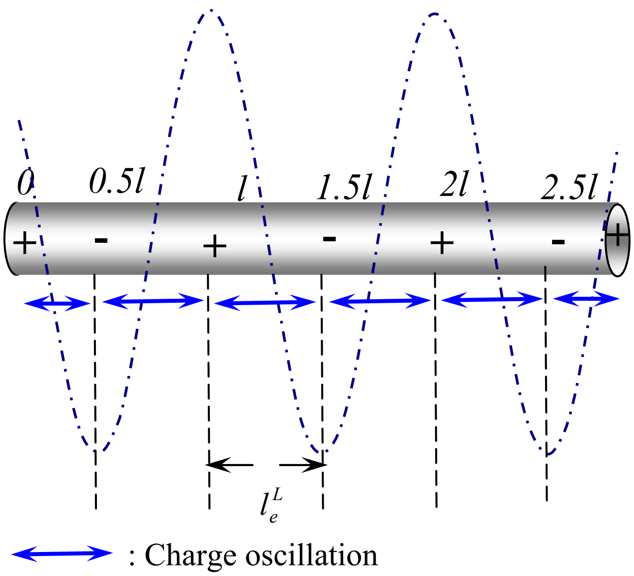

(c) Possible charge distribution for λ_R

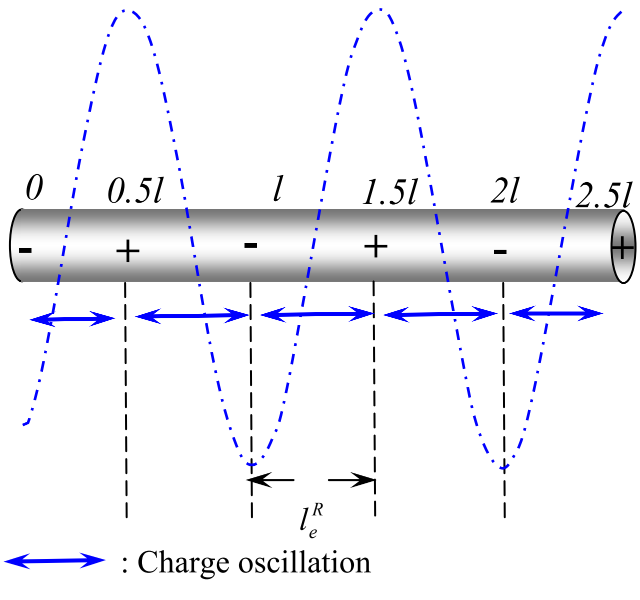

Figure 4.17 For $\varphi_H = 5.33\ \pi$ helix: (a) the sum of E^2 along the helix at λ_L and λ_R, and the sketches to show the possible charge distributions for different plasmon peaks: (b) λ_L and (c) λ_R.

In order to explore the nature of these two plasmon peaks, we have calculated the E field distribution around the nanorod (E^2, summation around the cross section form r = 13 nm to r = 15 nm) at different plasmon peaks (λ_L and λ_R) along the helix. Fig. 4.17(a) shows the field distribution for helix with $\varphi_H = 5.33\ \pi$. Although the amplitudes of the fields are different at two ends, the electric fields fluctuate periodically from one end to another end for both λ_L and λ_R. In addition, the fields at two ends of the helix are always maximums. For fields shown in Fig. 4.17(a), the field fluctuation for λ_L has 8 maximums and has 7 maximums for λ_R. We have investigated field distributions of other length helixes as well. In general, for λ_L, the number of the maximum field is $N_L = \text{int}(\varphi_H / \pi) + 2$, where int means taking the integer, and for λ_R, $N_R = \text{int}(\varphi_H / \pi) + 1$. These maximum field nodes result from maximum positive or negative surface charge congregation. If we pull the helix to a straight nanorod, we can sketch the possible charge distributions at the steady state along the helix to illustrate the electron oscillations. For the particular $\varphi_H = 5.33\ \pi$, $N_L = 7$ and $N_R = 6$. For λ_L case as shown in Fig. 4.17(b), the two ends of the helix have a maximum positive (negative) charge density distribution. And along thee helix, there are 2 maximum positive (negative) charge distribution and 3 maximum negative (positive) charge distributions. All the positive and negative charge distribution locations contribute to the E field maximum ($|E|^2 \propto |\frac{\sigma}{\varepsilon_0}|^2$, where σ is the surface charge density). Thus, the maximum positive and negative charge distributions in Fig. 4.17(b) correspond to 7 E field $|E|^2$ maximums. If we pair the positive charge maximum and negative charge maximum together to be an effective dipole, as illustrated in Fig. 4.17(b), the number of the effective dipoles oscillating along the helix is 6, or $N_L - 1$. For λ_R case, the two ends of the helix have opposite charge as shown in Fig. 4.17(c), and it corresponds to 5 effective dipoles, or $N_\mathrm{R} - 1$ dipoles. Therefore, we can define an effective dipole length l_e^L for λ_L and l_e^R for λ_R,

$$l_e^L = L/(N_L - 1) \text{ and } l_e^R = L/(N_R - 1)\,. \tag{4.3}$$

The effective dipole length shall determine the plasmon mode wavelength. According to the Gans theory, the longer the effective dipole length, the larger the plasmon wavelength is. Because $N_\mathrm{L} > N_\mathrm{R}$, $l_e^R > l_e^L$, thus, $\lambda_\mathrm{R} > \lambda_\mathrm{L}$, which is consistent with the red shift plasmon peak with the increasing length of the dipole oscillation.[64] Since N_L and N_R increase stepwise, it is expected that l_e^L and l_e^R change periodically with φ_H as well. This is coincident with the change of the plasmon wavelength. Thus, we can replot Fig. 4.16(b) as the plasmon wavelength versus the corresponding effective dipole length, as shown in Fig. 4.18. For both λ_L and λ_R, all data collapse together for different φ_H, and one can also see that λ_L vs. l_e^L, and λ_R vs. l_e^R follow a linear relationship with a slope of 2.3×10^{-3} and 6.4×10^{-3}. Such a behavior is similar to the longitudinal plasmon mode for the cylindrical nanorods[138]: For the cylindrical nanorods with fixed diameter, the LM plasmon peaks red shift linearly with the length of the nanorod, and the effective dipole length corresponds to the length of cylindrical nanorod. Thus, the plasmon mode of a helical nanostructure is determined by the effective dipole length. Due to the periodic structure of the helix, the effective dipole length is determined by the half arc length of the helix.

To further investigate whether the plasmon modes are really caused by the effective dipole length, we also varied the radius R and the pitch height h of the helix for $\varphi_\mathrm{H} = 5.33\ \pi$. The helix radius R is increased from $R = 24$ nm to $R = 40$ nm with fixed $h = 48$ nm and $r = 10$ nm. With the increase of the helix radius R, both λ_L and λ_R red shift with the increasing extinction coefficients. However, the λ_R red shift more dramatically compared to λ_L. The pitch height h is increased from $h = 24$ nm to $h = 60$ nm with fixed $R = 30$ nm and $r = 10$ nm. Both λ_L and λ_R red shift linearly with the pitch height. We also plot the plasmon wavelength λ_L and λ_R versus the effective dipole length in Fig. 4.18, and for both cases the λ_L (λ_R) changes linearly with l_e^L (l_e^R), which is consistent with our speculation. However, the slope of the changes is different. When R is changing, the slope for λ_R versus l_e^R is 3.1×10^{-3}, and 2.8×10^{-3} for λ_L versus l_e^L. When h is changing, these two slopes become 3.3×10^{-3} and 1.1×10^{-2}. We can see that for λ_L at h dependent case, the slope is the largest, while for λ_R at R dependent case, the slope is smallest. The largest slope for λ_L at h dependent illustrates that the λ_L is more sensitive to the coupling between adjacent cross sections. The similar slopes for λ_R at R and h dependent cases demonstrate that λ_R are mainly due to the charge oscillations along the helix, which is less sensitive to the coupling between adjacent cross sections.

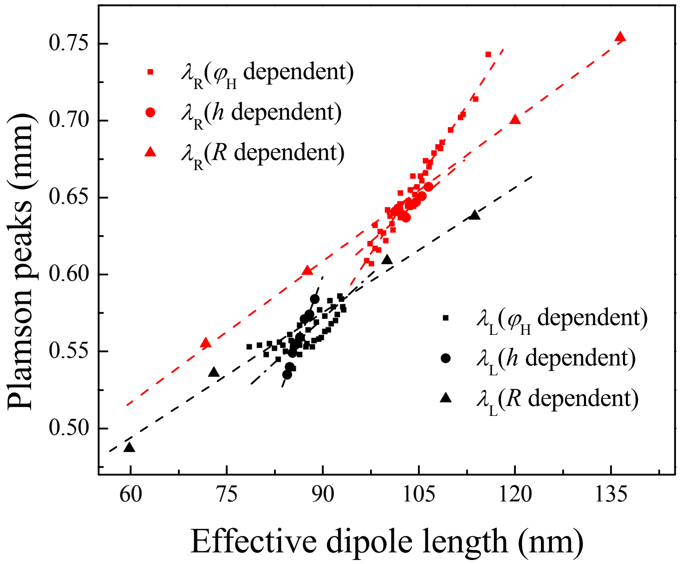

Figure 4.18 The plasmon peaks as a function of the effective dipole length for the height dependent, pitch height dependent, and helix radius dependent cases. The dash lines are used to guide eyes.

In conclusion, two LM plasmon modes are found in the extinction spectra of the nano-helix, they all red shift periodically with the increase of the helix height. They also red shift with the helix radius and the pitch height. These plasmon modes are resulted from the effective dipole oscillations along the arc length of the helix and are mainly determined by the effective dipole length, which is about the size of the half of the arc length of one pitch. The addition of an extra period in the helix will not significantly change the effective dipole length due to the symmetry and periodic structure of the helix, but just add additional effective dipoles into the structure. Therefore, the effective absorbance or extinction coefficient at those plasmon wavelengths can not be significantly increased. This property may be used to design better plasmonics nanostructure for tumor treatment or imaging biomarker.

4.6. Conclusions

Because of its complicated topological shape, the optical properties of a helical Ag nanostructure are strongly dependent on the incident polarizations. When light propagates perpendicular to the helix with the polarization along the helix, two transverse plasmon modes are excited in the UV region. At those plasmon wavelengths, the stronger *E* fields occur around the side surface of the helix and are coupled into the space between two adjacent pitches. When the incident polarization is changed to be perpendicular to the axis, multiple plasmon peaks appear in the extinction spectra. At the plasmon wavelengths, the maximum *E* fields occur around the surface of the helix, and there are strong coupling in the helix and form a zigzag field distribution inside the helix. When the incident light propagates along the helix axis, in addition to the transverse plasmon modes in the UV region, strong extinction peaks appear at the visible region. For the right-handed helical nanostructures, the main plasmon peaks under left-handed circular polarization (LHCP) incidence red shift in plasmon peak wavelength compared to those under right-handed circular polarization (RHCP) incidence. Under LHCP incidence, the maximum *E* fields occur at the exit end and excitation light propagates along the helix, while under RHCP incidence, the maximum *E* fields occur at the entry end of the helix. The *E* field distribution of the helical nanostructure under circularly polarized incidence could also help to spatially resolve the analyte's location in a sub-micrometer length scale.

In addition to the incident polarizations, the structural parameters, such as the total height, the pitch height, and the helix radius, can also be used to tune the plasmon peaks. The two LM mode plasmon peaks red shift periodically with the height and red shift linearly with the pitch height and the helix radius. These two plasmon modes are due to the dipole oscillations along the arc length of the helix and are determined by effective dipole length. Understanding the origins of the plasmon peaks would help us to design helical nanostructures for specific purpose, such as the tumor treatment and the imaging biomarker.

CHAPTER 5

CONCLUSIONS AND FUTURE WORK

In this dissertation, I have used the discrete dipole approximation method to study the optical properties of the Ag nanostructures with different topologic shapes. It is shown that the topologic shapes of the nanostructures have significant effects on the optical properties, and provides an alternative way to tune the plasmonic characteristics of metal nanorods.

When the nanostructures become complicated, plasmon peaks are strongly polarization dependent. For a cylindrical nanorod, the longitudinal mode plasmon peak appears when the incident polarization is located along the long axis and the transverse mode plasmon peak appears when the incident polarization is located perpendicular to the long axis. For more complicated nanostructures, such as a Y-shaped nanorod, the plasmon peaks can be tuned by changing the incident polarization angle. The plasmon peaks can also be tuned by changing the structural parameters. When the nanostructures become more complicated, there are more parameters that can be used to tune the plasmon peaks. At the plasmon wavelengths, enhanced electric fields occur at the surface. It is found that more hot spots are observed for nanostructures with more defects, such as the period-shaped nanorods, L- and Y-shaped nanorods. This would help us to understand the optical properties and field enhancement of irregular nanorod structures.

Other nanostructures also show unique optical properties and will be the potential choices for specific purpose. For the U-shaped nanorod, because the bottom nanorod builds a path for the electron oscillations, longitudinal mode plasmon oscillations can also occur along the vertical nanorods and there are larger hot spots with much larger electric field compared to the parallel-nanorod structure. Therefore, the rod-film substrates would produce larger SERS enhancement compared to the rod substrates. For the helical nanostructures, the spatial distribution of the maximum electric field can be adjusted by changing the polarization directions of the incident light, especially the circular polarizations. The maximum electric fields distribute at the bottom or on the top of helix, which depends on the incident circular polarizations. Thus, helical nanostructures provide a simple way to spatially distinguish the analyte's location in the helix. In fact, it can be used to resolve the spatial distribution of the analyte in the submicrometer length scale.

However DDA method can be only easily applied to single nanoparticle. Although optical properties of single nanostructure can also shine some light on the optical properties of the array substrate, in the future, the coupling effect should be considered and optical properties of the array can be calculated by the finite difference time domain (FDTD) method. The multilayer with different shapes would also provide interesting optical properties.

For the helical nanostructure, the longitudinal mode plasmon peaks are due to the effective dipole oscillation along the arc length of the helix and are mainly determined by the effective dipole length. Increasing the pitch number slightly changes the plasmon peak. However, the number of the effective dipole oscillations will be increased, which will benefit the absorption of the helix. This property may be used to design better plasmonic nanostructures for tumor treatment or imaging biomarkers. Therefore, investigating the absorption efficiency of the helical nanostructure would be interesting.

REFERENCES

1. Palik, E.D., *Handbook of Optical Constants of Solids*. 1985, New York: Academic.
2. Johnson, P.B. and R.W. Christy, Phys. Rev. B, 1972. **6**: p. 4370.
3. Faraday, M., Philos. Trans. R. Soc. Lond., 1857. **147**: p. 145.
4. Mie, G., Ann. Phys., 1908. **25**: p. 329.
5. Kreibig, U. and M. Vollmer, *Optical Properties of Metal Clusters*. 1995, Berlin: Springer.
6. Kerker, M., *The Scattering of Light and Other Electromagnetic Radiation*. 1969, New York: Academic.
7. Bohren, C.F. and D.R. Huffman, *Absorption and Scattering of Light by Small Particles*. 1983, New York: Wiley.
8. Vo-Dinh, T., Trac. Trends Anal. Chem., 1998. **17**: p. 557.
9. Tian, Z.Q., B. Ren, and D.Y. Wu, J. Phys. Chem. B, 2002. **106**: p. 9463.
10. Campion, A. and P. Kambhampati, Chem. Soc. Rev., 1998. **27**: p. 241.
11. Su, K.H., Q.H. Wei, and X. Zhang, Appl. Phys. Lett., 2006. **88**: p. 063118.
12. Prodan, E., P. Nordlander, and N.J. Halas, Nano Lett., 2003. **3**: p. 1411.
13. Mock, J.J., et al., Nano Lett., 2002. **2**: p. 465.
14. Wei, Q.-H., et al., Proceedings of SPIE 2003. **5221**: p. 92.
15. Payne, E.K., et al., J. Phys. Chem. B, 2006. **110**: p. 2150.
16. Kim, F., J.H. Song, and P. Yang, J. Am. Chem. Soc., 2002. **124**: p. 14316.
17. Chen, S., Z. Fan, and D.L. Carroll, J. Phys. Chem. B, 2002. **106**: p. 10777.

18. Hao, E., et al., J. Am. Chem. Soc., 2002. **124**: p. 15182.

19. Jin, R., et al., Science, 2001. **294**: p. 1901.

20. Wiley, B.J., et al., J. Phys. Chem. B, 2006. **110**: p. 15666.

21. Shuford, K.L., M.A. Ratner, and G.C. Schatz, J. Chem. Phys., 2005. **123**: p. 114713.

22. Hao, E., G.C. Schatz, and J.T. Hupp, J. Fluorescence, 2004. **14**: p. 331.

23. Kottmann, J.P., et al., Optics Express, 2000. **6**: p. 213.

24. Chen, S., et al., J. Nanosci. Nanotech., 2004. **4**: p. 254.

25. Jin, R., et al., nature, 2003. **425**: p. 487.

26. Zhu, J., et al., Materials Science and Engineering B, 2005. **121**: p. 199.

27. Noguez, C., Optical Materials, 2004. **27**: p. 1204.

28. Orfanides, P., et al., Am. J. Phys., 2000. **68**: p. 936.

29. Xu, G., et al., Appl. Phys. Lett., 2003. **82**: p. 3811.

30. Mock, J.J., D.R. Smith, and S. Schultz, Nano Lett., 2003. **3**: p. 485.

31. Harfenist, S.A., et al., Adv. Mater., 1997. **9**: p. 817.

32. Zhao, L., K.L. Kelly, and G.C. Schatz, J. Phys. Chem. B, 2003. **107**: p. 7343.

33. Su, K.-H., et al., Nano Lett., 2003. **3**: p. 1087.

34. Etchegoin, P., et al., Chem. Phys. Lett., 2003. **383**: p. 577.

35. Kalele, S.A., et al., J. Nanophotonics, 2007. **1**: p. 012501.

36. Andersen, P.C. and K.L. Rowlen, Appl. Spectrosc., 2002. **56**: p. 124.

37. Maier, S.A., et al., Adv. Mater., 2001. **13**: p. 1501.

38. Barnes, W.L., A. Dereux, and T.W. Ebbesen, Nature, 2003. **424**: p. 824.

39. Lamprecht, B., et al., Appl. Phys. Lett., 2001. **79**: p. 51.

40. Devaux, E., et al., Appl. Phys. Lett., 2003. **83**: p. 4936.

41. Dickson, R.M. and L.A. Lyon, J. Phys. Chem. B, 2000. **104**: p. 6095.

42. Maier, S.A., et al., Nat. Mater., 2003. **2**: p. 229.

43. Hecht, B., et al., J. Chem. Phys., 2000. **112**: p. 7761.

44. Larsen, R.E. and H. Metiu, J. Chem. Phys., 2001. **114**: p. 6851.

45. Degiron, A. and T.W. Ebbesen, J. Opt. A: Pure Appl. Opt., 2005. **7**: p. 90.

46. Mirkin, C.A., et al., Nature, 1996. **382**: p. 607.

47. Reynolds, R.A., C.A. Mirkin, and R.L. Letsinger, J. Am. Chem. Soc., 2000. **122**: p. 3795.

48. Elghanian, R., et al., Science, 1997. **277**: p. 1078.

49. Osawa, M., Bull. Chem. Soc. Jpn., 1997. **70**: p. 2861.

50. Link, S. and M.A. El-Sayed, Annu. Rev. Phys. Chem., 2003. **54**: p. 331.

51. Levi, S.A., et al., Chem. Eur. J., 2002. **8**: p. 3808.

52. Calander, N., Anal. Chem., 2004. **76**: p. 2168.

53. Ekgasit, S., et al., Anal. Chem., 2004. **76**: p. 2210.

54. Pendry, J.B., et al., Phys. Rev. Lett., 1996. **76**: p. 4773.

55. Pendry, J.B., et al., J. Phys. : Condens. Matter, 1998. **10**: p. 4785.

56. Smith, D.R., et al., Phys. Rev. Lett., 2000. **84**: p. 4148.

57. Shelby, R.A., D.R. Smith, and S. Schultz, Science, 2001. **292**: p. 77.

58. McCall, M.W., A. Lakhtzkia, and W.S. Weiglhofer, Eur. J. Phys., 2002. **23**: p. 353.

59. Veselago, V.G., Sov. Phys. Usp., 1968. **10**: p. 509.

60. Ramakrishna, S.A., Rep. Progr. Phys. , 2005. **68**: p. 449.

61. Pendry, J.B., Contemp. Phys., 2004. **45**: p. 191.

62. Gans, R., Ann. Physik, 1915. **47**: p. 270.

63. Papavassiliu, G.C., Prog. Solid state Chem., 1979. **12**: p. 185.

64. Link, S., M.B. Mohamed, and M.A. El-Sayed, J. Phys. Chem. B, 1999. **103**: p. 3073.

65. Draine, B.T. and P.J. Flatau, J. Opt. Soc. Am. A, 1994. **11**: p. 1491.

66. Jensen, T.R., et al., J. Phys. Chem. B, 1999. **103**: p. 9846.

67. Purcell, E.M. and C.R. Pennypacker, Astrophys. J., 1973. **196**: p. 705.

68. Flatau, P.J., G.L. Stephens, and B.T. Draine, J. Opt. Soc. Am. A, 1990. **7**: p. 593.

69. Draine, B.T. and P.J. Flatau, J. Opt. Soc. Am. A, 1993. **11**: p. 1491.

70. Laczik, Z., Appl. Opt., 1996. **35**: p. 3736.

71. Draine, B.T., Astrophysical Journal, 1988. **333**: p. 848.

72. Chiappetta, P., J. Phys. A, 1980. **13**: p. 2101.

73. Novotny, L., D.W. Pohl, and B. Hecht, Opt. Lett., 1995. **20**: p. 970.

74. Moreno, E., et al., J. Opt. Soc. Am. A, 2002. **19**: p. 101.

75. Hafner, C. and L. Bomholt, *The 3D electrodynamic wave simulator (including the 3D MMP source core)*. 1993, Chichester: Wiley.

76. Taflove, A. and M.E. Brodwin, IEEE Transactions: Microwave Theory and Techniques, 1975. **23**: p. 623.

77. Taflove, A., *Computational Electrodynamics: The Finite Difference Time-Domain Method*. 1995, Norwood, MA: Artech House.

78. Yee, S.K., IEEE Trans. Antennas Propag., 1966. **14**: p. 302.

79. Umashankar, K. and A. Taflove, IEEE Trans. Electromagn. Compat., 1982. **24**: p. 397.

80. Kunz, K.S. and R.J. Luebbers, *The Finite Difference Method for Electromagnetic*. 1993, Boca Raton, FLa.: CRC.

81. Mur, G., IEEE Trans. Electromagn. Compat., 1982. **23**: p. 377.

82. Quinten, M. and U. Kreibig, Appl. Opt., 1993. **32**: p. 6173.

83. Borghese, F., et al., Appl. Opt., 1979. **18**: p. 116.

84. Bruning, J.H. and Y.U. Lo, IEEE Trans. Antennas Propag., 1971. **19**: p. 378.

85. Fuller, K.A. and G.W. Kattawar, Opt. Lett., 1988. **13**: p. 90.

86. Hamid, A.K., J. Electromagn. Waves Appl., 1996. **10**: p. 723.

87. Mackowski, D.W., J. Opt. Soc. Am. A, 1994. **11**: p. 2851.

88. Waterman, P.C., Phys. Rev. D, 1971. **109**: p. 16.

89. Mishchenko, M.I., D.W. Mackowski, and L.D. Travis, Appl. Opt., 1995. **34**: p. 4589.

90. Mackowski, D.W., J. Quant. Spectrosc. Radiat. Transfer, 2001. **70**: p. 441.

91. Hao, E. and G.C. Schatz, J. Chem. Phys., 2004. **120**: p. 357.

92. Press, W.H., et al., *Numerical Recipes*. 1986, Cambridge: Cambridge University

93. Petravic, M. and G. Kuo-Petravic, J. Computational Phys., 1979. **32**: p. 263.

94. Draine, B.T. and J. Goodman, Astrophys. J., 1993. **405**: p. 685.

95. Vaidya, D.B., et al., Astronomy and Astrophysics, 2001. **375**: p. 584.

96. Kimura, H. and I. Mann, J. Quantitative Spectroscopy & Radiative Transfer, 2004. **89**: p. 155.

97. Saija, R., et al., Appl. Opt., 2001. **40**: p. 5337.

98. He, J., et al., J. Opt. Soc. Am. A, 2004. **21**: p. 1953.

99. Zong, R.-L., et al., J. Phys. Chem. B, 2004. **108**: p. 16716.

100. Felidj, N., J. Aubard, and G. Levi, J. Chem. Phys., 1999. **111**: p. 1195.

101. Jensen, T., et al., J. Cluster Science, 1999. **10**: p. 295.

102. Yang, W.-H., G.C. Schatz, and R.P.V. Duyne, J. Chem. Phys., 1995. **103**: p. 869.

103. Flatau, P.J., Opt. Lett., 1997. **22**: p. 1205.

104. Draine, B.T. and P.J. Flatau, *User guide to the discrete dipole approximation code DDSCAT 6.1*: San Diego, CA.

105. Tao, A., et al., Nano Lett., 2003. **3**: p. 1229.

106. Chaney, S.B., et al., Appl. Phys. Lett., 2005. **87**: p. 031908.

107. Zhao, Y.-P., et al., J. Phys. Chem. B, 2006. **110**: p. 3153.

108. Tao, A.R. and P. Yang, J. Phys. Chem. B, 2005. **109**: p. 15687.

109. Tao, A.R. and P. Yang, J. Phys. Chem., 2005. **109**: p. 15687.

110. Shanmukh, S., et al., Nano Lett., 2006. **6**: p. 2630.

111. Driskell, J.D., et al., J. Phys. Chem. C, 2008. **112**: p. 895.

112. Chu, H.Y., et al., Optics Express, 2007. **15**: p. 12230.

113. Kelly, K.L., et al., J. Phys. Chem. B, 2003. **107**: p. 668.

114. Sosa, I.O., C. Noguez, and R.G. Barrera, J. Phys. Chem. B, 2003. **107**: p. 6269.

115. Meier, M. and A. Wokaun, Opt. Lett., 1983. **8**: p. 581.

116. Shtrichman, I., et al., Phys. Rev. B, 2001. **65**: p. 035310.

117. Wokaun, A., J.P. Gordon, and P.F. Liao, Phys. Rev. Lett., 1982. **48**: p. 957.

118. Hulst, H.C.v.d., *Light scattering by small particles* Vol. Dover Publications, Inc. 1981, New York: Dover.

119. Jackson, J.D., *Classical Electrodynamics*. 1998, New York: John Wiley & Sons.

120. Krenn, J.R., et al., Appl. Phys. Lett., 2000. **77**: p. 3379.

121. Hao, F., et al., Nano Lett., 2007. **7**: p. 729.

122. Bloemer, M.J., et al., Phys. Rev. B, 1988. **37**: p. 8015.

123. Smith, G.B., Appl. Opt., 1990. **29**: p. 3685.

124. Robbie, K. and M.J. Brett, J. Vac. Sci. Technol. A, 1997. **15**: p. 1460.

125. Robbie, K., J.C. Sit, and M.J. Brett, J. Vac. Sci. Technol. B, 1998. **16**: p. 1115.

126. Zhao, Y.-P., et al., Int. J. Nanosci., 2002. **1**: p. 87.

127. Tabunshchyk, K.V., et al., J. Phys. D: Appl. Phys., 2007. **40**: p. 4936.

128. He, Y.-P., J.-S. Wu, and Y.-P. Zhao, Nano Lett., 2007. **7**: p. 1369.

129. Chaney, S.B., Z.-Y. Zhang, and Y.-P. Zhao, Appl. Phys. Lett., 2006. **89**: p. 053117.

130. Sorge, J.B., et al., Optics Express, 2006. **14**: p. 10550.

131. Williams, R., J. Phys. Chem. , 1963. **39**: p. 382.

132. Heimeier, G.H. and L.A. Zanoni, Appl. Phys. Lett., 1968. **13**: p. 91.

133. Young, N.O. and J. Kowal, Nature, 1959. **183**: p. 104.

134. Motohiro, T. and Y. Taga, Appl. Opt., 1989. **28**: p. 2466.

135. Azzam, R., Appl. Phys. Lett., 1992. **61**: p. 3118.

136. Popta, A.C.v., J.C. Sit, and M.J. Brett, Appl. Opt., 2004. **43**: p. 3632.

137. Steele, J.J. and M.J. Brett, J. Mater. Sci.: Mater. Electron, 2007. **18**: p. 367.

138. Zhang, Z.-Y. and Y.-P. Zhao, J. Appl. Phys., 2007. **102**: p. 113308.

APPENDICES

A. Calculate the near-field *E* field using DDSCAT 6.1

1. Output the polarizations of each dipole

The calculated polarizations of all the dipoles are stored in CXPOL, which has two formats. One is the original and another format is the extend format. For the original format, CXPOL(NAT3) stores polarizations and IXYZ(NAT0, 3) stores the position of the dipole, where NAT0 is the number of the dipoles and NAT3 = 3*NAT0. For the extend format, CXPOL is extended to one cubic CXPOL(X, Y, Z, 3). At the same time IOCC(X, Y, Z, 3) is used to show whether there is material with some special dielectric constants.

The file extend.f is used to extend CXPOL. At the beginning, all the data are read in the original way. After they call the function of extend.f, CXPOL is changed to be the extend format. In the file of getfml.f, after they call the function of reduce, CXPOL is changed back to the original format. For the positions of the dipoles, after extend is called, original positions are shifted to new position. The minimums of X, Y, Z are 1. This kind shift is done in the file of extend.f.

In order to output the polarizations of all dipoles, the following sentences are inserted in the file of getfml.f after the sentence of

“CALL REDUCE(CXPOL,IOCC,MXN3,MXNAT,NAT,NAT0)”,

```
CCCCCCCCCCCCCCCCCCCCCCCCCCCCCCC
CC OUTPUT THE POSITION OF DIPOLES:
      OPEN(UNIT=921,FILE="POSITION.TXT")
      DO Q=1,NAT0
      WRITE(921,*) IXYZ0(Q,1),IXYZ0(Q,2),IXYZ0(Q,3)
      END DO
```

```
CLOSE(921)

CC OUTPUT THE POLARIZATIONS OF ALL DIPOLES
      OPEN(UNIT=922,FILE="polarizationxxx.TXT")
      OPEN(UNIT=923,FILE="polarizationyyy.TXT")
      OPEN(UNIT=924,FILE="polarizationzzz.TXT")
      DO Q=1,NAT0
      WRITE(922,*) REAL(CXPOL(Q)),AIMAG(CXPOL(Q))
      WRITE(923,*) REAL(CXPOL(Q+NAT0)),AIMAG(CXPOL(Q+NAT0))
      WRITE(924,*) REAL(CXPOL(Q+2*NAT0)),AIMAG(CXPOL(Q+2*NAT0))
      END DO
      CLOSE(922)
      CLOSE(923)
      CLOSE(924)

CC OUTPUT THE PARAMETERS
      OPEN(UNIT=955,FILE="PARAMETER.TXT")
      WRITE(955,*) 'NAT=',NAT
      WRITE(955,*) 'NAT0=',NAT0
      WRITE(955,*) 'NAT3=',NAT3
      WRITE(955,*) 'MXN3=',MXN3
      WRITE(955,*) 'MXNX=',MXNX
      WRITE(955,*) 'MXNY=',MXNY
      WRITE(955,*) 'MXNZ=',MXNZ
      WRITE(955,*) 'NAT03=',NAT03
      WRITE(955,*) 'MXNAT=',MXNAT
      CLOSE(955)

CCCCCCCCCCCCCCCCCCCCCCCCCCCCCCCCCCCCCCCCCCCCCCCCCCCCCCCCCCCCCCCCCCCCC
```

2. Calculate the *E* field using the polarizations

The *E* field is the sum of *E* field produced by each dipole.

$$\vec{E}_{dipole} = \frac{e^{ikr}}{r^3}\left\{k^2\vec{r}\times(\vec{r}\times\vec{P}) + \frac{(1-ikr)}{r^2}[\vec{r}^{\,2}\vec{P} - 3\vec{r}(\vec{r}\cdot\vec{P})]\right\}$$

where $\vec{r}$ is the position of the dipole to the point to calculate the *E* field, $\vec{P}$ is the polarization, and *k* is wave number of incident wavelength.

The following program is used to calculate the *E* field at the *xy*-plane with the middle of *z*.

```
program EFIELD

      implicit none

      INTEGER XNPOINTS,YNPOINTS,J,K,M,N,NAT
      REAL MAXXD,MINXD,MAXYD,MINYD,MAXZD,MINZD
      INTEGER NSURFACE0,NSURFACE,YROUND
      REAL XMIDLE,YMIDLE
      INTEGER ZMIDLE
```

```
        REAL DISTANCE0,DISTANCE

        ALLOCATABLE XD(:),YD(:),ZD(:),XXD(:),YYD(:)
        ALLOCATABLE PX(:),PY(:),PZ(:)
        ALLOCATABLE EX(:,:),EY(:,:),EZ(:,:),ESQUARE(:,:),SHOW(:,:)
        ALLOCATABLE X(:),Y(:)

        REAL XD,YD,ZD,XXD,YYD
        COMPLEX PX,PY,PZ
        COMPLEX EX,EY,EZ
        REAL ESQUARE,SHOW
        REAL X,Y
        REAL REALPX,IMAGPX,REALPY,IMAGPY,REALPZ,IMAGPZ


        COMPLEX PN
        REAL NDATA,NX,NY,NZ

        COMPLEX EXADDFAR,EYADDFAR,EZADDFAR,FACTOR,EXADD,EYADD,EZADD
        REAL Z,DIEL0,DIEL,AIR,CONSTANT,D0,D,DELTA,WAVELENGTH0,WAVELENGTH,ZROUND
        INTEGER IDPAR,IDPOS,IDPOLXXX,IDPOLYYY,IDPOLZZZ
        CHARACTER*30 PARFILE,POSFILE,POLXXX,POLYYY,POLZZZ
        INTEGER IDX,IDZ,IDESQUARE,IDSHOW
        CHARACTER*30 XPLANE,YPLANE,ESQUAREFILE,ESHOW

        IDPAR=1
        IDPOS=2
        IDPOLXXX=3
        IDPOLYYY=4
        IDPOLZZZ=5
        PARFILE='PARAMETER.TXT'
        POSFILE='POSITION.TXT'
        POLXXX='POLARIZATIONXXX.TXT'
        POLYYY='POLARIZATIONYYY.TXT'
        POLZZZ='POLARIZATIONZZZ.TXT'

        IDX=51
        IDZ=52
        IDESQUARE=53
        IDSHOW=54
        XPLANE='XPLANEXXXYYY.TXT'
        YPLANE='YPLANEXXXYYY.TXT'
        ESQUAREFILE='ESQUAREXXXYYY.TXT'
        ESHOW='ESHOWXXXYYY.TXT'
!*************************************************************
        OPEN(UNIT=IDPAR,FILE=PARFILE,STATUS='OLD',FORM='FORMATTED')
        READ(IDPAR,*) D0
        READ(IDPAR,*) WAVELENGTH0
        READ(IDPAR,*) NAT
        CLOSE(IDPAR)
        ALLOCATE (XD(NAT),YD(NAT),ZD(NAT))
        ALLOCATE (PX(NAT),PY(NAT),PZ(NAT))
        OPEN(UNIT=IDPOS,FILE=POSFILE,STATUS='OLD',FORM='FORMATTED')
        DO J=1,NAT
                READ(IDPOS,*) XD(J),YD(J),ZD(J)
        END DO
```

```
        CLOSE(IDPOS)

        MAXXD=XD(1)
        MINXD=XD(1)
        MAXYD=YD(1)
        MINYD=YD(1)
        MAXZD=ZD(1)
        MINZD=ZD(1)

        DO J=1,NAT

        IF (XD(J).GE.MAXXD)THEN
        MAXXD=XD(J)
        END IF
        IF (XD(J).LE.MINXD)THEN
        MINXD=XD(J)
        END IF

  IF (YD(J).GE.MAXYD)THEN
        MAXYD=YD(J)
        END IF
        IF (YD(J).LE.MINYD)THEN
        MINYD=YD(J)
        END IF

  IF (ZD(J).GE.MAXZD)THEN
        MAXZD=ZD(J)
        END IF
        IF (ZD(J).LE.MINZD)THEN
        MINZD=ZD(J)
        END IF

        END DO
        XMIDLE=(MAXXD+MINXD)/2
        YMIDLE=(MAXYD+MINYD)/2
        ZMIDLE=INT((MAXZD+MINZD)/2)
!*****************************************************************
        DIEL0=8.854187E-12
        DIEL=DIEL0*1.0E8
        AIR=1
        CONSTANT=1/(4*3.1415926*DIEL*AIR)
        WAVELENGTH=WAVELENGTH0/1000.0
        D=D0/1000.0
        DELTA=0.25*D
        Z=(ZMIDLE+0.05)*D
        XNPOINTS=1+(2*MAXXD*D/DELTA)
        YNPOINTS=1+(2*MAXYD*D/DELTA)
        ALLOCATE (X(XNPOINTS),Y(YNPOINTS))
        DO J=1,XNPOINTS
                X(J)=(XMIDLE-MAXXD)*D+(REAL(J)-1)*DELTA
        END DO
        DO J=1,YNPOINTS
                Y(J)=(YMIDLE-MAXYD)*D+(REAL(J)-1)*DELTA
        END DO
!*****************************************************************
        OPEN(UNIT=IDPOLXXX,FILE=POLXXX,STATUS='OLD',FORM='FORMATTED')
```

```
        DO J=1,NAT
        READ(IDPOLXXX,*)REALPX,IMAGPX
        PX(J)=CMPLX(REALPX,IMAGPX)
        ENDDO
        CLOSE(IDPOLXXX)

        OPEN(UNIT=IDPOLYYY,FILE=POLYYY,STATUS='OLD',FORM='FORMATTED')
        DO J=1,NAT
        READ(IDPOLYYY,*)REALPY,IMAGPY
        PY(J)=CMPLX(REALPY,IMAGPY)
        ENDDO
        CLOSE(IDPOLYYY)

        OPEN(UNIT=IDPOLZZZ,FILE=POLZZZ,STATUS='OLD',FORM='FORMATTED')
        DO J=1,NAT
        READ(IDPOLZZZ,*)REALPZ,IMAGPZ
        PZ(J)=CMPLX(REALPZ,IMAGPZ)
        ENDDO
        CLOSE(IDPOLZZZ)

!*****************************************************************
        ALLOCATE (EX(XNPOINTS,YNPOINTS),EY(XNPOINTS,YNPOINTS),EZ(XNPOINTS,YNPOINTS))
        ALLOCATE (ESQUARE(XNPOINTS,YNPOINTS),SHOW(XNPOINTS,YNPOINTS))

        DO J=1,NAT
                PX(J)=PX(J)*D**3
                PY(J)=PY(J)*D**3
                PZ(J)=PZ(J)*D**3
        END DO

        DO M=1,XNPOINTS
                DO N=1,YNPOINTS


                        EX(M,N)=0
                        EY(M,N)=0
                        EZ(M,N)=0


                        DO K=1,NAT
                                NDATA=(X(M)-D*XD(K))**2+(Y(N)-D*YD(K))**2+(Z-D*ZD(K))**2

                                NX=(X(M)-D*XD(K))/(NDATA**0.5)
                                NY=(Y(N)-D*YD(K))/(NDATA**0.5)
                                NZ=(Z-D*ZD(K))/(NDATA**0.5)


                                PN=PX(K)*NX+PY(K)*NY+PZ(K)*NZ

                                EXADDFAR=(PX(K)-
NX*PN)*((2*3.1415926/WAVELENGTH)**2)/(NDATA**0.5)
                                EYADDFAR=(PY(K)-
NY*PN)*((2*3.1415926/WAVELENGTH)**2)/(NDATA**0.5)
                                EZADDFAR=(PZ(K)-
NZ*PN)*((2*3.1415926/WAVELENGTH)**2)/(NDATA**0.5)
```

```
                FACTOR=CMPLX(NDATA**(-3.0/2.0),-
2*3.1415926/(NDATA*WAVELENGTH))

                EXADD=CONSTANT*(EXADDFAR+(3*NX*PN-PX(K))*FACTOR)
                EYADD=CONSTANT*(EYADDFAR+(3*NY*PN-PY(K))*FACTOR)
                EZADD=CONSTANT*(EZADDFAR+(3*NZ*PN-PZ(K))*FACTOR)

                EX(M,N)=EX(M,N)+EXADD
                EY(M,N)=EY(M,N)+EYADD
                EZ(M,N)=EZ(M,N)+EZADD


            ENDDO

            ESQUARE(M,N)=(ABS(EX(M,N)))**2+(ABS(EY(M,N)))**2+(ABS(EZ(M,N)))**2



        ENDDO

    ENDDO


    DO M=1,XNPOINTS
        DO N=1,YNPOINTS
            SHOW(M,N)=ESQUARE(M,N)
        END DO
    END DO


    ZROUND=ZMIDLE

    NSURFACE0=0

    DO K=1,NAT
        IF (ABS(ZD(K)-REAL(ZROUND)).LE.(1*10**(-3))) THEN

            NSURFACE=NSURFACE0+1
            NSURFACE0=NSURFACE

        END IF
    END DO


    ALLOCATE (XXD(NSURFACE),YYD(NSURFACE))



    NSURFACE0=0

    DO K=1,NAT
        IF (ABS(ZD(K)-REAL(ZROUND)).LE.(1*10**(-3)))THEN
            NSURFACE=NSURFACE0+1
            NSURFACE0=NSURFACE
            XXD(NSURFACE)=XD(K)
            YYD(NSURFACE)=YD(K)
```

```
        END IF
    END DO


    DO M=1,XNPOINTS
        DO N=1,YNPOINTS
            IF ((X(M).GE.D*(MINXD-
1.0)).AND.(X(M).LE.D*(MAXXD+1.0)).AND.(Y(N).GE.D*(MINYD-
1.0)).AND.(Y(N).LE.D*(MAXYD+1.0)))THEN
                DO K=1,NSURFACE
                    DISTANCE0=(X(M)-D*XXD(K))**2+(Y(N)-D*YYD(K))**2
                    DISTANCE=DISTANCE0**0.5
                    IF (DISTANCE.LE.(0.8*D))THEN
                        SHOW(M,N)=0
                    END IF
                END DO
            END IF
        END DO
    END DO




    OPEN(UNIT=IDX,FILE=XPLANE,STATUS='NEW',ACCESS='SEQUENTIAL',FORM='FORMATTED')
    DO K=1,XNPOINTS
        WRITE(IDX,*)X(K)
        END DO
    CLOSE(IDX)



    OPEN(UNIT=IDZ,FILE=YPLANE,STATUS='NEW',ACCESS='SEQUENTIAL',FORM='FORMATTED')
    DO K=1,YNPOINTS
        WRITE(IDZ,*)Y(K)
    END DO
    CLOSE(IDZ)

    OPEN(UNIT=IDESQUARE,FILE=ESQUAREFILE,STATUS='NEW',ACCESS='SEQUENTIAL',FORM
='FORMATTED')
    DO M=1,XNPOINTS
        DO N=1,YNPOINTS
        WRITE(IDESQUARE,*)ESQUARE(M,N)
        END DO
    END DO

    OPEN(UNIT=IDSHOW,FILE=ESHOW,STATUS='NEW',ACCESS='SEQUENTIAL',FORM='FORMAT
TED')
    DO M=1,XNPOINTS
        DO N=1,YNPOINTS
            WRITE(IDSHOW,*)SHOW(M,N)
        END DO
    END DO

    end program EFIELD
```